Doctoral Dissertation

博士論文

Gravitational hierarchical three-body systems with an invisible inner binary: application to binary black-hole search and their dynamical stability

(不可視連星を含む階層的重力三体系：

連星ブラックホール探査への応用とその力学的安定性)

A Dissertation Submitted for the Degree of Doctor of Philosophy

December 2021

令和３年１２月博士（理学）申請

Department of Physics, Graduate School of Science,
The University of Tokyo

東京大学大学院理学系研究科物理学専攻

Toshinori Hayashi

林 利憲

Abstract

In 2015, LIGO detected the gravitational waves (GWs) from a binary black-hole merger (BBH) for the first time. The discovery gave a huge impact on astronomy, and since then the origin and evolution of BBHs have been widely studied in various contexts. Current continual detection of BBH mergers suggests an abundant population of progenitor BBHs before coalescence with relatively wide separations. The presence of progenitor wide-separation BBHs are also supported by the current formation scenarios, regardless of the details. Nevertheless, they have not yet been discovered because they generally do not emit any detectable signals in both electromagnetic(EM) and gravitational waves. Therefore, such progenitor BBHs needs to be searched for with different methods.

According to current observations, hierarchical triples, which consist of an inner binary and a well-separated tertiary, are known to be ubiquitous in the universe. Although they are mostly stellar triples, the fact implies a fraction of progenitor BBHs may form triple systems with visible tertiaries. In addition, some previous studies suggested such triples can be formed through dynamical capture process in dense clusters. We assume the presence of such triples, and propose novel methods to search for progenitor BBHs through the detection of anomalous motions of tertiary. The motion of the tertiary should be modulated by the gravitational perturbations induced by the invisible inner BBH, and therefore it should include the signature of the inner hidden BBH.

In this thesis, we assume our fiducial triple consisting of inner massive binary of $\mathcal{O}(10)$ $M_\odot$ and a visible tertiary of $\mathcal{O}(1)$ $M_\odot$, with week-scale and month-scale inner and outer orbital periods, respectively. We consider three different probes to search for inner BBHs. The first probe is the short-term radial velocity (RV) variations of a tertiary star, which have a timescale around half the inner orbital period. The second one is the long-term tertiary RV variations, which have the timescale much longer than the orbital periods of two orbits in a triple system. The third one is the arrival time variations of a tertiary pulsar if the tertiary is a pulsar rather than a star. Although tertiary pulsars are likely to be even rarer than tertiary stars, great precision of pulsar timing observations can search for more distant systems beyond kpc scale. This is complementary to the former two methods using RV observations, which is usually applicable up to $\mathcal{O}(100)$ pc scale.

We show that the short-term RV variations can be used as a probe of inner hidden BBH, when a tertiary star is near-by ($\ll$ kpc) and bright enough ($\lesssim 15$ mag) through mock observations. The variations indeed reach $\mathcal{O}(100)$ m/s amplitude with week-scale periods, which will be detected with intensive high precision RV follow-ups. We conclude that the short-term RV variations provide a suitable method to identify inner BBHs especially for coplanar triples. On the other hand, we find that the long-term

RV variations change the Kepler motion amplitude for inclined triples, as a result of orbital plane evolution with respect to the line of sight. The amplitude, therefore, becomes comparable to the huge Kepler motion amplitude itself. For instance, our fiducial triple has $\mathcal{O}(100)$ km/s variations, which should be detected even without high precision RV observations. We show numerically that the variations have long timescale, but still can be detected within decades depending on orbital parameters. For instance, the variations should be detected within a few decades for our fiducial triples. Therefore, we conclude that the long-term RV variations are very promising probe of the inner BBHs in inclined triples.

As for the pulsar arrival time variations, we show that it is possible to identify an inner BBH and its orbital parameters unambiguously. Moreover, we found that very precise pulsar timing with μsec scale uncertainty can identify an inner BBH down to hour-scale orbital period, given a day-scale outer orbital period. Since closer BBHs can be searched with future space-based low-frequency GW detectors, we can effectively cover a large parameter space of inner BBHs combining two methods in the future.

Finally, we consider the dynamical stability of triple systems. This is worth studying in order to examine the stable triples to which we can apply our methods. Even apart from the point, the dynamical stability is on its own important in the three-body problem. It has been widely studied previously, and many stability/instability criteria and the disruption time estimation model based on a Random Walk have been proposed. We performed a series of numerical simulations for different configurations of hierarchical triples. We found that the previous models are applicable only to a limited range of orbital configurations. In particular, we found that retrograde triples tend to remain stable for longer timescales. The result indicates the importance of extending the models, based on the disruption processes depending on orbital configurations in the future.

In summary, we propose methods to detect progenitor BBHs with relatively wide separations, in different ways from GW observations. We show that such BBHs can be detected with RV and pulsar timing observations of visible tertiaries, if the BBHs are inside triples. We expect that (star - BBH) triples will be searched for from candidate (star - unseen companion) binaries in the future. If such triples are successfully detected, the discovery will become remarkable as the first detection of not only progenitor BBHs, but also triples including BBHs.

Contents

Chapter 1

Introduction

Three-body problem is one of the most important and long-standing problems in classical mechanics, and it has been indeed widely studied over the long history of astronomy. In the 17th century, Isaac Newton established the Newtonian dynamics, and his theory of universal gravity (Newton 1687). The theory was first applied to the two-body problem, and successfully explained Kepler's laws for the planets in the Solar System. His interest soon moved on to the motion of the moon under the gravity of the earth and the sun, so called the Lunar theory. However, it was soon recognized that the three-body problem involved significant theoretical difficulties compared with the two-body problem.

Since then, many physicists and mathematicians were attracted by the three-body problem. For example, Gauss, Laplace, Lagrange, and many famous mathematicians worked on the three-body problem in the 18th and 19th centuries, and contributed to establish the perturbation theory in analytical dynamics (e.g. Laplace 1798). They developed a framework to treat the problem perturbatively, developing the gravitational force into a series expansion and taking account the low-order terms. The perturbation theory was later extended and applied to various problems, including the Lunar theory (e.g. Brown 1899; Hill 1877), the perihelion shift of Mercury (e.g. Le Verrier 1859), the secular evolution of planets and satellites, called the ZKL oscillations(e.g. Kozai 1962; Lidov 1962; von Zeipel 1910). Mathematical consideration of the perturbation theory of the three-body problem even led to the pioneering discovery of chaos by Poincaré (e.g. Poincaré 1892), and it started the theory of dynamical system in applied mathematics, which is currently used in many fields including physics, chemistry, biology, and epidemiology.

One of the most successful results from the perturbation theory in celestial mechanics is the discovery of Neptune in 1846 by Adams and Galle (e.g. Galle 1846). In human history, only six planets from Mercury to Saturn were known from the ancient era. In 1781, after the invention of telescope in the late 16th century, Herschel discovered Uranus using his telescope. About half a century later, Adam and Le Verrier recognized the motion of Uranus had un-explained anomalous behavior, and in order to explain it, they predicted an outer un-discovered planet using the perturbation theory (e.g. Adams 1846; Le Verrier 1846). The later observations actually discovered

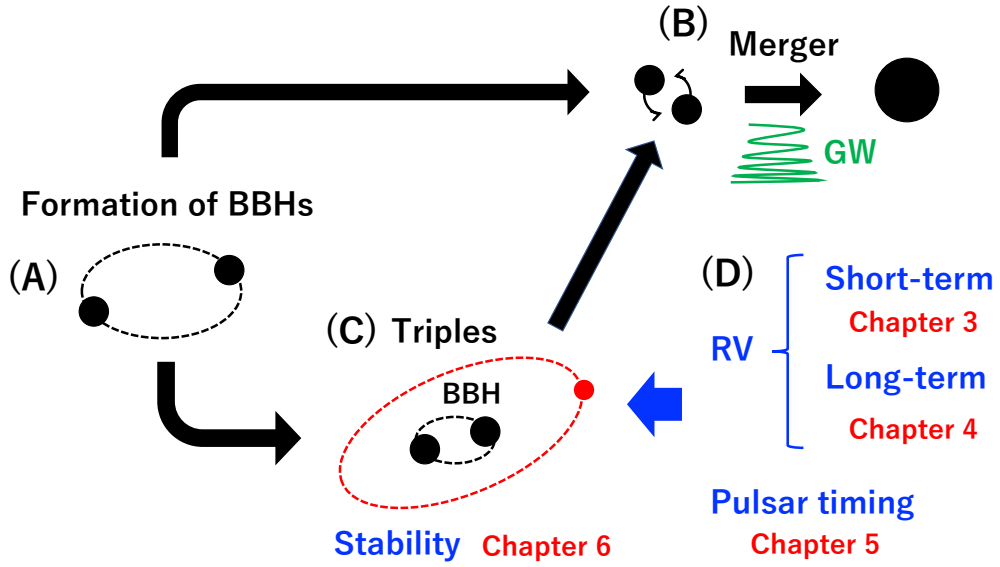

Figure 1.1 A schematic illustration for the flowchart of this thesis.

the corresponding planet, now known as Neptune. This is a remarkably successful example that the anomalous motions identified an unknown object, which is deeply related to our motivation in this thesis.

Figure 1.1 shows the schematic illustration of the background picture of this thesis. In 2015, LIGO detected the gravitational waves (GWs) from a binary black hole (BBH) merger event. A BBH emits strong and high-frequency ($\mathcal{O}(10) - \mathcal{O}(100)$ Hz) GWs at the final stage of BBH evolution before coalescence (see Figure 1.1, (B)), and such a BBH merger was indeed detected with current ground-based GW detectors. This discovery was quite revolutionary in physics as the first detection of the GWs, which have been predicted in the theory of general relativity. It was, however, also important as the first discovery of close massive binary black holes (BBHs) in the universe. Although some pioneering studies (e.g. Belczyński & Bulik 1999; Portegies Zwart & McMillan 2000) have suggested the presence of close BBHs, such BBHs were not seriously believed to exist before the LIGO's first discovery. Since then, the number of observed BBH mergers has increased rapidly, and reached around 90 in GWTC-3 catalog as of 2021, which strongly indicates a significant fraction of black holes form binaries in the universe. Currently, there are several scenarios proposed to form such BBHs, including the isolated binary evolution scenario (e.g. Belczyński & Bulik 1999; Belczynski et al. 2012, 2016, 2002, 2007; Dominik et al. 2012, 2013; Kinugawa et al. 2014, 2016), dynamical capture in dense regions (e.g. O'Leary et al. 2009, 2006; Portegies Zwart & McMillan 2000; Rodriguez et al. 2016; Tagawa et al. 2016), and the formation from primordial black holes (e.g. Bird et al. 2016; Sasaki et al. 2016, 2018) (see Figure 1.1, (A)). We emphasize here that, regardless of the details of the formation scenarios, a long-term gravitational wave emission is required for progenitor, possibly wide-separation, BBHs ((A) in Figure 1.1) to coalesce ((B) in Figure 1.1). In turn, this

implies that there are abundant progenitor BBHs with relatively long orbital periods in the universe. Nevertheless, such progenitor BBHs have not yet been discovered because they generally do not emit any detectable signals in either electromagnetic or gravitational waves. The difficulty indicates that such progenitor wide-separation BBHs needs to be searched for indirectly through their dynamical influence on nearby visible objects. This motivated us to consider a hierarchical triple, which has well-separated inner and outer orbits, consisting of an inner invisible massive BBH and a visible tertiary ((C) in Figure 1.1).

Indeed, it is known that hierarchical triple systems are ubiquitous in the universe from observations. More than 70 % of OBA-type stars and 50 % of FGK-type stars are observationally known to belong to multiple systems (Raghavan et al. 2010; Sana et al. 2012). Even in the present epoch, more and more triples are being discovered with recent observations, and orbital properties are precisely determined (e.g. Hajdu et al. 2021; Tokovinin 2021; Tokovinin & Latham 2020). In addition, Moe & Di Stefano (2017) found that the observed fraction of stars belonging to multiple systems increases with their masses. Such massive stellar triples may provide a fraction of triple systems including an inner BBH although the detailed fraction has been uncertain due to the complicated evolution of stars in triple systems. Interestingly, some previous studies (e.g. Antognini 2015; Fragione et al. 2020; Trani et al. 2021) suggested that dynamical capture processes in clusters can also form such triples.

Indeed, there are a few interesting triples discovered previously, which are analogous to triples we are interested in. For instance, Ransom et al. (2014) discovered a triple system consisting of an (inner white dwarf (WD) - pulsar) binary and a tertiary WD. In addition, recently, Gomez & Grindlay (2021) reported the detailed analysis and modeling of HD96670, and proposed that the system is likely to be a triple including an inner binary consisting of an O type star with $22.7^{+5.2}_{-3.6}$ $M_\odot$ and a possible black hole companion with $6.2^{+0.9}_{-0.7}$ $M_\odot$. Lennon et al. (2021a) analyzed the result of VLT-FLAMES survey of NGC 2004#115, and found that the system may be a triple with inner binary of a 8.6 $M_\odot$ B-type star and a possible black hole companion with mass larger than 25 $M_\odot$. Therefore, it is likely that a fraction of BBHs belong to triple systems ((C) in Figure 1.1).

Furthermore, there are several on-going surveys that search for a (star - unseen companion) binary. There are many proposals to search for (star - black hole) binaries with Gaia astrometry observation (e.g. Breivik et al. 2017; Kawanaka et al. 2017; Mashian & Loeb 2017; Shikauchi et al. 2020; Yamaguchi et al. 2018). For instance, Yamaguchi et al. (2018) estimated the number of detectable such binaries with Gaia is $200 - 1000$ in five year operation. Another important survey is performed with TESS photometry observation for near-by stars. Masuda & Hotokezaka (2019) pointed out that TESS will potentially discover near-by $10 - 100$ (star - black hole) binaries from a relativistic effect in the photometric light curves. These star- unseen companion binaries will not be discriminated from (star - inner BBH) triples initially. Therefore, it is possible that a (visible body - unseen companion) binary will turn out to be an (inner unseen binary - tertiary) triple after follow-up observations. In this sense, we

will potentially have some candidates of triples in the near future. Indeed, Gaia full data release 3 is planned in 2022, and we expect many such binaries in due course.

Based on the situation as described above, we assume a fraction of progenitor BBHs form triple systems with visible tertiaries, and propose to search for them through observation of the anomalous motions of a tertiary induced by the gravitational perturbations of an inner binary. We consider three different methods, and present the results of our study in chapter 3, 4, and 5 (Hayashi & Suto 2020, 2021; Hayashi et al. 2020, hereafter, HS2020, HS2021, and HWS 2020, respectively). Figure 1.1 (D) classifies these methods and the corresponding chapters in this thesis. In chapter 3, we first consider the short-term radial-velocity (RV) variations of a tertiary star, which have the timescale around half an inner orbital period. Then, in chapter 4, we move on to the long-term RV variations, which have the timescale much longer than the orbital periods. Finally, we consider the pulsar arrival time variations of a tertiary pulsar. We show that these three methods, complimenting each other, indeed provide plausible probes to identify inner progenitor BBHs when the follow-up observations are performed for candidate binaries.

Finally, we briefly consider the dynamical stability of such triples in chapter 6. Since our methods can apply only to triple systems with long lifetime, it is mandatory to examine the properties of triples to which we apply our methods ((C) in Figure 1.1). Even apart from this point, the dynamical stability of triple systems is very interesting in the three-body problem. Indeed, there are many previous studies that considered the stability/instability of triple systems, and many criteria were proposed to judge the stability/instability of triples (e.g. Mardling & Aarseth 1999; Mylläri et al. 2018; Wei et al. 2021). Unlike such criteria for judging only the stability/instability, recently, Mushkin & Katz (2020) proposed a Random Walk (RW) model to estimate the disruption time of triples with high outer eccentricities. This is indeed important to consider how long a triple system remains a stable orbit. Nevertheless, it has not yet been certain how orbital configuration, such as mutual inclination and mass ratio, affects these models. We extend the previous models including such orbital configuration dependency. In chapter 6, through a series of numerical simulations, we show that the previous models are applicable only to a limited range of orbital configurations. In particular, we show that retrograde triples tend to remain more stable than the prediction of previous models. The result indicates the importance to consider different disruption processes for such configurations, and extend the models in the future.

The rest of this thesis is organized as follows. Chapter 2 shows the background of our study, and reviews on the relevant previous works. We discuss both observational and theoretical backgrounds in chapter 2. The following three chapters are devoted to our proposed methods to search for inner BBHs inside triples. First, chapter 3 summarizes our method using the short-term RV variations for coplanar triples. We here show that our strategy indeed works well through mock observations. Chapter 4 rather considers the long-term RV variations. We show the long-term RV variations provide an ideal probe of inner unseen binary especially for non-coplanar triples. In

chapter 5, we consider a tertiary pulsar, and propose to use the pulsar arrival time variations to search for inner BBHs. Although such triples are expected to be very limited in number, we confirm that the pulsar timing has an ability to detect inner BBHs, and determines the orbital parameters precisely even without degeneracy. We discuss here a possible synergy of this method with the future space-based GW detectors. In chapter 6, we briefly consider the dynamical stability and disruption timescale of triples. We here compare the simulations with the RW model (Mushkin & Katz 2020) and the dynamical stability criterion (Mardling & Aarseth 1999). Finally, chapter 7 is devoted to the summary and conclusion of this thesis, and we discuss here the possible future prospects. Technical details and/or supplementary materials are discussed in the appendix.

Chapter 2

Background

2.1 Multiple systems including unseen companions

2.1.1 Current observed systems relevant for our study

LIGO's detection of BBH mergers strongly suggests that there should be abundant progenitor BBHs, and some of them possibly form triple systems with visible tertiaries. Although such triples are not yet discovered, there exist a couple of known interesting systems that are relevant for our study in this thesis. In this subsection, we briefly review on the systems.

The first system is a binary system 2M05215658+435922, which consists of a red giant and an unseen companion. This system is one good example to clearly indicate what we consider in this thesis as candidates for follow-up observations applying our methodology.

Next, we introduce a couple of triple systems that are likely to include compact stars. Although the systems themselves are not triples that we consider to search for, the presence of these triples highly encourages our methodology. We first review on a triple system, PSR J0337+1715, which consists of a (pulsar - white dwarf) inner binary and a tertiary white dwarf. Then, we review on a recent report on the discovery of triple possibly including a black hole companion inside the inner binary, NGC 2004#115.

Indeed, recently, systems including black hole companions have very often been reported. For example, LB-1 was reported as a binary including a very massive black hole companion (Liu et al. 2019), and HR6819 was also reported as a triple including a black hole inside its inner binary (Rivinius et al. 2020). The nature of these systems are currently disputed since the reanalysis of observational data revealed that other interpretations such as rapidly rotating Be star companions are likely (e.g. Bodensteiner et al. 2020; Shenar et al. 2020). Nevertheless, these examples also indicate that multiples including compact companions have been drawing increasing attention in astronomy. If later followup observation confirm the presence of black hole companions in LB1 and HR6819, these systems will also be added to relevant systems for our study.

parameter	value	meaning
$P_{\rm out}$	83.205 ± 0.064 days	orbital period
$m_{\rm co}$	$3.3^{+2.8}_{-0.7}$ $M_\odot$	mass of an unseen companion
$m_{\rm giant}$	$3.2^{+1.0}_{-1.0}$ $M_\odot$	mass of a red giant
$e_{\rm out}$	0.00476 ± 0.00255	eccentricity
$\omega_{\rm out}$	197.13 ± 32.07 deg	argument of pericenter
$\sin i$	$0.97^{+0.03}_{-0.12}$	inclination of the orbital plane
$R_{\rm giant}$	30^{+9}_{-6} $R_\odot$	radius of a red giant

Table 2.1 Best-fit parameters for the binary system 2M05215658+4359220 (Thompson et al. 2019)

A binary system 2M05215658+4359220

In chapters 3 and 4, we propose two methods to search for an inner unseen binary with the radial-velocity modulations of a tertiary star with followup observations. In order to apply our methods, it is very important to select candidates of (star - inner binary) triples before actual observations. We expect that such candidates will be first discovered as (star - unseen companion) binaries with large-scale surveys such as Gaia astrometry and TESS photometry observations. Interestingly, a (red giant - unseen companion) binary was reported in Thompson et al. (2019). In the following, we review on the system as a good example of our target binaries.

In 2018, Thompson et al. (2019) reported a discovery of a binary system 2M05215658 +4359220 that consists of a red giant and an unseen massive object. They first searched for systems exhibiting anomalously large radial accelerations from the Apache Point Observatory Galactic Evolution Experiment (APOGEE) radial velocity data, and selected 200 candidates of such binaries. After checking the photometric variations from the All-Sky Automated Survey for Supernovae (ASAS-SN) data, they identified 2M05215658+4359220 as the most likely binary candidate. Subsequently, they performed the radial velocity follow-up observations with the Tillinghast Reflector Echelle Spectrograph (TRES) on the 1.5 m telescope at the Fred Lawrence Whipple Observatory (FLWO). They obtained 11 spectra with the precision of about 0.1 $\rm kms^{-1}$ over several months in 2017 and 2018.

Interestingly, the orbital period of the binary turned out to be very close to the photometric variation period of the star, indicating the tidal synchronization. Therefore, they assumed that the inclination of the rotation axis of the outer red giant $i_{\rm rot}$ is equal to its orbital inclination $i_{\rm orb}$ with respect to the line of sight: $i \equiv i_{\rm rot} = i_{\rm orb}$. This enabled them to estimate the best-fit parameters of the system (Table 2.1) from the RV data and the spectroscopic analysis of the red giant. Thompson et al. (2019) estimated the mass of the unseen companion to be $m_{\rm CO} = 3.3^{+2.8}_{-0.7}$ $M_\odot$.

This binary system is interesting since the estimated mass of unseen companion exceeds a conventionally accepted range of the maximum mass of the neutron star. It could be a single BH, or even a binary neutron star/BH. In the appendix, we put a con-

straint on an assumed possible inner unseen binary using observational uncertainties of the radial velocity of a the star.

A triple system PSR J0337+1715

In chapter 5, we assume a triple consisting of an inner BBH and a tertiary pulsar, and propose a method to search for the inner BBH with the pulsar timing of tertiary. Although such triples have not yet been discovered, one interesting system, which is analogous to our target triple, was reported in Ransom et al. (2014). The discover is very encouraging to our study, and therefore we review on the triple, PSR J0337+1715.

Ransom et al. (2014) reported a discovery of a triple system PSR J0337+1715, that is a triple system consisting of an inner white dwarf-pulsar binary and an outer white dwarf orbiting around the inner binary.

The authors first discovered a millisecond pulsar PSR J0337+1715 with 2.73 msec spin period from large-scale pulsar survey with the Robert C. Byrd Green Bank Telescope (GBT). Although the system was first considered to be a binary with a white dwarf, later analysis of the large timing systematics revealed that the observed time delays were decomposed into two periodic signals, and the system is indeed a triple rather than a binary. Simultaneously, a large timing perturbation indicated that a tertiary companion is massive unlike the previously known two pulsars B1257+12 and B1620-26, that form multiple systems with planet-mass companions.

In order to determine the orbital parameters, they performed intensive multi-frequency radio timing followups using the GBT, the Arecibo telescope, and the Westerbork Synthesis Radio Telescope (WSRT). They successfully obtained about 100 nsec precision timing data, which were extraordinarily precise, with half-an-hour integrations of the Arecibo data. They used the Solar System barycentre at infinite frequency with the Very Long Baseline Array (VLBA) in order to calibrate the pulse times of arrival (TOA).

The TOAs had the variations induced by two different physical effects. One is the "Rømer delay", which is caused by the finite speed of light and the position difference during the motion. The other is the relativistic delays, which are caused by the relativistic redshift (Einstein delay), and the effect of space-time curvature in the photon path (Shapiro delay). The Rømer delay reflects the information on the orbits, and the relativistic delays, especially the Shapiro delay, can be used to determine the inclination of the system. The authors first used the two-Kepler-orbit approximation, but the resulting residuals soon showed the discrepancy caused by the three-body interactions. The fact clearly shows the importance of including the three-body effects to analyze the TOAs of triple systems. In order to find the best parameter sets minimizing the discrepancy, they used the Monte Carlo technique with the numerical integrations including the three-body interactions. The best-fit parameters are summarized in Table 2.2. Due to the great precision of TOAs, the parameters are determined very precisely.

Although the pulsar timing only cannot reveal the physical properties of two companions of the pulsar, they succeed in identifying one object with blue colors with the Sloan Digital Sky Survey (SDSS). They confirmed that the object was consistent with

parameter	value	meaning
P	2.73258863244(9) ms	Pulsar period
$\dot{P}$	$1.7666(9)(12) \times 10^{-20}$	Pulsar period derivative
τ	2.5×10^9 yrs	Characteristic age
$a_{\rm I}$	1.9242(4) ls	Pulsar semi-major axis(inner)
$e_{\rm I}$	$6.9178(2) \times 10^{-4}$	Eccentricity(inner)
$\omega_{\rm I}$	97.6182(19) deg	Longitude of pericentre(inner)
$a_{\rm O}$	118.04(3) ls	Pulsar semi-major axis(outer)
$e_{\rm O}$	$3.53561955(17) \times 10^{-2}$	Eccentricity(outer)
$\omega_{\rm O}$	95.619493(19) deg	Longitude of pericentre(outer)
i	39.243(11) deg	Inclination of invariant plane
$i_{\rm I}$	39.254(10) deg	Inclination of inner orbit
δ_i	$1.20(17) \times 10^{-2}$ deg	Angle between orbital planes
δ_ω	$-1.9987(19)$ deg	Angle between eccentricity vectors
$m_{\rm p}$	1.4378(13) $M_\odot$	Pulsar mass
$m_{\rm cI}$	0.19751(15) $M_\odot$	Inner companion mass
$m_{\rm cO}$	0.4101(3) $M_\odot$	Outer companion mass

Table 2.2 Best-fit system parameters for PSR J0337+1715. Note that values in parentheses are 1σ errors in the final decimal places. Adapted from Ransom et al. (2014).

an inner white dwarf companion. While the outer companion was not detected in the survey, they confirmed that the companion should not be a low-mass main-sequence star due to the lack of near- and mid- infrared excesses. They concluded that the outer companion was likely to be a white dwarf with the effective temperature less than 20000K. Then, they reported the discovery of a triple system consisting of a pulsar-WD inner binary and an outer WD companion.

Quite interestingly, Table 2.2 shows that the inner and outer orbits are near-circular and coplanar; the eccentricities of the inner and outer orbits are $e_{\rm I} \sim 6.9 \times 10^{-4}$ and $e_{\rm O} \sim 3.5 \times 10^{-2}$, and the mutual inclination is $\delta_i = (1.20 \pm 0.17) \times 10^{-2}$ deg. In the paper, the authors proposed a possible formation scenario of such triples as follows although the details of formation processes have not yet been established. First, the system was formed as a multiple stellar system. Then, the most massive star in the system evolved into a neutron star after a supernova explosion. Two companions successfully survived the explosion, probably in eccentric orbits. The outer companion star later evolved into a WD and transferred mass into the inner binary after Gyr-scale evolution. The process likely aligned two orbits through the angular momentum exchange. After additional Gyr-scale evolution, the remaining main-sequence star finally turned into a WD while circularizing the inner binary and transferring mass to a companion neutron star. During this process, the neutron star speeded up its rotation, resulting in the formation of a millisecond pulsar. Finally, the secular evolution of

triple aligned the apsides of two orbits. This is the scenario that the authors proposed in order to form a near-circular and coplanar triple consisting of compact stars. The scenario, although it has not yet been confirmed, has a possibility to produce a triple containing a pulsar.

Triple system NGC2004#115

Recently, there are a couple of observational reports for the discovery of triples including possible black hole companions. For instance, Gomez & Grindlay (2021) proposed that HD96670 is a triple system with an inner binary of ~ 5.3 day orbital period consisting of a 23 $M_\odot$ O type star and a 6 $M_\odot$ possible black hole. Lennon et al. (2021a) also proposed that NGC2004#115 is a triple including a tight inner binary consisting of a B-type star and a possible black hole. Although they are not our target triples including inner BBHs, the discoveries are very encouraging to our study, implying the existence of our target triples. In the following, we briefly review on Lennon et al. (2021a) as an example of such triple systems.

In 2021, Lennon et al. (2021a) presented the recent observational report for NGC2004 #115. NGC2004#115 is a star located around a young cluster NGC2004, on the northern edge of the Large Magellanic Cloud. The star was observed with the VLT-FLAME Survey of Massive Stars (FSMS) in 2003 and 2004, and first classified as a B type star in a single-lined spectroscopic binary system. However, the detailed analysis was performed in Lennon et al. (2021a) with additional recent observations with the Southern African Large Telescope (SALT), and it was revealed that the system is likely to be a triple system consisting of an inner (B-type star - black hole) binary and a less massive B-type tertiary star.

The authors first checked the spectroscopic profiles, and confirmed that Hα profiles showed the double-peaked emission, plus a narrow absorption line from primary B-type star. They performed the radial-velocity analysis of primary B-type star using the narrow metal lines, and found that the primary form a binary system of a few day orbital period, with an unseen secondary. Interestingly, they found that the best-fit RV solution varied depending on the observational data they used. This is indeed a clear evidence of the presence of a tertiary, which affects the RV of inner binary. The best-fit RV solution was revealed to be better when only including FSMS data taken within the final week of observational campaign, instead of including full FSMS and SALT data. Table 2.3 summarizes the best-fit parameters from RV solution using only final-week FSMS data.

Then, they performed an atmospheric analysis for the primary B-type star following Lennon et al. (2021b). The atmospheric analysis was able to estimate the parameters successfully, such as the effective temperature $T_{\rm eff}$, surface gravity $\log g$, radius R, line width parameter $v_{\rm e} \sin i$, and chemical components. From the analysis, they concluded that the primary is likely to be a ~ 9 $M_\odot$ B-type star.

Then, they assumed a synchronous orbit for the inner binary, which was expected from the synchronization timescale analysis of this system. Under this assumption, they were able to constrain the mass of secondary to be in excess of 25 $M_\odot$. Such a

parameter	value	meaning
P	2.918 ± 0.010 days	period
T_p	2453005.45 ± 0.10 HJD	time of pericentre
e	0.02 ± 0.02	eccentricity
ω	171 ± 10 deg	argument of pericentre
γ	326.5 ± 2.1 km/s	systemic velocity
K_1	62.4 ± 0.5 km/s	the RV amplitude
$a_1 \sin i$	3.60 ± 0.03 $R_\odot$	projected semi-major axis from center of mass
$f(m_1, m_2)$	0.073 ± 0.005 $M_\odot$	mass function

Table 2.3 Best-fit RV parameters for inner binary of NGC2004#115. Adapted from Lennon et al. (2021a).

large mass estimate and the lack of secondary component in spectrum implied that the secondary is likely to be a black hole.

The property of tertiary was weakly constrained using the spectrum subtracting the primary component expected by best-fit atmospheric model. The resulting ~ 60 day residual spectrum never show the significant radial-velocity difference, which indicates the orbital period of tertiary is more than 120 days. Although the tertiary property was not well determined in the analysis, they also found that the tertiary is likely to be a $6 - 7$ $M_\odot$ B-type star from the V-band flux ratio assuming an isochrone with narrow-lined B-type star. Therefore, they concluded that NGC2004#115 is likely to be a triple consisting of an inner (B-type star - massive black hole) binary and a distant B-type star tertiary. Again, we would like to emphasize that the presence of triple including a black hole companion encourages the possibility of the presence of our target triples.

2.1.2 Proposals for surveys on star- unseen object binary systems

In order to apply our methods to search for inner invisible BBHs in triples, it is required to select candidate systems for follow-up observations. Currently, there are many proposals to search for a (star- black hole) binary with large-scale surveys such as Gaia and TESS. If such binaries are discovered in the future, we can select follow-up targets applying our methods among such systems. Therefore, the large scale surveys play an important role for our methods in practice. In the following, we briefly review on the current proposals to search for (star - black hole) binary systems with Gaia and TESS.

First, we review on the proposals in Yamaguchi et al. (2018) and Shikauchi et al. (2020), which estimate the number of detectable (star - black hole) binaries with Gaia. Yamaguchi et al. (2018) are based on isolated binary evolution model, and estimate that the detectable number is $200 - 1000$. Shikauchi et al. (2020) are based

on dynamical capture model in the open cluster, and the detectable number is ~ 10.

Next, we review on the proposal in Masuda & Hotokezaka (2019). The authors proposed that TESS photometric observations also have an ability to detect star - black hole binaries. They consider two models to estimate the detectable number of such binaries with TESS, and suggested that 10 - 100 binaries will be detected in the future. The proposal is encouraging especially for our method using the tiny short-term RV variations since TESS surveys on near-by bright stars, to which very precise RV monitoring would be applicable.

Gaia astrometric surveys on (star - unseen companion) binaries

Gaia is a large-scale astrometric observational mission after Hipparcos (Gaia Collaboration et al. 2016). The mission started scientific observations in 2014, and it is still on-going until 2022. Although the main purpose is the precise determination of the locations of about billion stars with the magnitude up to 20 in the Galaxy, it is also expected that Gaia will discover many new objects including exoplanets (e.g. Perryman et al. 2014) and (star - unseen companion) binaries. Indeed, there are many proposals for the surveys on (star - unseen companion) binaries using precise Gaia astrometry (e.g. Breivik et al. 2017; Kawanaka et al. 2017; Mashian & Loeb 2017; Shikauchi et al. 2020; Yalinewich et al. 2018; Yamaguchi et al. 2018). In the following, we briefly review on Yamaguchi et al. (2018) and Shikauchi et al. (2020).

Yamaguchi et al. (2018) considered the standard isolated binary evolution model, and estimated the number of (star - black hole) binaries in the Galaxy. In the isolated binary evolution model, they assumed that a more massive primary star collapsed into a black hole by direct collapse with no natal kick, and formed a (star - black hole) binary. First, they assumed that isolated binary systems have initially logarithmically flat separation distribution, and circular orbits. They used the Kroupa initial mass function for the primary star, and the flat mass ratio distribution for the secondary star. Then, they were able to compute the final distribution of binaries after evolution, taking account of the mass transfer and common-envelope phase. They adopted several different values of parameters in the initial mass function, the mass ratio distribution, common-envelope efficiency, and the black hole mass from the zero-age mass of primary.

In order to determine the spatial distribution, they used the exponentially decreasing number density in the Galactic plane. They only considered the Galactic disk since the systems located in the bulge should not be observed due to the strong interstellar absorption. They assumed the binary occurrence rate was 50% over the whole stellar systems, for simplicity. Under the above setup, they was able to determine the number, and distribution of (star - black hole) binaries in the Galaxy. In order to estimate the number detectable with Gaia, they took account of the interstellar extinction, the standard observational errors of Gaia, and the limitation of detectable orbital period due to the Gaia cadence and mission time.

Finally, the authors concluded that $200 - 1000$ star -black hole binaries would be detected with Gaia, depending on the values of model parameters. The spatial

distribution of such binaries ranges from $1-10$ kpc with the peak around 7 kpc. The mass distribution of black holes is sensitive to the mass ratio of zero-age star and black hole, but the decreasing powerlaw ranged between $4-30\ M_\odot$ in the fiducial case. The authors also found that the companion secondary star are also likely to be massive ($\gtrsim 10 M_\odot$) in order to have detectably wide orbits (au-scale) after common envelope phase.

From the view point of our proposed methods in this thesis, it may be difficult to perform precise RV follow-up observations for the binaries detected with Gaia, since the estimated distances to them are usually large. This is quite discouraging for our method using the short-term RV variations in chapter 3, since it requires high precision RV followups. On the other hand, the high long-term RV variations, which are discussed in chapter 4, may be applicable even for relatively distant systems. Therefore, it is likely that Gaia will provide good targets for us to search for inclined triples via the long-term RV variations.

Next, we move on to Shikauchi et al. (2020), in which the authors estimated the detectable number of (star - black hole) binaries with Gaia contributed from dynamical capture in open clusters. In dynamical capture scenario, a (star - black hole) binary is formed from single stars and black holes as a result of gravitational scatterings and captures in the clusters. This is a clear contrast to isolated binary evolution model, in which a system experiences many drastic binary evolution such as common-envelope and supernova explosion.

First, Shikauchi et al. (2020) adopted the (star - black hole) binary distributions obtained from the N-body simulations of open clusters that were performed in Kumamoto et al. (2020). The N-body simulations were performed using a fourth-order Hermite integration method, also taking account of single and binary stellar evolution models, stellar wind mass loss, and supernova. For simplicity, the simulations neglected the effect of natal kick by asymmetric supernova explosion.

For open clusters, they adopted $2.5\times10^3\ M_\odot$ initial mass, and the Plummer model phase space distribution. Initial half mass density was set as $10^4\ M_\odot \mathrm{pc}^{-3}$. The mass of each body in a cluster was randomly assigned from the Kroupa initial mass function, ranging from 0.08 $M_\odot$ to 150 $M_\odot$. The number of particles and the metalicity were set to be 4266 and solar value, respectively. They neglected the contribution from primordial binaries, and focused on newly formed binaries via dynamical capture. Under the above setup, they performed 1000 different realizations.

In order to estimate the number and spatial distribution, they followed the procedures in Yamaguchi et al. (2018). Only the systems escaping from the clusters were considered since otherwise observations are difficult. They assumed that the local star formation rate density is proportional to the local stellar density, and the contribution fraction from open clusters is estimated to be ~ 0.1 from observations. Following Yamaguchi et al. (2018), the Galactic disk distribution in the Milky Way, the interstellar extinction, and the observational limitation of Gaia were all taken account in the estimation.

Finally, the authors concluded that about 10 cluster-originated (star - black hole)

systems are likely to be detected with Gaia in 5 year operation. The estimated observational distance distribution is peaked around $1-2$ kpc, and the mass distribution of black holes is peaked around 10 $M_\odot$. The mass of companion star is dominated below 10 $M_\odot$, which is a clear contrast to the binaries originated from isolated binary evolution model. It was also found that the detectable orbital period is around yr-scale. Interestingly, the authors found that highly eccentric orbits are dominated in dynamical capture model. In the paper, the authors also claimed that the cluster-originated binaries will be possibly distinguished by chemical composition from isolated-binary originated binaries since they never experience chemical pollutions during the binary evolution.

According to the results in Shikauchi et al. (2020), the contribution from dynamical capture is also possibly detected with Gaia. Interestingly, Shikauchi et al. (2020) also estimated that the detectable systems are likely located at closer distance. This is a quite encouraging result for our method. In addition, some previous studies (e.g. Antognini & Thompson 2016; Fragione et al. 2020; Trani et al. 2021) pointed out that triple systems including inner BBHs can be formed through dynamical capture in clusters. We review on this formation path in a later section.

TESS photometric surveys on (star - unseen companion) binaries

TESS ia a large-scale photometric survey for near-by stars with magnitude up to 16. The mission started the observation in 2018, and is still on-going as the extended mission although the prime mission ended in 2020. The main purpose of TESS mission is discovering many near-by exoplanets by transit observations. Furthermore, Masuda & Hotokezaka (2019) proposed that TESS also has ability to search for (star - black hole) binaries by analyzing light curves in detail, and detecting the modulations by tidal and relativistic effects. Since TESS observes relatively near-by stars compared with Gaia, if TESS detected (star - black hole) binaries, such binaries will be ideal targets for our methods using intensive RV followups. In the following, we briefly review on Masuda & Hotokezaka (2019).

First, the authors considered two different modulation effects in the light curves induced by a black hole companion: self-lensing effect and phase-curve variation effect. The self-lensing effect is a magnification of star flux caused by the gravitational lensing by a companion black hole during eclipse. The effect will be detected in the light curve as a pulse-like peak every orbital period. On the other hand, the phase-curve variation effect is caused by two different physical effects. One is the ellipsoidal variations due to the deformation of star shape by black-hole gravity, and the other is the Doppler beaming due to relativistic effects. The phase-curve variation will be detected in the light curve as a periodic change of star flux. Both self-lensing and phase-curve variation effects will indicate the presence of massive and compact companions.

The authors first estimated the number of stars in TESS Input catalog (Stassun 2017) searchable with the self-lensing and the phase-curve variation effects, separately. They first selected ~ 20 million low mass stars with mass and radius estimated from the catalog, taking account of the observational gap of TESS. The expected photometric

noises from the TESS magnitude, and TESS observation duration and cadence, were also taken account in the selection. The stellar activities such as star spots could cause additional noises or mimicking signals. Thus, in order to evaluate the effects and avoid false detections, the authors analyzed the actual light curves from the Kepler mission, and put the detection thresholds for both self-lensing and phase-curve variation effects, separately. Assuming circular orbits, the authors found that in TESS input catalog $\sim 10^5$ and $\sim 10^6$ stars are " searchable stars " with the self-lensing and phase-curve variation effects, respectively.

Then, they estimated the expected number of star- black hole binaries detected with TESS by considering the occurrence rate of such binaries. Two population models were considered in the estimation. One is the field binary model without binary evolution, and the other is the common envelope model with common-envelope evolution. In the field binary model, they assumed the occurrence rate of (star - black hole) binaries basically follows that of massive star binaries in Sana et al. (2012). The initial mass functions of black hole and star were assumed to be a power-law function and the Kroupa mass function, respectively. The field-binary model neglects drastic binary evolution such as common-envelope phase, and therefore gives one extreme case of estimation. On the other hand, in the common envelope model, the authors took account of common-envelope phase evolution and mass loss. They followed Belczynski et al. (2002), and estimated the orbital shrink and mass loss effects.

Finally, the authors concluded that, regardless of the field-binary and common-envelope models, ~ 10 and ~ 100 (star - black hole) binaries are likely to be detected with TESS by the self-lensing and phase-curve variation effects, respectively. The expected black hole mass ranges between $\sim 5\ M_\odot$ - $\sim 50\ M_\odot$, and the expected orbital period is mainly below a few days. This is quite contrasting to the binaries expected to be detected with Gaia. In addition, the authors also checked the maximum searchable distance, adopting a representative searchable binary, which has 0.8 day orbital period, 7 $M_\odot$ black hole, and a sun-like star companion. The upper limit distance was estimated to be 0.25 kpc and 1.3 kpc for self-lensing and phase-curve variation effects, respectively. This is again very different from Gaia, which would detect the binaries more distant than kpc-scale.

The distance is an important factor affecting the RV precisions. Near-by systems are preferred for our methods since high precision RV followups are required in general. Therefore, the binaries detected with TESS will provide ideal targets foe the application of our methods.

2.1.3 Possible formation paths of triples including binary black holes

The feasibility of our methods in this thesis highly depends on the presence and fraction of triple systems including inner BBHs. Theoretically, it was estimated that there are $10^8 - 10^9$ stellar mass black holes even inside our Galaxy (e.g. Shapiro & Teukolsky 1983). Furthermore, current ground-based gravitational wave detectors continually

detect BBH and BNS mergers, and $\sim$ 90 candidate events are listed in GWTC-3 (The LIGO Scientific Collaboration et al. 2021b) as of 2021. The BBH merger rate is currently estimated to be 17.3 $\mathrm{Gpc^{-3}yr^{-1}}$ - 45 $\mathrm{Gpc^{-3}yr^{-1}}$ (The LIGO Scientific Collaboration et al. 2021a). Therefore, there should be abundant progenitor BBHs before mergers hidden in the universe. From observations, there are abundant stellar triples (e.g. Raghavan et al. 2010; Sana et al. 2012), and the fraction even increases with a mass of star (Moe & Di Stefano 2017). Therefore, it is reasonable that a fraction of progenitor BBHs are embedded in triple systems.

Nevertheless, the formation of such triples have not yet been established so far. It is intuitively expected that a stellar triple evolves into an (inner BBH - star) triple if inner stellar binary first becomes an inner BBH, and a tertiary still remains as a star. However, it is quite uncertain whether a triple can survive after drastic stellar evolution processes such as mass transfer, common-envelope phase, and supernova explosion. Toonen et al. (2020) studied the typical evolution of triples theoretically with simulations, and found the mass transfer is important for most cases. Therefore, many complex processes, for instance, mass transfer in eccentric orbits (e.g. Dosopoulou & Kalogera 2016) and mass-loss induced eccentric ZKL oscillation(e.g. Michaely & Perets 2014; Shappee & Thompson 2013) should take place generally during the evolution. It is also known that common-envelope evolution of inner binary significantly shrinks their orbital separations, and sometimes causes binary merges (e.g. Toonen et al. 2016; Zorotovic et al. 2010). For supernova natal kick, Lu & Naoz (2019) found that the survival rate of triples after supernova natal kick significantly drops as the tertiary mass decreases. Therefore, the formation and fraction of triples we are interested in from stellar triples is still in veil from the current understanding of triple systems.

Interestingly, some previous theoretical studies revealed that triple systems including compact binaries are likely to be formed in clusters via dynamical capture. Although the feasibility of such formation path has also not yet been confirmed, this is a quite encouraging result for our methodology. In the following, we review on those studies as a possible formation path of our target triples.

Dynamical capture formation scenario of triples including compact binaries

In dynamical capture scenario, the formation of compact multiples takes place in clusters through gravitational scatterings. Whereas isolated triple evolution scenario as the formation of compact multiples undergoes various complicated processes during stellar evolutions, dynamical capture scenario is less affected by such processes, and dominated by gravitational scattering and cluster evolution processes. Therefore, this scenario is widely studied (e.g. O'Leary et al. 2009, 2006; Portegies Zwart & McMillan 2000; Rodriguez et al. 2016; Tagawa et al. 2016) as one of complementary formation scenarios of BBHs with isolated binary evolution (e.g. Belczyński & Bulik 1999; Belczynski et al. 2012, 2016, 2002, 2007; Dominik et al. 2012, 2013; Kinugawa et al. 2014, 2016). Recently. it is also proposed that dynamical capture can form triple systems including compact binaries in clusters (e.g. Antognini & Thompson 2016; Fragione et al. 2020; Trani et al. 2021). In the following, we briefly review on these studies as

a possible formation mechanism of triples we are interested in.

First, Antognini & Thompson (2016) considered the gravitational scattering processes, and studied the cross-sections, parameter distributions of resulting systems, and possible implication for dynamical capture in clusters, with systematic numerical experiments. In the paper, they considered three kinds of gravitational scattering processes: binary-binary, triple-single, triple-binary scatterings as elementary processes.

Then, they performed idealized numerical experiments of these processes with N-body simulations to reveal the cross-section and resulting orbital parameter distribution for each scattering. In the numerical experiments, they fixed the initial separation of target and interloping systems as $\delta = 10^{-5}$, where δ is the ratio of relative gravitational binding and tidal forces at apocentre. They also fixed the maximum collision parameter $b_{\rm max}$ following Hut & Bahcall (1983), and simultaneously confirmed the different choice never affect much the result. Then, 10^6 numerical experiments were performed for each scattering process to investigate the outcomes of scattering events.

The results showed that new triples can be formed via binary-binary scatterings, and one component exchange can occur during triple-single and triple binary scatterings although the cross-section $\hat{\sigma}$ normalized by the area of system is not large: $\hat{\sigma} = 10^{-3} - 10^{-1}$ depending on the initial parameters such as semi-major axis ratio, mass ratio, injected velocity, and eccentricity. Their analyses on the distribution of newly formed triples revealed that relatively compact triples with the semi-major axis ratio of a few - 100, the quasi-thermal or flat eccentricity distribution, and flat cosine mutual inclination distribution are preferred after scattering processes. Based on the results of their numerical experiments, they were able to estimate the rate of dynamical formation of new triples $\Gamma_{\rm newtriple}$. For instance, in all open clusters in the Galaxy, $\Gamma_{\rm newtriple}$ was estimated to be $\sim 2 \times 10^{-5}{\rm yr}^{-1}$ and $\sim 5 \times 10^{-4}{\rm yr}^{-1}$ for triple and binary scatterings, respectively. Although they concluded that the estimated value is not enough to explain the type Ia Supernova rate, the results opened up the possibility of triple formation via dynamical capture in clusters.

Fragione et al. (2020) performed a series of simulations for dynamical formation of triples in dense star clusters such as globular clusters (GCs), along with the cluster evolutions. They used a set of 148 independent cluster simulations presented in Kremer et al. (2020), using the code CMC, which covers nearly the complete range of GCs observed in the Galaxy. The CMC code incorporates the evolution of clusters such as two-body relaxation, and specific stars and compact objects, in addition. Single and binary star evolutions were calculated with NS and BH formation processes also considering supernova natal kicks. In their study, they considered binary-single and binary-binary scatterings, which were integrated with N-body simulations with the addition of gravitational radiation reactions.

They assumed the King density profile for clusters, the Kroupa initial mass function for stars. For primordial stellar binaries, they assumed 5% binary fraction, and uniform mass ratio distribution for secondaries. Binaries were sampled using log-uniform semi-major axis distribution, and thermal eccentricity distribution ($f(e) \propto e$). Primordial triples were not included in their simulations, therefore all the triples were formed via

dynamical capture process. The integration was proceeded for 14 Gyrs unless a cluster underwent disruption or collisional runaway process.

The results of simulations indeed showed that triple systems are produced via binary-binary scatterings efficiently ($\sim 98.2\%$ of total triples). The preferred parameters of newly formed triples are briefly summarized as follows. The inner and outer semi-major axes are preferred to be $\sim 10^{-1} - 10^{1}$ au and $\sim 10^{1} - 10^{3}$ au depending on the initial properties of globular clusters. The resulting semi-major axis ratio is peaked around $10^{1} - 10^{2}$. They also found that only $\lesssim 1\%$ of formed triples can escape from clusters by acquiring enough dynamical recoil kicks.

In the paper, they also discussed the demographics of formed triples. They found that a cluster with $\sim 10^{6}$ particles typically forms hundreds of triples including an inner BBH or an inner MS-BH binary. Interestingly, $\sim 70 - 90\%$ of triples including an inner BBH have a BH as tertiary. In total, $\sim 50\%$ of formed triples are indeed BH triples in the simulations. More relevantly for our study, they found that $\sim 10\%$ of the triples consist of an inner BBH and a non-BBH tertiary such as MS, giant, WD, and NS. Additionally, roughly $\sim 38\%$ of the triples include at least one MS in an inner binary. Although other type triples such as inner binary NS triple were also produced in their simulations, surprisingly, the contribution was only $\sim 2\%$. The authors also discussed the contribution of the ZKL oscillations in newly formed triples, and found $\sim 0.1\%$ of triples including inner BBHs would be merged within the Hubble time, almost independently of the nature of tertiary. Therefore, the authors concluded that the majority of BBH mergers in dynamically formed triples owing to the ZKL oscillations were expected to come from BH triples.

Finally, we review on a resent theoretical result for dynamically formed triples in low-mass young clusters by Trani et al. (2021). In the paper, the authors considered low-mass ($300 - 1000\ M_{\odot}$) young clusters, and the dynamically formed triples there in the context of the ZKL oscillation contributions for merger events. The dynamically formed triples were sampled from the simulations presented in Rastello et al. (2020). Rastello et al. (2020) performed in total 100002 N-body simulations with three different metalicities. The young low-mass stellar clusters were sampled from a power-law distribution with the range of $300 - 1000\ M_{\odot}$, reminiscent of the low-mass young stellar clusters in the Galaxy. The initial half mass radius of a cluster was chosen following Marks & Kroupa (2012). Stellar masses were sampled from the Kroupa initial mass function, and the orbital parameters of primordial binaries were determined following Sana et al. (2012). The simulations were performed taking account of the rapid core-collapse supernova. The simulated young clusters were embedded in a circular orbit at 8 kpc distance from the Galaxy center along with the static external tidal field like solar neighborhoods. Then, each young cluster was integrated up to 100 Myrs, and the formed triples with inner BHs, NSs, or WDs, which were also escaped from the clusters, were selected from simulations.

The authors found that $\sim 7 \times 10^{4}$ triples were formed throughout the simulations. The triples including inner compact binaries contribute $\sim 0.2 - 0.9$ % of total triples, depending on the metalicities. The orbital parameters of such triples are summarized

as follows. The inner and outer semi-major axes are peaked around $\sim$ 86 au and $\sim$ 2700 au, respectively. The resulting semi-major axis ratio is peaked around 30. The inner eccentricity distribution is biased toward lower values around $\sim$ 0, on the other hand, the outer eccentricity is distributed widely peaked around $\sim$ 0.6. The cosine mutual inclination distribution is nearly flat. In addition, $\sim$ 60% and $\sim$ 20% of tertiaries belong to MS and NS, respectively. This is indeed a encouraging result for our proposed methods requiring visible tertiaries. Unfortunately, the expected period of such triples is 1.5×10^4 yrs on average, and may be too long to detect the long-term RV variations discussed in chapter 5. Nevertheless, the short-term RV variations could be detected if a tertiary is in the vicinity of the pericentre, assuming high values of outer eccentricity. In the paper, the authors also discussed the contribution of the ZKL oscillations for inner compact binary mergers. They found that the ZKL oscillations play a crucial role for merger events in triples formed in low-mass young clusters, and only 0.2% of the triples can be merged within 13.3 Gyrs without the ZKL oscillations. Interestingly, a fraction of merger events owing to the ZKL oscillations is expected to be detected as eccentric mergers in the LVK, ET, and LISA frequency bands.

From these studies, it is indicated that dynamical capture in the clusters would provide a possible formation path of triples that we consider in the thesis. Although the fraction is not large, an outer visible tertiary is also found to be possible in this scenario. Therefore, although the fraction and feasibility of triples that we consider have not yet been established, we assume the presence of a triple consisting of an inner BBH and a visible tertiary throughout this thesis.

2.2 Analytic approximate formulae for the anomalous tertiary motions by the inner-binary perturbation

In this section, we review on theoretical aspects of our proposed methods to search for inner BBHs in a triple system. We derive analytic approximate formulae for the short-term and long-term RV variations for a tertiary in due course.

2.2.1 Short-term variations

The short-term RV variations of tertiary induced by the perturbation of binary companion is first considered in Schneider & Cabrera (2006) in the context of detection of exoplanets. In the paper, they claim that the short-term RV variations by an unresolved binary companion can mimic the RV induced by a planet, and therefore needs to be checked carefully to confirm that it is really caused by a planet.

Later, Morais & Correia (2008) consider this problem in detail using perturbation theory, and conclude that the short-term RV variations are not likely to mimic a planet, if the observational data is carefully analyzed. They derive an approximate analytic formula for a coplanar and circular triple, and confirm that the variations

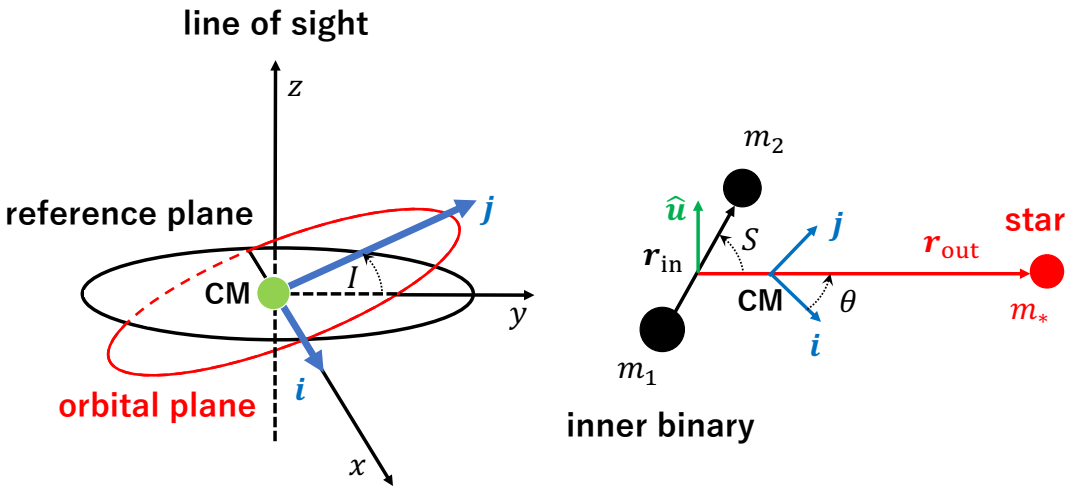

Figure 2.1 A schematic illustration of a triple system consisting of an inner binary and a tertiary star following Morais & Correia (2008). The left panel shows the common orbital plane of the inner binary and the tertiary star. The center of mass of the triple is denoted as CM. An observer is located along the z-direction with I being the inclination of the orbital axis measured by the observer. The right panel shows the definitions of orbital parameters of the system that are described in the main text. Adapted from HWS2020.

consist of two periodic terms, instead of one periodic variation like the RV induced by a planet. They extend their results for eccentric and inclined systems in Morais & Correia (2011) by considering more systematic theory of perturbations.

Although the RV variations are first considered in the context of exoplanetary detections, the variations will also be used to identify an inner unseen binary. This is indeed what we proposed in the present thesis, and in chapter 3, we consider more detailedly how the variations are used to detect an inner unseen binary, and confirm the observational feasibility by mock observations.For definiteness, in the present section, we derive an analytic approximate formula for the short-term RV variations of a tertiary following Morais & Correia (2008). For simplicity, we only consider a coplanar and circular triple here.

The right panel of Figure 2.1 shows a schematic illustration of the coplanar and circular triple we considered in the following derivation. We consider that $\rho \equiv |\boldsymbol{r}_{\rm in}|/|\boldsymbol{r}_{\rm out}| \ll 1$, and treat the perturbation approximately. The Hamiltonian of the system to the second order of ρ is written as

$$\mathcal{H} = \frac{1}{2}\frac{\boldsymbol{p}_{\rm in}^2}{\mu} + \frac{1}{2}\frac{\boldsymbol{p}_{\rm out}^2}{\mu_*} - G\frac{m_1 m_2}{r_{\rm in}} - G\frac{m_{12} m_*}{r_{\rm out}} - G\frac{m_1 m_2 m_*}{r_{\rm out} m_{12}}\rho^2 \frac{1}{2}(3\cos^2 S - 1), \quad (2.1)$$

where $S \equiv \angle(\boldsymbol{r}_{\rm in}\boldsymbol{r}_{\rm out})$, $m_{12} \equiv m_1 + m_2$, $\boldsymbol{p}_{\rm in}$ and $\boldsymbol{p}_{\rm out}$ are the momenta corresponding to $\boldsymbol{r}_{\rm in}$ and $\boldsymbol{r}_{\rm out}$ in terms of Jacobi coordinates, respectively (see the right panel of Figure

2.1). The reduced masses μ and μ_* are defined as

$$\mu \equiv \frac{m_1 m_2}{m_{12}} \quad \text{and} \quad \mu_* \equiv \frac{m_{12} m_*}{m_{12} + m_*}. \tag{2.2}$$

Using the Hamiltonian $\mathcal{H}$, the equations of motion are obtained from the canonical equations:

$$\dot{\boldsymbol{p}}_{\rm in} = -\frac{\partial \mathcal{H}}{\partial \boldsymbol{r}_{\rm in}} \quad \text{and} \quad \dot{\boldsymbol{p}}_{\rm out} = -\frac{\partial \mathcal{H}}{\partial \boldsymbol{r}_{\rm out}}. \tag{2.3}$$

Therefore, the explicit forms of equations of motion for the inner binary and outer star are

$$\ddot{\boldsymbol{r}}_{\rm in} = -G\frac{m_{12}}{r_{\rm in}^3}\boldsymbol{r}_{\rm in} + G\frac{m_*}{r_{\rm out}^3}(3\rho\cos S\boldsymbol{r}_{\rm out} - \boldsymbol{r}_{\rm in}) \tag{2.4}$$

and

$$\ddot{\boldsymbol{r}}_{\rm out} = -G\frac{m_{12}+m_*}{r_{\rm out}^3}\left[\left(1 + \frac{\mu}{m_{12}}\frac{\rho^2}{2}(-3+15\cos^2 S)\right)\boldsymbol{r}_{\rm out} - \frac{\mu}{m_{12}}3\rho\cos S\boldsymbol{r}_{\rm in}\right], \tag{2.5}$$

respectively.

The 0-th order solutions of equations (2.4) and (2.5) for a circular system are as follows:

$$\boldsymbol{r}_{\rm in}^{(0)} = a_{\rm in}\cos S\hat{\boldsymbol{r}}_{\rm out} + a_{\rm in}\sin S\hat{\boldsymbol{u}} \quad \text{and} \quad \boldsymbol{r}_{\rm out}^{(0)} = a_{\rm out}\hat{\boldsymbol{r}}_{\rm out}, \tag{2.6}$$

where $S = S_0 + (\nu_{\rm in} - \nu_{\rm out})t$, and $a_{\rm in}$ and $a_{\rm out}$ are the semi-major axes of the inner and outer orbits, respectively, with S_0 being a constant phase determined by the initial positions. The mean motions $\nu_{\rm in}$ and $\nu_{\rm out}$ are defined as

$$\nu_{\rm in} \equiv \sqrt{\frac{Gm_{12}}{a_{\rm in}^3}} \quad \text{and} \quad \nu_{\rm out} \equiv \sqrt{\frac{G(m_{12}+m_*)}{a_{\rm out}^3}}. \tag{2.7}$$

In terms of the Cartesian coordinate on the orbital plane, unit vectors $\hat{\boldsymbol{r}}_{\rm out}$ and $\hat{\boldsymbol{u}}$ are

$$\hat{\boldsymbol{r}}_{\rm out} = \cos\theta\boldsymbol{i} + \sin\theta\boldsymbol{j} \quad \text{and} \quad \hat{\boldsymbol{u}} = -\sin\theta\boldsymbol{i} + \cos\theta\boldsymbol{j}, \tag{2.8}$$

where $\theta \equiv \theta_0 + \nu_{\rm out}t$, and $\boldsymbol{i}$ and $\boldsymbol{j}$ are constant base vectors (see Figure 2.1), with θ_0 being a constant phase determined by the initial positions. Substituting equations (2.6) - (2.8) into the equation (2.5), we obtain

$$\begin{aligned}\ddot{X} &= -\frac{Gm_{12}}{a_{\rm out}^2}\left[\left(1+\frac{3}{4}\alpha^2\frac{\mu}{m_{12}}\right)\cos\theta + \frac{9}{4}\alpha^2\frac{\mu}{m_{12}}\cos 2S\cos\theta\right. \\ &+ \left.\frac{3}{2}\alpha^2\frac{\mu}{m_{12}}\sin 2S\sin\theta\right]\end{aligned} \tag{2.9}$$

and

$$\begin{aligned}\ddot{Y} &= -\frac{Gm_{12}}{a_{\rm out}^2}\left[\left(1+\frac{3}{4}\alpha^2\frac{\mu}{m_{12}}\right)\sin\theta+\frac{9}{4}\alpha^2\frac{\mu}{m_{12}}\cos 2S\sin\theta\right.\\ &- \left.\frac{3}{2}\alpha^2\frac{\mu}{m_{12}}\sin 2S\cos\theta\right], \end{aligned} \tag{2.10}$$

where X and Y are defined as $\boldsymbol{r}_{\rm out} = X\boldsymbol{i} + Y\boldsymbol{j}$.

The solutions of these equations are written as

$$\begin{pmatrix} X \\ Y \end{pmatrix} = \begin{pmatrix} a_*\cos\theta \\ a_*\sin\theta \end{pmatrix} + \begin{pmatrix} \sin\theta & \cos\theta \\ -\cos\theta & \sin\theta \end{pmatrix}\begin{pmatrix} \delta_X\sin 2S \\ \delta_Y\cos 2S \end{pmatrix}, \tag{2.11}$$

where

$$a_* \equiv \frac{m_{12}}{m_{12}+m_*}\left(1+\frac{3}{4}\alpha^2\frac{\mu}{m_{12}}\right)a_{\rm out}, \tag{2.12}$$

$$\delta_X \approx \frac{3}{8}\frac{\mu}{m_{12}}\alpha^4 a_{\rm out} \quad \text{and} \quad \delta_Y \approx \frac{9}{16}\frac{\mu}{m_{12}}\alpha^4 a_{\rm out}. \tag{2.13}$$

The above expressions for δ_X and δ_Y are derived on the assumption of $\nu_{\rm out}/\nu_{\rm in} \ll 1$.

The radial velocity $V_{\rm RV}$ is defined as

$$V_{\rm RV} \equiv \dot{z} = \dot{Y}\sin I. \tag{2.14}$$

Therefore, we can write down the following RV approximation formula:

$$\begin{aligned} V_{\rm RV} &\approx K_0\left(1+\frac{3}{4}\alpha^2\frac{\mu}{m_{12}}\right)\sin I\cos[\nu_{\rm out}t+\theta_0] \\ &- \frac{15}{16}K_{\rm BBH}\sin I\cos[(2\nu_{\rm in}-3\nu_{\rm out})t+(2S_0-\theta_0)] \\ &+ \frac{3}{16}K_{\rm BBH}\sin I\cos[(2\nu_{\rm in}-\nu_{\rm out})t+(2S_0+\theta_0)], \end{aligned} \tag{2.15}$$

where

$$K_0 \equiv \frac{m_{12}}{m_{12}+m_*}a_{\rm out}\nu_{\rm out} \quad \text{and} \quad K_{\rm BBH} \equiv \frac{m_1m_2}{(m_1+m_2)^2}\sqrt{\frac{m_{12}+m_*}{m_{12}}}\alpha^{3.5}K_0. \tag{2.16}$$

The first term of equation (2.15) corresponds to the modified Keplerian motion, which dominates over the whole RV of tertiary. On the other hand, the RV of tertiary also have two periodic terms represented by the second and third terms of equation (2.15). The variations are very tiny compared with the first term, however in chapter 3 we confirm that they can be used to identify an inner unseen binary after subtracting the base-line Keplerian motion appropriately. Chapter 5 discusses the pulsar arrival time variations as a possible probe of inner unseen binary. Although equation (2.15) is written in the form of the RV, it can be directly translated into the pulsar arrival time delays by integrating the equation over time.

2.2.2 Long-term variations

In the present section, we consider the long-term orbital evolutions which cause the long-term RV variations. Note that the long-term evolution timescale is defined as the timescale much longer than the outer orbital period $P_{\rm out}$ here. When we derive the approximate formula of the short-term RV variations, we neglect the back reaction on an inner binary from a tertiary, and fix the phases such as θ_0 and S_0. Here, we consider a generally inclined and eccentric triple, and show that the orbital elements such as inclinations, longitudes of ascending nodes, and the argument of pericentre all evolve with time in the long-term scale. Note that the argument of pericentre is relevant for θ_0 and S_0 for coplanar triples, and therefore fixed in the previous section. Chapter 4 discusses how the orbital evolution affects the total RV of tertiary, and can be used to identify an inner unseen binary.

The long-term behaviors of triple are widely studied in various contexts using the secular perturbation theory. In the usual perturbation theory, we usually expand the perturbative terms of gravitational force into an infinite series in terms of orbital elements. Then, the evolution of orbital elements is obtained approximately neglecting higher order terms, by solving the Lagrange planetary equations. Indeed, the previous section follows this strategy, and for instance, our non-published result in Hayashi et al. (2019) confirm that the short-term variations of orbital elements are understood using the usual perturbation theory.

However, a different treat is required to understand the long-term behaviors perturbatively. For the purpose, the secular perturbation theory is introduced to extract only the long-term behaviors after subtracting the short-term evolution. In the secular perturbation theory, we use the orbit-averaged Hamiltonian, in which all the dependence of perturbative terms on the true anomaly is averaged out over one orbit. All the short-term behaviors are therefore averaged out, and only the long-term behaviors are evaluated in the approximation.

The secular perturbation is widely used to consider the precession of pericentre (e.g. Le Verrier 1859), the ZKL oscillations (e.g. Kozai 1962; Lidov 1962; von Zeipel 1910), and the evolution of BBHs in triples (e.g. Liu & Lai 2017). In the following discussion, we derive the long-term evolution of orbital elements approximately using the secular perturbation theory, which affects the RV of tertiary. We follow the discussion in Naoz et al. (2013) and Morais & Correia (2012).

We consider a hierarchical triple system consisting of an inner binary and a tertiary. Figure 4.1 shows a schematic configuration of a triple system consisting of an inner BBH and an outer orbiting star. Note that we use the subscript j(= in and out) to distinguish between those variables of the inner and outer orbits, respectively. Unlike the previous section, we assume a triple has non-zero mutual inclination and eccentricity in general. With respect to the reference coordinate system, the inner and outer orbits are specified by the instantaneous longitudes of the ascending nodes Ω_j, semi-major axes a_j, eccentricities e_j, arguments of pericenter ω_j, orbital inclinations I_j, and their mutual inclination $i_{\rm mut}$. Note that our reference plane in Figure 4.1 is arbitrary while it is often chosen as the invariant plane of the triple system.

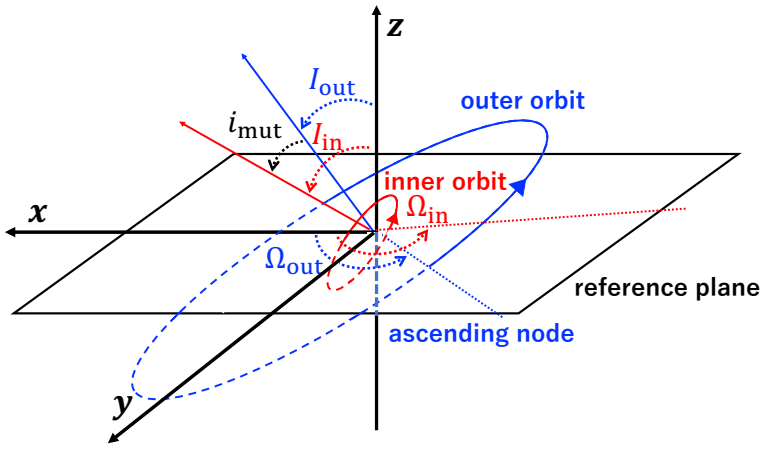

Figure 2.2 Schematic illustration of a triple system that we consider in the present chapter. The orbital angles are defined with respect to the reference Cartesian frame whose origin is set to be the barycenter of the inner orbit. Adapted from HS2020.

The orbit-averaged quadrupole Hamiltonian $\bar{F}$ is given by (e.g., Morais & Correia 2012):

$$\begin{aligned}\bar{F} &= C_{\rm quad}[2-12e_{\rm in}^2-6(1-e_{\rm in}^2)(\sin I_{\rm in}\sin I_{\rm out}\cos(\Delta\Omega)+\cos I_{\rm in}\cos I_{\rm out})^2 \\ &+ 30e_{\rm in}^2(-\sin I_{\rm out}\cos I_{\rm in}\sin\omega_{\rm in}\cos(\Delta\Omega)-\sin I_{\rm out}\cos\omega_{\rm in}\sin(\Delta\Omega) \\ &+ \sin I_{\rm in}\sin\omega_{\rm in}\cos I_{\rm out})^2], \end{aligned} \tag{2.17}$$

where

$$C_{\rm quad} \equiv \frac{\mathcal{G}}{16}\frac{m_1m_2}{m_1+m_2}\frac{m_*}{(1-e_{\rm out}^2)^{3/2}}\left(\frac{a_{\rm in}^2}{a_{\rm out}^3}\right) \tag{2.18}$$

and

$$\Delta\Omega \equiv \Omega_{\rm in}-\Omega_{\rm out}. \tag{2.19}$$

In equation (C.4) and throughout this section, we denote Newton's gravitational constant by $\mathcal{G}$, since G indicates a canonical variable corresponding to an orbital angular momentum.

With the orbit-averaged Hamiltonian $\bar{F}$, secular evolution of orbital angles is explicitly written as (e.g. Danby 1988; Murray & Dermott 2000; Valtonen & Karttunen

2006)

$$\dot{\omega}_j = -\frac{\sqrt{1-e_j^2}}{\mu_j\nu_j a_j^2 e_j}\frac{\partial \bar{F}}{\partial e_j} + \frac{\cos I_j}{\mu_j\nu_j a_j^2\sqrt{1-e_j^2}\sin I_j}\frac{\partial \bar{F}}{\partial I_j}, \tag{2.20}$$

$$\dot{\Omega}_j = -\frac{1}{\mu_j\nu_j a_j^2\sqrt{1-e_j^2}\sin I_j}\frac{\partial \bar{F}}{\partial I_j}, \tag{2.21}$$

$$\dot{I}_j = \frac{1}{\mu_j\nu_j a_j^2\sqrt{1-e_j^2}\sin I_j}\frac{\partial \bar{F}}{\partial \Omega_j} - \frac{\cos I_j}{\mu_j\nu_j a_j^2\sqrt{1-e_j^2}\sin I_j}\frac{\partial \bar{F}}{\partial \omega_j}, \tag{2.22}$$

where $j(=\text{in and out})$. We define the corresponding reduced mass as

$$\mu_{\rm in} \equiv \frac{m_1 m_2}{m_1+m_2}, \tag{2.23}$$

$$\mu_{\rm out} \equiv \frac{m_*(m_1+m_2)}{m_1+m_2+m_*}. \tag{2.24}$$

We note that the Lagrange planetary equations are often written in terms of the disturbing function $R \equiv -\bar{F}$ in celestial mechanics (e.g. Murray & Dermott 2000), but we here use the standard definition of the Hamiltonian.

Neglecting $\mathcal{O}(e_{\rm in}^2)$ terms in equation (2.17), equations (2.20), (2.21), and (2.22) for $j = \text{in}, \text{out}$ are explicitly written as follows:

$$\begin{aligned}\dot{\omega}_{\rm in} = \frac{12C_{\rm quad}(1-e_{\rm in}^2)}{G_{\rm in}}\Big[&2-\cos^2 i_{\rm mut} - \frac{\cos I_{\rm in}}{\sin I_{\rm in}}\cos i_{\rm mut}(\cos I_{\rm in}\sin I_{\rm out}\cos\Delta\Omega \\ &-\sin I_{\rm in}\cos I_{\rm out}) - 5(-\sin I_{\rm out}\cos I_{\rm in}\sin\omega_{\rm in}\cos(\Delta\Omega) \\ &-\sin I_{\rm out}\cos\omega_{\rm in}\sin(\Delta\Omega)+\sin I_{\rm in}\sin\omega_{\rm in}\cos I_{\rm out})^2\Big],\end{aligned} \tag{2.25}$$

$$\begin{aligned}\dot{\omega}_{\rm out} = \frac{6C_{\rm quad}}{G_{\rm out}}\Big[&(3\cos^2 i_{\rm mut}-1) - 2\frac{\cos I_{\rm out}}{\sin I_{\rm out}}\cos i_{\rm mut}(\sin I_{\rm in}\cos I_{\rm out}\cos\Delta\Omega \\ &-\cos I_{\rm in}\sin I_{\rm out})\Big],\end{aligned} \tag{2.26}$$

$$\dot{\Omega}_{\rm in} = \frac{12C_{\rm quad}}{G_{\rm in}\sin I_{\rm in}}\cos i_{\rm mut}(\cos I_{\rm in}\sin I_{\rm out}\cos\Delta\Omega - \sin I_{\rm in}\cos I_{\rm out}), \tag{2.27}$$

$$\dot{\Omega}_{\rm out} = \frac{12C_{\rm quad}}{G_{\rm out}\sin I_{\rm out}}\cos i_{\rm mut}(\sin I_{\rm in}\cos I_{\rm out}\cos\Delta\Omega - \cos I_{\rm in}\sin I_{\rm out}), \tag{2.28}$$

$$\dot{I}_{\rm in} = \frac{12C_{\rm quad}}{G_{\rm in}}\cos i_{\rm mut}\sin I_{\rm out}\sin\Delta\Omega, \tag{2.29}$$

$$\dot{I}_{\rm out} = -\frac{12C_{\rm quad}}{G_{\rm out}}\cos i_{\rm mut}\sin I_{\rm in}\sin\Delta\Omega, \tag{2.30}$$

where $G_{\rm in}$ and $G_{\rm out}$ are the angular momenta of inner and outer orbits defined as

$$G_{\rm in} \equiv \mu_{\rm in}\nu_{\rm in}a_{\rm in}^2\sqrt{1-e_{\rm in}^2}, \tag{2.31}$$

$$G_{\rm out} \equiv \mu_{\rm out}\nu_{\rm out}a_{\rm out}^2\sqrt{1-e_{\rm out}^2}. \tag{2.32}$$

Note that we use an arbitrary inertial frame to write down the equations, rather than the invariant plane. Using equations (2.25) to (2.28), we can understand the long-term behaviors. First, we see the precession of argument of pericentre for coplanar triples, and next move on to the evolution of inclination for inclined triples.

Precession of argument of pericentre for coplanar triples

Chapter 4 discusses the precession of $\omega_{\rm out}$ is used as a probe of inner unseen binary for coplanar triples. The precession is approximately derived from equation (2.26) as follows. For coplanar triples, we can choose $\Delta\Omega = 0$ and $I_{\rm in} = I_{\rm out}$ for a prograde case, and $\Delta\Omega = 0$ and $I_{\rm in} = \pi + I_{\rm out}$ for a retrograde triple. Substituting these values into equation (2.26), for both prograde and retrograde triples, the equation reduces to

$$\frac{\dot{\omega}_{\rm out}}{2\pi} = \frac{3}{4}\frac{1}{P_{\rm out}}\left(\frac{a_{\rm in}}{a_{\rm out}}\right)^2\left(\sqrt{\frac{m_2}{m_1}}+\sqrt{\frac{m_1}{m_2}}\right)^{-2}\frac{1}{(1-e_{\rm out}^2)^2}, \tag{2.33}$$

for $e_{\rm in}^2 \ll 1$. From equation (2.33), we see that the pericentre shift is expected to be detected in the timescale within $\sim P_{\rm out}(a_{\rm in}/a_{\rm out})^{-2}$. We discuss it further using numerical simulations in chapter 4.

Precession of inclination for inclined triples

In the following, we discuss the long-term behaviors of inclined triples. Consider first the case of moderate mutual inclination $i_{\rm mut}$ and small inner eccentricity $e_{\rm in}$, in which the ZKL oscillation is not so effective and $e_{\rm in}$ remains negligibly small. In this case, the secular evolution is basically described by the precession of the inner and outer angular momenta around the total angular momentum axis with $G_{\rm in}$, $G_{\rm out}$, and $G_{\rm tot}$ being constant, where

$$G_{\rm tot} = \sqrt{G_{\rm in}^2 + G_{\rm out}^2 + 2G_{\rm in}G_{\rm out}\cos i_{\rm mut}}. \tag{2.34}$$

Indeed such motion well explains those of I1010 and I0218 in chapter 4, where the normal directions of orbits move on the circles centered at the total angular momentum direction. This behavior is reflected in the long-term RV variations as we see in chapter 4.

The precession timescale can be computed by considering the motion with respect to the invariant reference frame ($\Delta\Omega = \pi$, $i_{\rm mut} = I_{\rm in} + I_{\rm out}$). Since $G_{\rm in}/\sin I_{\rm out} = G_{\rm out}/\sin I_{\rm in} = G_{\rm tot}/\sin I_{\rm mut}$ holds in this case, equations (2.27) and (2.28) reduce to

$$\dot{\Omega}_j = -\frac{12C_{\rm quad}G_{\rm tot}}{G_{\rm in}G_{\rm out}}\cos i_{\rm mut}. \tag{2.35}$$

The precession rate above is constant if we neglect the higher-order variation of mutual inclination, and expressed analytically as

$$P_\Omega = \frac{2\pi}{\dot{\Omega}} = \frac{\pi G_{\rm in}G_{\rm out}}{6C_{\rm quad}G_{\rm tot}\cos i_{\rm mut}}. \tag{2.36}$$

If we neglect $\mathcal{O}(e_{\rm in}^2)$ and $\mathcal{O}(e_{\rm out}^2)$ terms, equation (2.36) is further approximated as

$$\frac{P_\Omega}{P_{\rm out}} \approx \frac{80.7}{\cos i_{\rm mut}} \left(\frac{m_1+m_2+m_*}{23\ M_\odot}\right) \left(\frac{m_*}{3\ M_\odot}\right)^{-1} \left(\frac{P_{\rm out}}{78.9\ {\rm days}}\right) \left(\frac{P_{\rm in}}{10.0\ {\rm days}}\right)^{-1} \quad (2.37)$$

for $G_{\rm out} \gg G_{\rm in}$, and

$$\begin{aligned} \frac{P_\Omega}{P_{\rm out}} &\approx \frac{92.0}{\cos i_{\rm mut}} \frac{(m_1+m_2)^2}{4m_1m_2} \left(\frac{m_1+m_2+m_*}{23\ M_\odot}\right)^{\frac{2}{3}} \left(\frac{m_1+m_2}{20\ M_\odot}\right)^{-\frac{2}{3}} \\ &\quad \times \left(\frac{P_{\rm out}}{78.9\ {\rm days}}\right)^{\frac{4}{3}} \left(\frac{P_{\rm in}}{10.0\ {\rm days}}\right)^{-\frac{4}{3}} \end{aligned} \quad (2.38)$$

for $G_{\rm out} \ll G_{\rm in}$. For comparison, we write down the conventional ZKL timescale for an inner test particle (e.g. Merritt 2013):

$$\begin{aligned} \frac{T_{\rm ZKL}}{P_{\rm out}} &= \frac{m_1}{m_*} \left(\frac{P_{\rm out}}{P_{\rm in}}\right) (1-e_{\rm out}^2)^{3/2} \\ &\approx 26 \left(\frac{m_1}{10\ M_\odot}\right) \left(\frac{m_*}{3\ M_\odot}\right)^{-1} \left(\frac{P_{\rm out}}{78.9\ {\rm days}}\right) \left(\frac{P_{\rm in}}{10\ {\rm days}}\right)^{-1} (e_{\rm out}^2 \ll 1) \end{aligned} \quad (2.39)$$

The timescale roughly agrees with equation (2.37) within order estimation. Therefore, we conclude that the timescale of long-term RV variations can be roughly estimated as the ZKL timescale, which is indeed much larger than the timescale of orbital periods.

While the orbital inclinations $I_{\rm in}$ and $I_{\rm out}$ are constant in the invariant reference frame, i.e., defined with respect to the total angular momentum axis, they also exhibit periodic variations due to the Ω precessions for an an arbitrary line of sight. Thus the period of inclination variations is also given by equation (2.36), which basically explains the behavior of I1010 and I0218 in chapter 4 (see Figures 4.3 and 4.5), in which two orbital planes precess around the total angular momentum.

Consider next a larger mutual inclination ($i_{\rm mut} \approx 90°$, for instance, O1010 and O0218 in chapter 4). In this case, the ZKL oscillation is efficient and increases the inner eccentricity significantly and periodically. Since the precession period, equation (2.36), is inversely proportional to $\cos i_{\rm mut}$, the timescale of the inclination change is very sensitive to the value of $i_{\rm mut}$. The system spends most of their time around $i_{\rm mut} \approx \pi/2$. Then the ZKL oscillation gradually enhances the inner eccentricity, and drastically changes the inclinations. During such transient time, $i_{\rm mut}$ becomes very small, but rapidly goes back to $\approx \pi/2$ again. Therefore, we expect a sudden change of orbital plane for the case with $i_{\rm mut} \approx 90°$. Indeed, we see this behavior for O1010 and O0218 in chapter 4 (see Figures 4.4 and 4.6).

For high mutual inclination, a more quantitative estimate of the corresponding period is difficult and generally requires numerical integration of a set of the Lagrange planetary equations including the eccentricity terms, although several analytical and numerical results have been presented in previous literature (e.g. Antognini 2015; Kinoshita & Nakai 1999; Merritt 2013; Naoz et al. 2013; Vinson & Chiang 2018; Will 2017).

2.3 Dynamical stability of triples

In chapter 6 of this thesis, we consider the dynamical stability of triple systems, and how orbital configurations affect the instability timescale. In this section, we briefly introduce two models relevant for the dynamical stability of triple systems. First, we briefly review on the dynamical stability criterion proposed in Mardling & Aarseth (1999) (hereafter, MA99), as a representative criterion to evaluate whether a given system is stable or not. Second, we review on the Random Walk disruption time estimate model proposed in Mushkin & Katz (2020) (hereafter, MK20), as an important direction of the stability problem; how we can estimate the instability timescale of triples instead of just predicting the instability.

2.3.1 Dynamical stability/instability criterion

In a series of papers (Mardling & Aarseth 1999; Mardling 1995a,b), they derived a criterion to predict the boundary between regular and chaotic behaviors in a binary system with stellar tidal interactions. The chaotic behavior is defined in the sense that the direction and amount of energy flows between the tide and orbits become unpredictable, and it is extremely sensitive to initial small differences. Although the chaotic evolution does not rigorously means the disruption, there is a high probability for chaotic evolution to end up in the binary disruption.

MA99 pointed out that the way energy and angular momentum are exchanged between the inner and outer orbits of a stable hierarchy is very similar to that in a binary normal tidal evolution. Using the analogy, MA99 proposed the following dynamical instability criterion

$$\alpha > \frac{1-e_{\rm out}}{2.8\left(1-0.3\frac{i_{\rm mut}}{\pi}\right)}\left[\frac{\left(1+\frac{m_3}{m_{12}}\right)(1+e_{\rm out})}{\sqrt{1-e_{\rm out}}}\right]^{-2/5}, \tag{2.40}$$

where $\alpha \equiv a_{\rm in}/a_{\rm out}$ is the inner semi-major axis ratio against the outer one, $e_{\rm out}$ is the eccentricity of outer orbit, $i_{\rm mut}$ is the mutual inclination, m_{12} is the total mass of inner binary, and m_3 is the mass of tertiary. Note that the dependence $(1-0.3i_{\rm mut}/\pi)^{-1}$ is later heuristically introduced in Aarseth & Mardling (2001) from the result of stability enhancement with $i_{\rm mut}$ in Harrington (1972). This criterion is analytically determined except for the 2.8 factor, which is empirically determined from simulations. They evaluate the stability whether two orbits, differing by 1 part in 10^5 in the eccentricity, remain 'close' after 100 orbits.

This criterion is widely used in various contexts to predict the instability of triples(e.g. Gupta et al. 2020; Perpinyà-Vallès et al. 2019; Tanikawa et al. 2020), and there are also some extensions, including the dependence of mass ratio m_2/m_1, mutual inclination $i_{\rm mut}$, and inner eccentricity $e_{\rm in}$ (e.g. Mylläri et al. 2018). Nevertheless, dynamical stability criteria only evaluate the stability of triples, and do not predict the disruption time in general.

2.3.2 Disruption time estimate model by the Random Walk energy transfer

In order to estimate the disruption times of triples, MK20 consider the Random-Walk-like energy transfer between inner and outer orbits. They consider very eccentric outer orbits ($e_{\rm out} \sim 1$), and use an approximate analytic formula of the energy transfer during the pericenter passages of a parabolic orbit by Roy & Haddow (2003).

The transferred energy depends on the inner mean anomaly during the next outer orbital pericenter. The Random Walk (RW) model assumes that the inner mean anomaly changes randomly between outer pericenter passages and the average energy exchange is zero. The resulting energy transfer processes therefore have the Random-Walk-like nature. Considering the RW model, they assume the disruption likely occurs when the accumulated transferred energy variance becomes comparable to the squared outer orbital energy. From this, they can estimate the disruption time of triples.

In the full RW model, they use numerical secular integration up to quadrupole interaction to include the effect of evolving orbital parameters. On the other hand, in the simplified RW model, they neglect the complicated evolution of orbital elements, and derive the following analytic expressions of disruption time $T_{\rm d}(e_{\rm out}, \alpha)$:

$$\begin{aligned} \frac{T_{\rm d}}{P_{\rm in}} &= 2\left(\frac{m_{123}}{\mu_{12}}\right)^2 (1-e_{\rm out})^{-3/2}\alpha^2 \exp\left(\frac{4\sqrt{2}}{3}\sqrt{\frac{m_{12}}{m_{123}}}(1-e_{\rm out})^{3/2}\alpha^{-3/2}\right) \\ &= 2\left(\frac{m_{123}}{\mu_{12}}\right)^2 (1-e_{\rm out})^{1/2}x^2 \exp\left(\frac{4\sqrt{2}}{3}\sqrt{\frac{m_{12}}{m_{123}}}x^{-3/2}\right), \end{aligned} \tag{2.41}$$

where $P_{\rm in}$ is the initial orbital period of inner binary, m_{123} is the total mass of system, m_{12} is the total mass of inner binary, μ_{12} is the inner reduced mass, α is the inner semi-major axis ratio over the outer one, $e_{\rm out}$ is the outer eccentricity, and x is defined as $\alpha(1-e_{\rm out})^{-1}$. Note that the factor 2 is heuristically determined from the numerical simulations. The RW model estimations can reasonably reproduce the disruption times from N-body numerical simulations within one order-of-magnitude difference for high-$e_{\rm out}$ triples in MK20. They perform the simulations for $e_{\rm out}$ between 0.1 and 0.9 by 0.2, and confirm that their models agree well with the simulations down to $e_{\rm out} = 0.7$ although the prediction accuracy decreases for lower eccentricities. Although the RW models estimate the disruption times reasonably, the effects of orbital evolution is only included numerically using the secular calculations. In chapter 6, we concentrate on prograde, orthogonal, and retrograde triples, and compare the simulated disruption times with the RW model estimations. We show there that the disruption time distribution is indeed very different even qualitatively from the RW model, especially for retrograde triples.

Chapter 3

Novel methods to detect inner BBHs I: short-term radial velocity variations

3.1 Introduction

In this chapter, we consider a coplanar triple consisting of an unseen inner binary and a tertiary star. The inner binary gravitational perturbation induces the short-term variations on the radial velocity (RV) of a tertiary star. We propose a method to search for an inner BBH in a triple system from the short-term RV variations of a tertiary star. We note that all the results here are based on HWS2020 and HS2020.

Our strategy is summarized in a schematic illustration in Figure 3.1. We first assume that a (star - unseen companion) binary will be discovered by the large-scale surveys such as Gaia and TESS. At first, it should not be clear if an unseen companion is really a single or an unseen inner binary. Therefore, we consider to perform intensive follow-up RV monitoring, and if the short-term RV variations are indeed detected, we can conclude that an unseen companion is an inner binary in reality. In this chapter, we show that our strategy works well through numerical simulations.

First, We summarize the analytic approximate RV formula for a coplanar circular triple by Morais & Correia (2008), and explain the features of the RV variations induced by an inner unseen binary.

We next show that the expected variations are indeed extracted if we subtract the base-line Kepler motions by fittings appropriately. We here compare the extracted RV residuals with the analytic approximation formulae. Then, we perform mock observations for coplanar triples following our strategy, and discuss the observational feasibility of our method.

Although the induced short-term RV variations have unique features, there would be the degeneracy between the RV from a S-type circumbinary planet when observational precision is limited. We also discuss a possible degeneracy between an inner-binary perturbation and a S-type circumbinary planet. We here show that eccentrici-

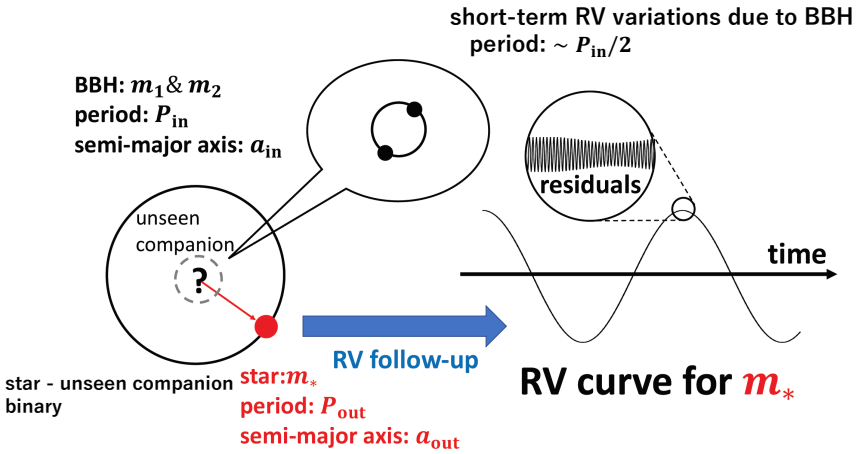

Figure 3.1 A schematic illustration for a methodology to search for inner BBHs using the RV variations of a tertiary star. Adapted from HWS2020.

ties play an important role to break the degeneracy. In appendix, we further discuss the parameter correspondence between the inner binary and a S-type circumbinary planet interpretations, if these two interpretations are degenerate.

3.2 Short-term RV variations for a coplanar circular triple: analytic approximate formula

In this section, we first present an approximation formula for short-term RV variations for a coplanar circular triple with an inner binary, which was derived by Morais & Correia (2008). The details of derivation is included in chapter 2. This analytic formula is useful to show basic feature of RV variations, and also to estimate the expected amplitude of RV variations in designing an RV followup strategy. As one example of application, we put a constraint on a possible inner unseen binary in a binary system 2M05215658+4359220. The result is included in the appendix.

We consider a coplanar circular hierarchical triple consisting of an inner binary and a star. The RV of the tertiary star orbiting around the inner binary (Morais & Correia 2008) is given by (see chapter 2)

$$\begin{aligned} V_{\rm RV} &\approx K_0 \left[1 + \frac{3}{4}\left(\frac{a_{\rm in}}{a_{\rm out}}\right)^2 \frac{m_1 m_2}{(m_1+m_2)^2}\right] \sin I \cos[\nu_{\rm out} t + \theta_0] \\ &- \frac{15}{16} K_{\rm BBH} \sin I \cos[(2\nu_{\rm in} - 3\nu_{\rm out})t + (2S_0 - \theta_0)] \\ &+ \frac{3}{16} K_{\rm BBH} \sin I \cos[(2\nu_{\rm in} - \nu_{\rm out})t + (2S_0 + \theta_0)], \end{aligned} \tag{3.1}$$

where I is the inclination of the stellar orbit axis with respect to the line of sight, $\nu_{\rm in}$ and $\nu_{\rm out}$ are mean motions of the inner and outer orbits, and S_0 and θ_0 are constant phases specified by the initial conditions.

The first term in the right-hand-side of equation (3.1) corresponds to the modulated Keplerian motion of the star. The semi-amplitude of the unperturbed Keplerian RV for a edge-on view is given by

$$K_0 \equiv \frac{m_1 + m_2}{m_1 + m_2 + m_*} a_{\rm out} \nu_{\rm out}, \tag{3.2}$$

where m_1, m_2 and m_* are the masses of the inner binary and the outer star, and $a_{\rm out}$ is the semi-major axis of the stellar orbit.

The second and third terms express the RV variations induced by an inner binary. The semi-amplitude of the variations is proportional to $K_{\rm BBH}$ defined as

$$K_{\rm BBH} \equiv \frac{m_1 m_2}{(m_1 + m_2)^2} \sqrt{\frac{m_1 + m_2 + m_*}{m_1 + m_2}} \left(\frac{a_{\rm in}}{a_{\rm out}} \right)^{3.5} K_0 \tag{3.3}$$

with $a_{\rm in}$ being the semi-major axis of the inner binary.

Equation (3.1) indicates that the RV variations due to an inner binary consist of two periodic terms with frequencies of $2\nu_{\rm in} - \nu_{\rm out}$ and $2\nu_{\rm in} - 3\nu_{\rm out}$. Since we consider a hierarchical system with $\nu_{\rm in} \gg \nu_{\rm out}$ ($a_{\rm in} \ll a_{\rm out}$), $K_{\rm BBH}$ is much smaller than K_0 by a factor of $(a_{\rm in}/a_{\rm out})^{3.5}$, and their frequencies are well approximated by $2\nu_{\rm in}$. Thus, it is not easy to identify the two distinct modes observationally.

Nevertheless, Morais & Correia (2008) pointed out that the separation of the two modes is crucial to distinguish the RV variation of the inner binary against a single periodic modulation induced by a planet orbiting the star. When two stars form a binary system and a planet orbits around one of those stars (a S-type circumbinary planet), we expect the RV signals of the star consists of the long-term and superposed short-term Keplerian motions. Thus, a S-type circumbinary planet would produce a signal very similar to that expected for an inner binary in a triple system.

We discuss the degeneracy between these two interpretations in section 3.6. In turn, a detection of an inner binary requires a well-organized observational monitor with short-cadence as we discuss later.

3.3 Numerical setup for simulations

In this section, we describe our methodology to extract the short-term RV variations from the total RV, and search for a possible inner binary in a star – BH system.

The comparison of the residual RV variations against the analytic approximate solutions are presented in the next section. Since there are many parameters characterizing a triple system, we cannot explore an entire parameter space. Instead, we fix fiducial models, and examine the feasibility of our method for the models.

In order to obtain the simulated RV data, we perform N-body simulations for a set of triple configurations (Table 3.1), using a public N-body package `REBOUND` (Rein

Table 3.1. Simulation models

model	$I_{\rm out}$ (deg)	$I_{\rm in}$ (deg)	$i_{\rm mut}$ (deg)	m_1 ($M_\odot$)	m_2 ($M_\odot$)	$e_{\rm in}$
P1010	90	90	0	10	10	10^{-5}
PE1010	90	90	0	10	10	0.2
R1010	90	270	180	10	10	10^{-5}
P0218	90	90	0	18	2	10^{-5}
PE0218	90	90	0	18	2	0.2
R0218	90	270	180	18	2	10^{-5}

Note. — P, PE, and R indicate prograde, prograde eccentric, and retrograde orbits.

Table 3.2. Initial values of the common parameters

parameter	initial value
orbital period $P_{\rm out}$	78.9 days
orbital period $P_{\rm in}$	10.0 days
eccentricity $e_{\rm out}$	0.03
argument of pericenter $\omega_{\rm in}$	0 deg
argument of pericenter $\omega_{\rm out}$	0 deg
longitude of ascending node $\Omega_{\rm in}$	0 deg
longitude of ascending node $\Omega_{\rm out}$	0 deg
true anomaly $f_{\rm in}$	30 deg
true anomaly $f_{\rm out}$	120 deg
tertiary mass m_*	3 $M_\odot$
inner binary mass $m_1 + m_2$	20 $M_\odot$

& Liu 2012). The fixed initial conditions of simulations throughout the models are summarized in Table 3.2. Note that we only consider coplanar systems here since the long-term RV variations show more feasibly the signature of inner BBHs for inclined systems. This is extensively discussed in the next chapter. Although we only consider very narrow range of initial conditions here, the conclusion is all the same qualitatively regardless of the specific choice of the parameters.

We use WHFast integrator (Rein & Tamayo 2015), which is one of the fast and accurate symplectic integrators, and set the calculation time interval to be 10^{-6} yr$/2\pi$. We run each model and output the snapshots every 0.1 day over $0 < t < 1000P_{\rm out}^{(0)}$, with $P_{\rm out}^{(0)} = 78.9$ days being the input orbital period of the outer star. We confirmed that all the systems remain gravitationally bound and stable at least within $1000P_{\rm out}^{(0)}$.

While our analysis is based on purely Newtonian gravity, we made sure that the correction due to general relativity (GR) does not change the conclusions here by repeating a set of runs using `REBOUNDx` (Tamayo et al. 2020), the extended package of `REBOUND`, with GR effects `gr_full` (Newhall et al. 1983).

Since we are looking for tiny RV variations relative to a much larger quasi-Keplerian component, we need to determine the base-line quasi-Keplerian motion accurately and subtract it from the total RV. Although it may seem a trivial and straightforward procedure, it is not the case in reality.

In the three-body problem, all the orbital parameters evolve with time unlike the two-body problem. The information of the inner BBH imprinted in the RV variations can be reproduced only when if the quasi-Keplerian RV component is properly extracted. While equation (3.1) provides a reasonably good approximation as discussed later, it does not incorporate the back-reaction from the outer star, and cannot be directly applied to estimate the quasi-Keplerian RV component.

Figure 3.2 plots the total RV of the prograde, coplanar and circular case P1010 for $100 < t/P_{\rm out}^{(0)} < 120$. In order to avoid a possible initial transient behavior, we examine the evolution of the systems at $t \geq 100P_{\rm out}^{(0)}$. The black dots and magenta dashed line indicate the simulation output and an analytic approximation by Morais & Correia (2008). For the latter, we evaluate the orbital variables at $t = 100P_{\rm out}^{(0)}$, and substitute those instantaneous values in equation (3.1). As expected, Figure 3.2 shows that the the total RV is dominated by the Keplerian motion, but the corresponding instantaneous period $P_{\rm out}(t)$ from simulations is clearly smaller than $P_{\rm out}^{(0)}$. Note that the orbital period evaluating with the instantaneous orbital elements at $t = 100P_{\rm out}^{(0)}$ does not differ much from $P_{\rm out}^{(0)}$.

Therefore, we use a public code `RadVel` (Fulton et al. 2018), and estimate the best-fit Keplerian motion by fitting the simulated RV data. We use the best-fit Keplerian motion as the baseline, and compute the residual RV variations, perform the Lomb-Scargle (LS) periodogram analysis, and compare with the approximate analytic results. Figure 3.3 shows the resulting best-fit values of $P_{\rm out}(t_n \equiv nP_{\rm out}^{(0)})$ over $100 \leq n < 200$ for P1010, R1010, and PE1010, in which each fitting is performed over one $P_{\rm out}^{(0)}$. The decrease of $P_{\rm out}(t)$ from its input value $P_{\rm out}^{(0)}$ is understood using the secular approximation, and discussed in the appendix.

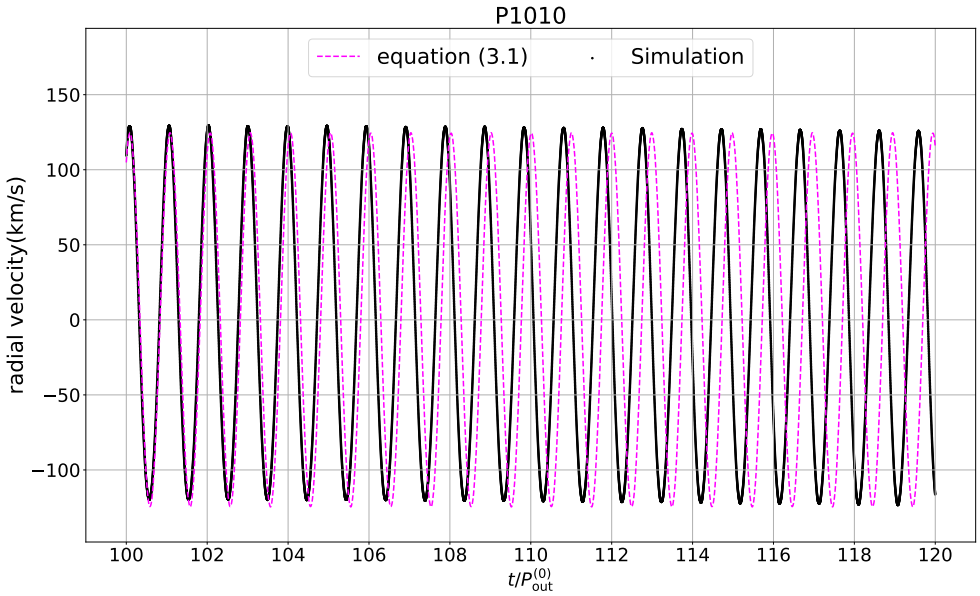

Figure 3.2 Radial velocity(P1010) with 0.1-day cadence. The black points and magenta dashed line denote the simulated RV data and RV approximate formula (equation (3.1)) evaluated at $t = 100P_{\rm out}^{(0)}$, respectively. Adapted from HS2020.

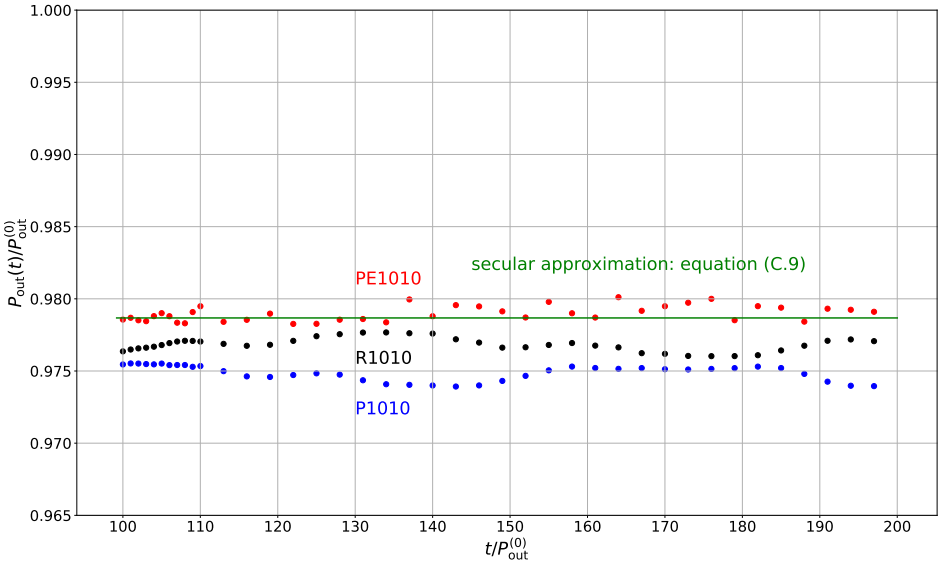

Figure 3.3 Best-fit values of $P_{\rm out}(t_n \equiv nP_{\rm out}^{(0)})$ for coplanar systems. They are estimated with `RadVel` using the 0.1-day cadence simulated RV data over $nP_{\rm out}^{(0)} < t < (n+1)P_{\rm out}^{(0)}$ for $100 \leq n < 200$; P1010 (blue), R1010 (black), and PE1010 (red). The solid green line indicates the analytic prediction that incorporate the average time-derivative of the argument of pericenter $\omega_{\rm out}(t)$ and the initial true anomaly $f_{\rm out,0}(t)$. Adapted from HS2020.

In summary, our strategy is to empirically remove the quasi-Keplerian RV component by local fitting of the data, instead of using the analytical template. Then we estimate $P_{\rm out}(t_{100})$ with `RadVel`, and remove the corresponding Keplerian component from the data. We analyze the residual RV variations using the LS periodogram to search for the signal due to the inner binary. The choice of $100P_{\rm out}^{(0)} < t < 101P_{\rm out}^{(0)}$ is arbitrary, and we made sure that our main conclusion below is not affected by the choice of the epoch at all.

3.4 Comparison with analytic approximation formulae

In this section, we compare the resulting residual RV variations with the analytic formulae using the time domain analysis and the Lomb-Scargle periodogram. First, we concentrate on coplanar near-circular cases, and next extend the result for eccentric systems. We here confirm that the residual RV variations after empirically removing the base-line Kepler motion indeed include the information of inner binary expected from the analytic approximate formulae.

3.4.1 Coplanar, near-circular cases

The residual RV variations after removing the empirically fitted Keplerian component are plotted in Figure 3.4. Top, middle, and bottom panels correspond to P1010 (prograde and equal-mass binary), R1010 (retrograde and equal-mass binary), and P0218 (prograde and unequal-mass binary), respectively. The Lomb-Scargle (LS) periodogram are calculated using a community-developed core Python package for Astronomy, `Astropy` (Astropy Collaboration et al. 2013, 2018).

Left panels indicate the RV variations of the simulation runs (dots) in the time domain every 0.1 days over $100P_{\rm out}^{(0)} < t < 101P_{\rm out}^{(0)}$. For comparison, magenta curves show the analytic approximation:

$$
\begin{aligned}
V_{\rm BBH,i}(t) &= -\frac{15}{16}K_{\rm BBH}^{\rm (i)}\cos[\nu_{\mp3}^{\rm (i)}t + 2(f_{\rm in,0}^{\rm (i)}+\omega_{\rm in}^{\rm (i)}) \mp 3(f_{\rm out,0}^{\rm (i)}+\omega_{\rm out}^{\rm (i)})] \\
&\quad + \frac{3}{16}K_{\rm BBH}^{\rm (i)}\cos[\nu_{\mp1}^{\rm (i)}t + 2(f_{\rm in,0}^{\rm (i)}+\omega_{\rm in}^{\rm (i)}) \mp (f_{\rm out,0}^{\rm (i)}+\omega_{\rm out}^{\rm (i)})], \qquad (3.4) \\
\nu_{\mp3}^{\rm (i)} &\equiv 2\nu_{\rm in}^{\rm (i)} \mp 3\nu_{\rm out}^{\rm (i)}, \qquad (3.5) \\
\nu_{\mp1}^{\rm (i)} &\equiv 2\nu_{\rm in}^{\rm (i)} \mp \nu_{\rm out}^{\rm (i)}, \qquad (3.6)
\end{aligned}
$$

where the minus and plus signs are for prograde and retrograde orbits, respectively. We introduce the superscript (i) so as to indicate instantaneous orbital elements evaluated at $t_{\rm i} = 100P_{\rm out}^{(0)}$.We evaluate equation (3.4) using the instantaneous orbital elements at $t_{\rm i}$ rather than their input values (Table 3.2). This is necessary to accurately estimate the phases $f_{\rm in,0}^{\rm (i)}+\omega_{\rm in}^{\rm (i)}$ and $f_{\rm out,0}^{\rm (i)}+\omega_{\rm out}^{\rm (i)}$ in order for the numerical results to reproduce the approximate formula.

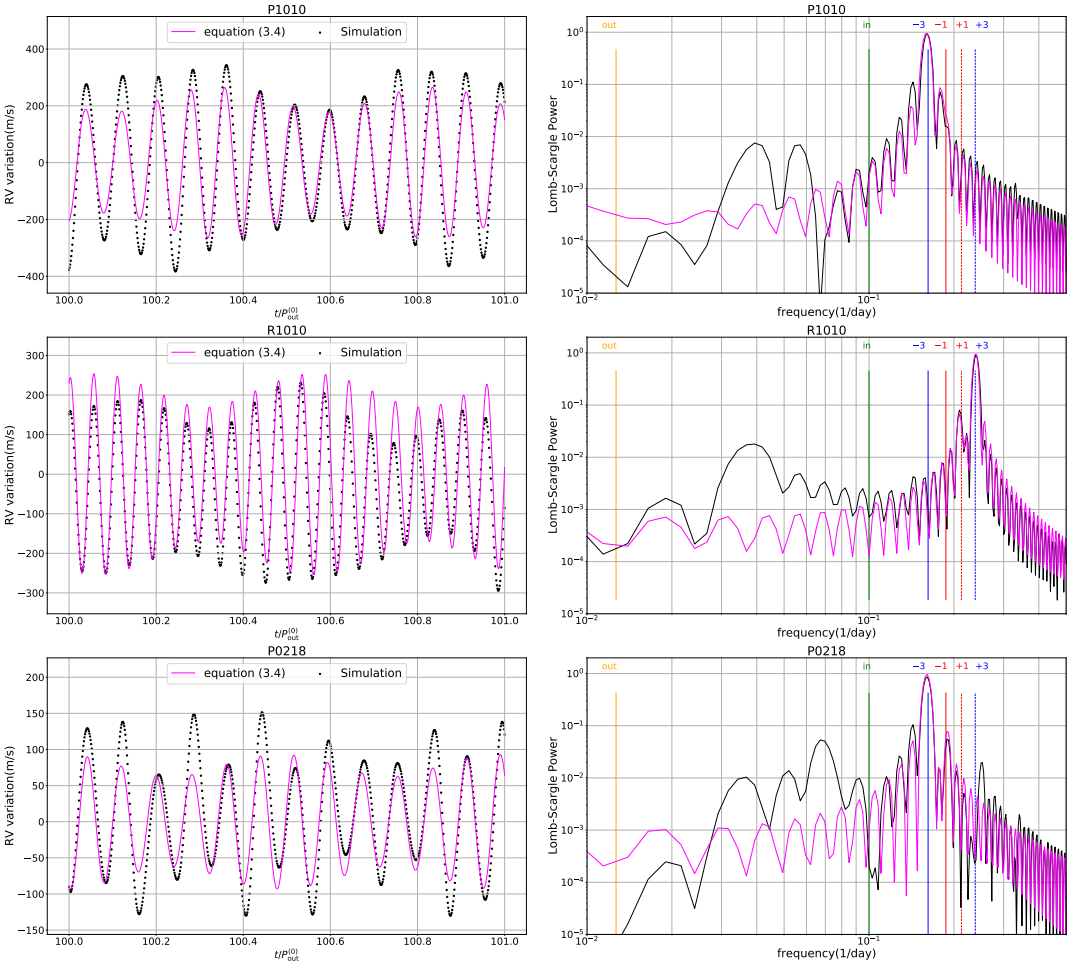

Figure 3.4 RV variations for P1010, R1010, and P0218 with 0.1-day cadence: time series (left) and LS periodograms (right). The black points indicate the simulated RV variation determined with `RadVel`. The magenta lines show the approximate prediction for the RV variation, equation (3.4). In the right panels, the locations of the frequencies at $\nu_{\rm out}^{(0)}$, $\nu_{\rm in}^{(0)}$, $\nu_{-3}^{(0)}$, $\nu_{-1}^{(0)}$, $\nu_{+1}^{(0)}$, and $\nu_{+3}^{(0)}$ are indicated by vertical lines labeled by out, in, -3, -1, +1, +3, respectively. Adapted from HS2020.

Equation (3.4) reproduces the amplitudes of the RV variations from the simulations (left panels in Figure 3.4) reasonably well. Note that the simulated RV variations are dependent on the empirically removed quasi-Keplerian component, while equation (3.4) is the lowest-order perturbation approximation neglecting the back-reaction of the outer star on the inner orbit. Therefore, the discrepancy between the two should not be regarded as serious.

Nevertheless, the corresponding LS periodograms (right panels in Figure 3.4) clearly detect the presence of the periodic components due to the inner binary expected from the approximate formula, especially at the frequencies of $\nu_{-3}^{(0)}$ and $\nu_{+3}^{(0)}$ for prograde and retrograde orbits, respectively. Furthermore, the lower-amplitude peak at the accompanying frequency ($\nu_{-1}^{(0)}$ or $\nu_{+1}^{(0)}$) can infer in principle whether the inner and outer orbits are prograde or retrograde. The agreement between the simulations and predictions is degraded for frequencies less than $\nu_{\rm in}^{(0)}$, which likely results from the uncertainty of the empirical removal of the underlying quasi-Keplerian RV component, as mentioned in the above. The LS periodograms prove, however, that the frequency modes at $\nu_{\pm3}^{(0)}$ and $\nu_{\pm1}^{(0)}$ are fairly robust against the removal procedure.

Incidentally, the agreement between the simulation and predictions seems worse for the unequal-mass binary case (P0218). This is supposed to come from the higher-order perturbation effect; larger mass difference of the binary enhances the octupole (e.g. Mardling 2013), which is neglected in the approximation by Morais & Correia (2008).

3.4.2 Effect of the eccentricity of the inner binary

It is expected that both $e_{\rm in}$ and $e_{\rm out}$, eccentricities of the inner and outer orbits, sensitively change the RV variations. For simplicity, we only consider the effect of $e_{\rm in}$ here although the $e_{\rm out}$ could be very eccentric in practice. The effect of outer eccentricity $e_{\rm out}$ is discussed in the next section when we perform the mock observation.

According to the formation scenarios, the $e_{\rm in}$ is expected to be not so large for BBHs that we are primarily interested in, because of the circularization due to the emission of the gravitational wave, especially for those with a short orbital period. Therefore we focus on the effect of relatively small $e_{\rm in}$ on the RV variation of the tertiary star in coplanar triple systems.

Morais & Correia (2011) have derived an analytic approximation for the RV variation in a coplanar eccentric triple, to the lower-order of $e_{\rm in}$ and $e_{\rm out}$:

$$V_{\rm RV}(t) = V_{\rm Kep}^{(0)}(t) + \delta V_{\rm Kep}(t) + V_{\rm BBH}(t), \tag{3.7}$$

where $V_{\rm Kep}^{(0)}(t)$ is the unperturbed Keplerian radial velocity, and $\delta V_{\rm Kep}(t)$ in a coplanar eccentric case is now written as

$$\delta V_{\rm Kep}(t) \;=\; \frac{3}{4} K_0 \left(\frac{a_{\rm in}}{a_{\rm out}}\right)^2 \frac{m_1 m_2}{(m_1+m_2)^2} \sin I_{\rm out} \cos\left(\nu_{\rm out}\, t + \lambda_{\rm out,0}\right), \tag{3.8}$$

in terms of the initial mean longitude $\lambda_{j,0}$. We use the subscript j to refer inner and outer orbital elements, *i.e.* j = in or out. The true anomaly f_j and argument of

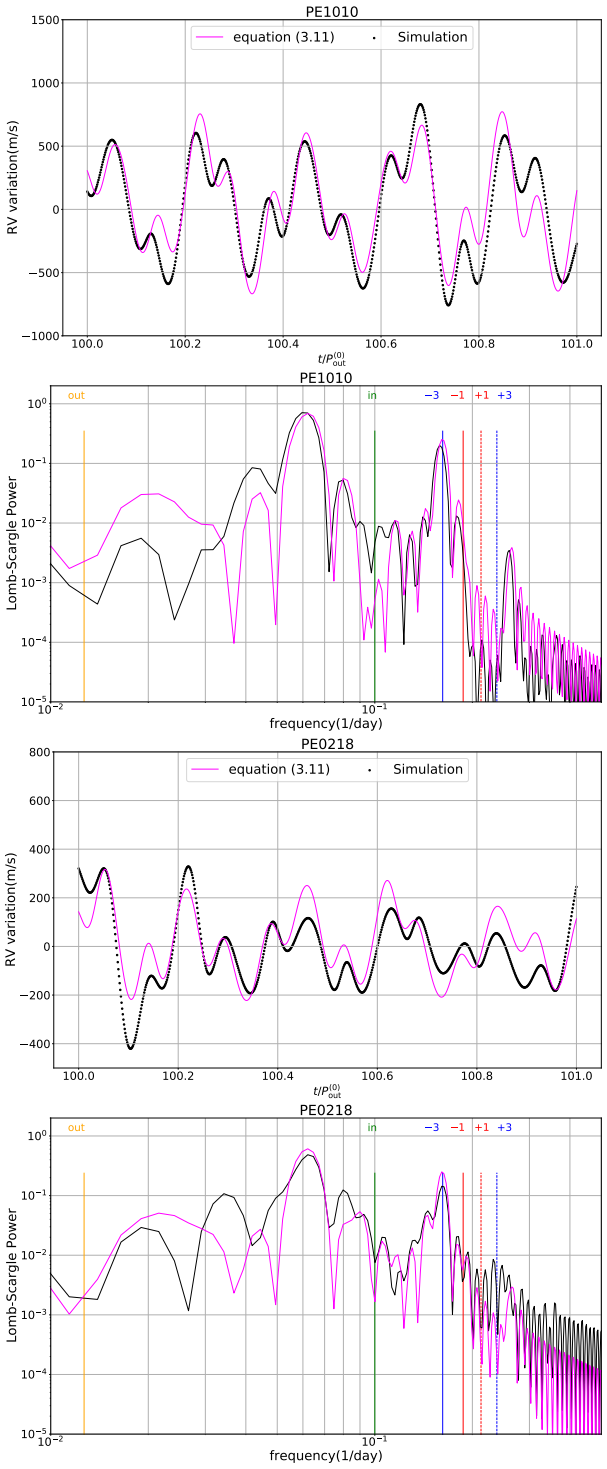

Figure 3.5 Same as Figure 3.4 but for PE1010 and PE0218. The magenta lines show the approximate formula (equation (3.11)) evaluated at $t = 100P_{\rm out}^{(0)}$. The phase and constant offsets $(\delta t, C)$ are empirically determined to match simulated residuals: $(\delta t, C) = (+0.115P_{\rm out}^{(0)}, -480.0)$ and $(-0.27P_{\rm out}^{(0)}, -430.0)$ for PE1010 and PE0218, respectively. Adapted from HS2020.

pericenter ω_j can be expanded in terms of the small eccentricity e_j as

$$f_j + \omega_j = \lambda_j + 2e_j \sin(\lambda_j - \omega_j) + \mathcal{O}(e_j^2), \tag{3.9}$$

(e.g. Murray & Dermott 2000). Thus $f_j + \omega_j$ is identical to λ_j for a circular case, and the first term of equation (3.1) reduces to equation (3.8). In an eccentric case, however, equation (3.9) is necessary to clarify the effect of the eccentricities in a perturbative manner.

An analytic approximation for $V_{\rm bin}(t)$ in equation (3.7) is derived by Morais & Correia (2011), which is explicitly written as

$$\begin{aligned}
V_{\rm BBH}^{\rm MC}(t) &= \frac{3}{8} K_{\rm BBH} \sin I_{\rm out} \left[\frac{\nu_{\rm in}}{2\,\nu_{\rm in} - \nu_{\rm out}} \cos[(2\,\nu_{\rm in} - \nu_{\rm out})\,t + 2\,\lambda_{\rm in,0} - \lambda_{\rm out,0}] \right. \\
&- \frac{5\,\nu_{\rm in}}{2\,\nu_{\rm in} - 3\,\nu_{\rm out}} \cos[(2\,\nu_{\rm in} - 3\,\nu_{\rm out})\,t + 2\,\lambda_{\rm in,0} - 3\,\lambda_{\rm out,0}] \\
&+ 15\,e_{\rm in} \frac{\nu_{\rm in}}{\nu_{\rm in} - 3\,\nu_{\rm out}} \cos[(\nu_{\rm in} - 3\,\nu_{\rm out})\,t + \lambda_{\rm in,0} - 3\,\lambda_{\rm out,0} + \varpi_{\rm in}] \\
&+ e_{\rm in} \frac{\nu_{\rm in}}{3\,\nu_{\rm in} - \nu_{\rm out}} \cos[(3\,\nu_{\rm in} - \nu_{\rm out})\,t + 3\,\lambda_{\rm in,0} - \lambda_{\rm out,0} - \varpi_{\rm in}] \\
&- 5\,e_{\rm in} \frac{\nu_{\rm in}}{3\,\nu_{\rm in} - 3\,\nu_{\rm out}} \cos[(3\,\nu_{\rm in} - 3\,\nu_{\rm out})\,t + 3\,\lambda_{\rm in,0} - 3\,\lambda_{\rm out,0} - \varpi_{\rm in}] \\
&- 2\,e_{\rm in} \frac{\nu_{\rm in}}{\nu_{\rm in} + \nu_{\rm out}} \cos[(\nu_{\rm in} + \nu_{\rm out})\,t + \lambda_{\rm in,0} + \lambda_{\rm out,0} - \varpi_{\rm in}] \\
&- 3\,e_{\rm in} \frac{\nu_{\rm in}}{\nu_{\rm in} - \nu_{\rm out}} \cos[(\nu_{\rm in} - \nu_{\rm out})\,t + \lambda_{\rm in,0} - \lambda_{\rm out,0} + \varpi_{\rm in}] \\
&+ 2\,e_{\rm in} \frac{\nu_{\rm in}}{\nu_{\rm in} - \nu_{\rm out}} \cos[(\nu_{\rm in} - \nu_{\rm out})\,t + \lambda_{\rm in,0} - \lambda_{\rm out,0} - \varpi_{\rm in}] \\
&+ 6\,e_{\rm out} \frac{\nu_{\rm in}}{2\,\nu_{\rm out}} \cos\left(2\,\nu_{\rm out}\,t + 2\,\lambda_{\rm out,0} - \varpi_{\rm out}\right) \\
&+ e_{\rm out} \frac{\nu_{\rm in}}{2\,\nu_{\rm in}} \cos\left(2\,\nu_{\rm in}\,t + 2\,\lambda_{\rm in,0} - \varpi_{\rm out}\right) \\
&- 25\,e_{\rm out} \frac{\nu_{\rm in}}{2\,\nu_{\rm in} - 4\,\nu_{\rm out}} \cos[(2\,\nu_{\rm in} - 4\,\nu_{\rm out})\,t + 2\,\lambda_{\rm in,0} - 4\,\lambda_{\rm out,0} + \varpi_{\rm out}] \\
&+ 3\,e_{\rm out} \frac{\nu_{\rm in}}{2(\nu_{\rm in} - \nu_{\rm out})} \cos[(2(\nu_{\rm in} - \nu_{\rm out})t + 2(\lambda_{\rm in,0} - \lambda_{\rm out,0}) + \varpi_{\rm out}] \\
&+ \left. \frac{5\,e_{\rm out}\nu_{\rm in}}{2(\nu_{\rm in} - \nu_{\rm out})} \cos[(2(\nu_{\rm in} - \nu_{\rm out})t + 2(\lambda_{\rm in,0} - \lambda_{\rm out,0}) - \varpi_{\rm out}] \right] ,
\end{aligned} \tag{3.10}$$

where $\varpi_j = \omega_j + \Omega_j$.

In reality, however, our simulation results have an uncertain offset relative to equation (3.10), and thus we model $V_{\rm bin}(t)$ as

$$V_{\rm bin}(t) = V_{\rm bin}^{\rm MC}(t) - V_{\rm bin}^{\rm MC}(0) + V_0 + C. \tag{3.11}$$

In equation (3.11), we define V_0 as the initial velocity of the RV variation, and C is an additional constant discussed below.

We first fit the simulation data using `RadVel` to obtain $V_{\rm Kep}^{(0)}(t) + \delta V_{\rm Kep}(t)$ at $t = t_{\rm i} = 100 P_{\rm out}^{(0)}$. Thus the residual RV variation from the simulation should correspond

parameter	initial value
semi-major axis $a_{\rm in}$	1.0 au
semi-major axis $a_{\rm out}$	4.0 au
mass of the primary m_1	10 $M_\odot$
mass of the secondary m_2	10 $M_\odot$
mass of the tertiary m_*	1 $M_\odot$
inclinations $I_{\rm in}, I_{\rm out}$	90 deg
arguments of pericenter $\omega_{\rm in}, \omega_{\rm out}$	0 deg
longitudes of ascending node $\Omega_{\rm in}, \Omega_{\rm out}$	0 deg
true anomaly $f_{\rm in}$	30 deg
true anomaly $f_{\rm out}$	120 deg

Table 3.3 Initial values of parameters for our fiducial triple.

to $V_{\rm bin}(t)$. We also evaluate all the orbital elements and V_0 at $t_{\rm i}$, whose values are substituted into equation (3.10). Since the quasi-Keplerian component estimated with our fitting procedure involves a time-average over an outer orbital period, the residual RV variation $V_{\rm bin}(t)$ from the simulation should inevitably have a time-shift relative to equation (3.10). Thus we introduce an empirical time-shift δt to match the analytical expression (3.10) and the simulation result. This matching simultaneously requires the additional velocity offset term C, which is introduced in equation (3.11).

Figure 3.5 shows the resulting plot of RV variations for PE1010 and PE0218. We find that the simulated RV variations in the left panel of Figure 3.5 agree well with the analytic approximation. Thus the presence of an inner binary can be detected even in a moderately eccentric coplanar system, as long as the observational data are sufficiently accurate to the level indicated in Figure 3.5.

3.5 Mock observations

The former sections confirm that we can use the residual short-term RV variation as a probe of inner unseen binary. In the present section, in order to examine the feasibility of our methodology, we perform mock observations of the RV signal including observational noise and finite sampling effect following our observational strategy. Since the long-term variations discussed in the next chapter provide a good probe for inclined systems, we concentrate on coplanar systems here.

Table 3.3 summarizes the initial values of parameters in our fiducial model for the mock observartions. We adopt a 1 $M_\odot$ star as the tertiary for simplicity. Also we assume a relatively large value for $(a_{\rm in}/a_{\rm out})$ within the dynamically stable range (Mardling & Aarseth 1999). As a reference, Table 3.4 lists the predicted values for orbital motions calculated from equation (3.1).

For definiteness, we consider four cases of different eccentricities: $(e_{\rm in}, e_{\rm out}) = (10^{-5}, 10^{-5})$, $(10^{-5}, 0.2)$, $(0.1, 10^{-5})$, and $(0.1, 0.2)$. The other parameters are fixed

parameter	value
orbital period $P_{\rm in}$	81.7 days
orbital period $P_{\rm out}$	638 days
semi-amplitude of Keplerian RV K_0	65.0 km/s
variation period (2nd term in eq.(3.1)) $P_{\rm var1}$	50.5 days
variation period (3rd term in eq.(3.1)) $P_{\rm var2}$	43.6 days
half an inner period $P_{\rm in}/2$	40.9 days
characteristic semi-amplitude of variations $K_{\rm BBH}$	130.1 m/s

Table 3.4 Predicted values for orbital motions calculated from equation (3.1) and Table 3.3.

as those listed in Table 3.3. We first generate the RV data in 0.1-day cadence over 800 days using `REBOUND`, and extract the base-line Keplerian motion fitted with `RadVel`. We use these data as the original RV variations before including observational noise and finite sampling effects.

Figure 3.6 shows the RV variations (*left*) and the corresponding Lomb-Scargle (LS) periodogram (*right*). The RV variation for a coplanar circular triple exhibits a clear periodic signal as shown in the top-left panel of Figure 3.6. According to equation (3.1), the variation should have two distinct frequencies $\nu_{\rm var1} \equiv 2\nu_{\rm in} - \nu_{\rm out}$, and $\nu_{\rm var3} \equiv 2\nu_{\rm in} - 3\nu_{\rm out}$, corresponding to

$$P_{\rm var1} = \frac{P_{\rm in}P_{\rm out}}{2P_{\rm out} - P_{\rm in}}, \tag{3.12}$$

and

$$P_{\rm var3} = \frac{P_{\rm in}P_{\rm out}}{2P_{\rm out} - 3P_{\rm in}}, \tag{3.13}$$

respectively. The LS periodograms in the top-right panel of Figure 3.6 indicates that the RV variation that we compute numerically is dominated by the mode with $\sim 1/P_{\rm var3} \approx 0.02$ day^{-1}, and the mode with $\sim 1/P_{\rm var1} \approx 0.023$ day^{-1} is barely visible. For comparison, we also computed the LS periodogram directly for the second and third terms of equation (3.1) with the same parameters and 0.1-day cadence over 800 days. We found that the secondary peak at $\nu_{\rm var1}$ is not visible either, but correctly reproduced only when the total base-line duration is significantly larger than the 800 days we adopted here. Therefore, the identification of the two distinct modes due to an inner binary is very challenging in practical observation.

The LS periodograms also imply that non-zero eccentricities generate a variety of additional frequency modes in the LS periodograms, and that the value of the frequency $\nu_{\rm var3}$ is fairly insensitive to $e_{\rm in}$, but decreases as $e_{\rm out}$ increases. The sensitivity of the RV variation curve in time domain, instead of the LS periodogram, on $e_{\rm in}$ and $e_{\rm out}$ may be useful to estimate those eccentricities of the system. Thus we conclude that the presence of the inner binary itself can be inferred robustly. Also we find that

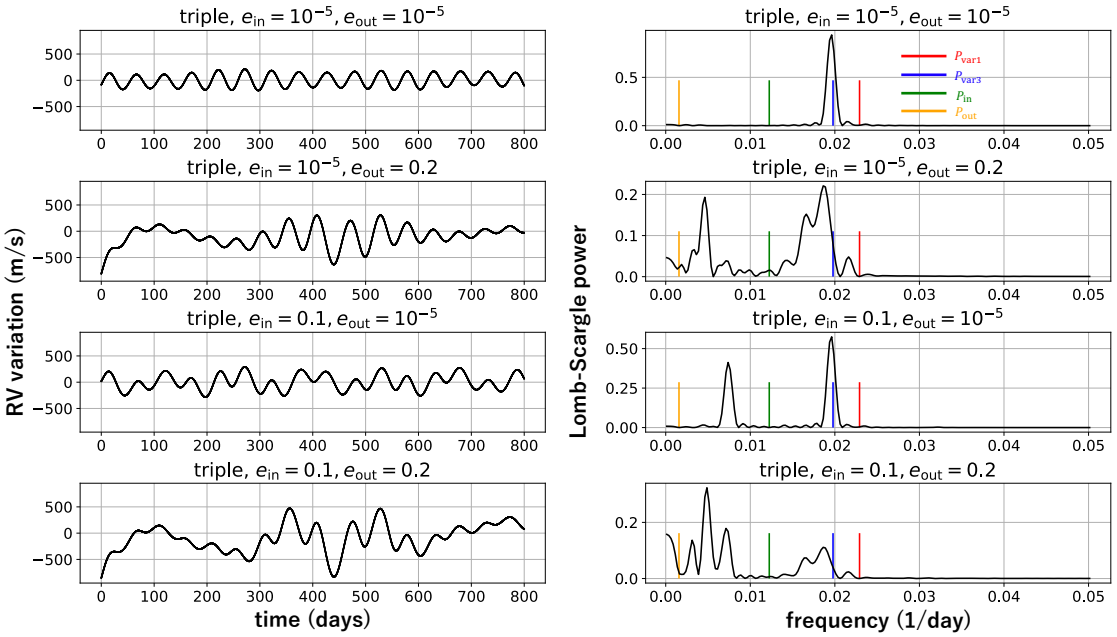

Figure 3.6 RV variations from numerical simulations: RV variation curves (*left*) and their Lomb-Scargle periodograms (*right*). For reference, the vertical lines in the right panel indicate relevant frequencies of the systems calculated from Table 3.4. Adapted from HWS2020.

the eccentricity is useful in distinguishing between the inner binary and the planetary signals as we discuss in section 3.6.

Then, we perform mock observations for irregularly sampled RV data from simulations including observational noises. If the tertiary star is a solar-type star located at ~ 1 kpc, the apparent magnitude is around 15. According to Plavchan et al. (2015), the statistical RV error is at the level of a few tens of m/s with an ideal 10m telescope with ~ 1000 second exposure. While the noise is crucially dependent on the nature of the star, we neglect any systematic/non-Gaussian noise, and add 20 m/s Gaussian noise into the RV signal.

The observational cadence also affects the detectability of the inner binary. We consider two different cases; 10 and 30 data points randomly selected from one-day cadence data over 100 days. In both cases, we assume that the same cadence data are available for 600 days. Then we fit the data over 600 days with `RadVel` to extract the base-line Keplerian component, and obtain the RV residuals.

The results are shown in Figure 3.7 for the 30 percent sampling rate, and in Figure 3.8 for the 10 percent sampling rate. Blue lines in the left panels of Figures 3.7 and 3.8 correspond to the original RV variation curves of Figure 3.6. We note that we add the noise on the *total* RV curve, instead of the RV variation curve (blue lines). Thus the extracted Keplerian component is not exactly the same depending on the Gaussian noise. This is why the data points in the left panels of the two figures do

parameter	initial value
semi-major axis $a_{\rm pl}$	0.27 au
semi-major axis $a_{\rm out}$	4.0 au
mass of the unseen companion $m_{\rm BH}$	20 $M_\odot$
mass of the star m_*	1 $M_\odot$
mass of the planet $m_{\rm pl}$	2.7 $M_{\rm J}$
inclinations $I_{\rm pl}, I_{\rm out}$	90 deg
arguments of pericenter $\omega_{\rm pl}, \omega_{\rm out}$	0 deg
longitudes of ascending node $\Omega_{\rm pl}, \Omega_{\rm out}$	0 deg
true anomaly $f_{\rm pl}$	30 deg
true anomaly $f_{\rm out}$	120 deg

Table 3.5 Initial values of parameters for a fiducial binary with an S-type circumbinary planet orbiting around the star.

not necessarily distribute around the blue lines. This clearly implies that an accurate determination and extraction of the base-line Keplerian component is crucial in our methodology.

Except for the limitation, Figures 3.7 and 3.8 indicate that the RV variations can clearly reveal the presence of the inner binary if the relevant short-cadence RV follow-up is performed. The LS periodograms in our mock data are very similar to the idealized cases shown in Figure 3.6; the peaks around the frequency $\nu_{\rm var3}$ are fair robust even in the (modest) eccentricities we assumed here.

While the inner binary orbital period can be inferred relatively easily, it would be difficult to determine the mass ratio m_2/m_1 of the binary. As equation (3.1) indicates, the RV variations are more insensitive to the mass ratio than to the inner binary separation. Even a small uncertainty of the amplitude due to noise would affect the estimate of the mass ratio.

3.6 Degeneracy with an S-type circumbinary planet

As mentioned in sections 3.1 and 3.2, an S-type circumbinary planet (see Figure 3.9) produces a RV variation similar to that due to an inner binary. We examine the degree of a possible degeneracy by performing mock observations presented in section 3.5.

We consider the configuration of a star– BH binary system with a planet around a star. We intentionally choose a set of parameters for a planet (Table 3.5) so as to mimic the RV variations produced by our fiducial triple model (Table 3.3). The details are discussed in the appendix. We also consider non-zero eccentricities of the planetary and stellar orbits: $(e_{\rm pl}, e_{\rm out}) = (10^{-5}, 10^{-5})$, $(10^{-5}, 0.2)$, $(0.1, 10^{-5})$, and $(0.1, 0.2)$. While we choose the same set of values for $(e_{\rm in}, e_{\rm out})$ in section 3.5, $e_{\rm in}$ and

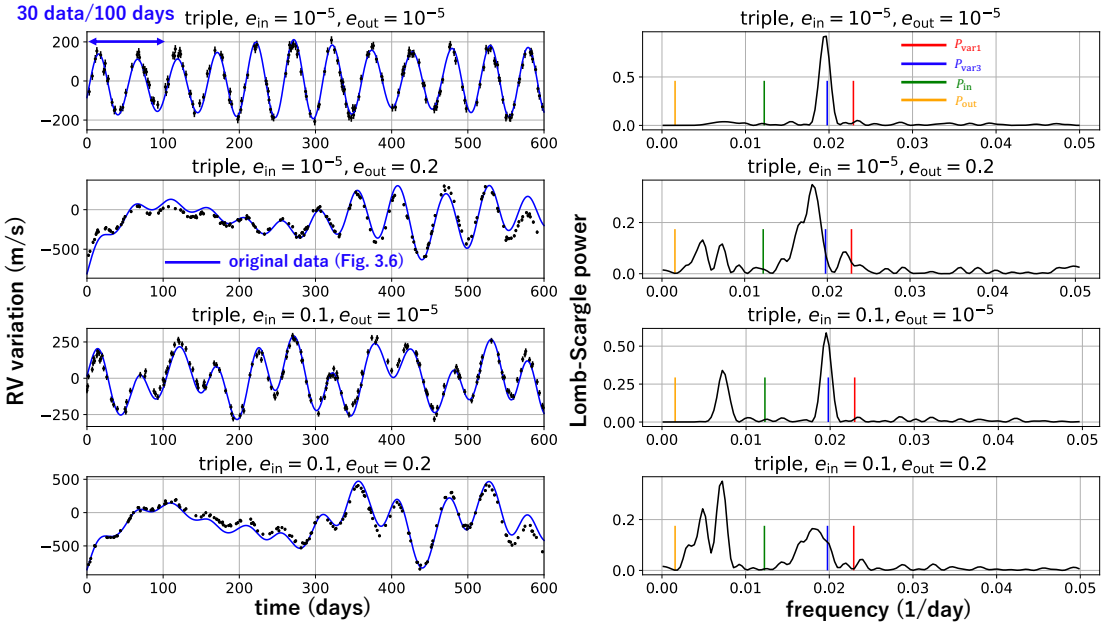

Figure 3.7 RV variation curves from mock observations of the original data plotted in Figure 3.6 and their LS periodograms. We sample 30 data points from each 100-days segment of the total RV data, add 20 m/s Gaussian noise, and extract the Keplerian component fitted to the 30×6 points over 600 days. Thin blue curves in the left panels correspond to the original data without noise plotted in Figure 3.6. The vertical lines in the right panels indicate relevant frequencies of the systems calculated from Table 3.4. Adapted from HWS2020.

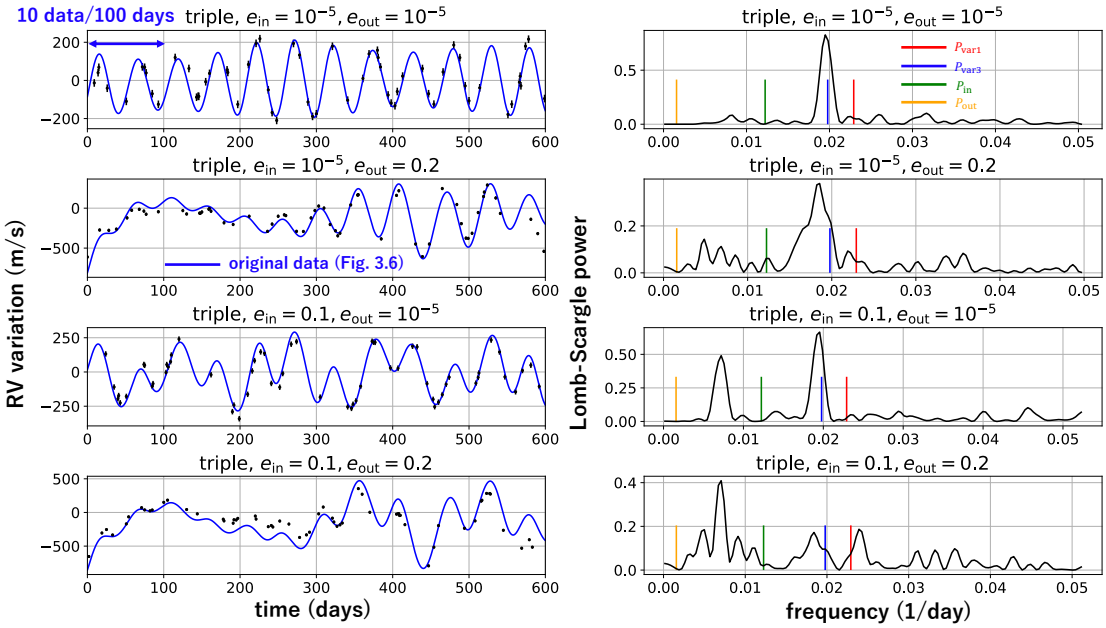

Figure 3.8 Same as Figure 3.7 but sampled 10 data points from each 100-days segment. Adapted from HWS2020.

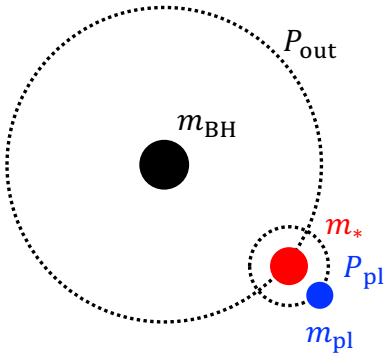

Figure 3.9 A binary consisting of a star and an unseen single BH. Adapted from HWS2020.

$e_{\rm pl}$ do not have to be the same value in the two different pictures. We then perform the mock observations similar in section 3.5. We here consider the 30 percent sampling rate and examine if we can distinguish between the two pictures observationally.

Figure 3.10 shows the resulting RV variations (*left*) and the LS periodograms (*right*) for star–BH binaries with a planet orbiting around the star. As expected, a circular inner binary (top panels in Figure 3.7) is difficult to be distinguished from a star with a planet. The RV variation curves due to a planet are not so much affected by $e_{\rm pl}$ nor $e_{\rm out}$, in contrast to their sensitivity due to an inner binary on $e_{\rm in}$ and $e_{\rm out}$ (Figure 3.7). Thus eccentricities of the inner binary is indeed helpful to break the degeneracy between the two models. In the appendix, we provide the parameter correspondence between the two possibilities for coplanar and circular systems.

3.7 Summary

In this chapter, we proposed a method to detect wider-separation BBHs expected as progenitors of BBH mergers through the short-term RV variations on a tertiary star orbiting around them. The radial velocity of the tertiary star in a star – BBH triple system exhibits a periodic variation due to the orbital motion of the inner BBH. We concentrated on coplanar triples, and showed that the short-term RV variations can be indeed extracted if the base-line Kepler motion is appropriately subtracted by RV fittings. The variation amplitudes are tiny compared with the Keplerian motion RV. For instance, our fiducial triple shows $\mathcal{O}(100)$ m/s variations, inside $\mathcal{O}(100)$ km/s Kepler motion RV. Nevertheless, we found that the amplitude is comparable to, or even larger than, a typical amplitude of the radial velocities for observed exoplanetary systems. Thus, such a velocity variation signal will be indeed detectable if such star-BBH triples exist.

In our observational strategy, we consider to perform the intensive follow-up observations for target (star - unseen companion) binaries, which will be discovered with the large-scale surveys such as Gaia and TESS. Therefore, the feasibility highly de-

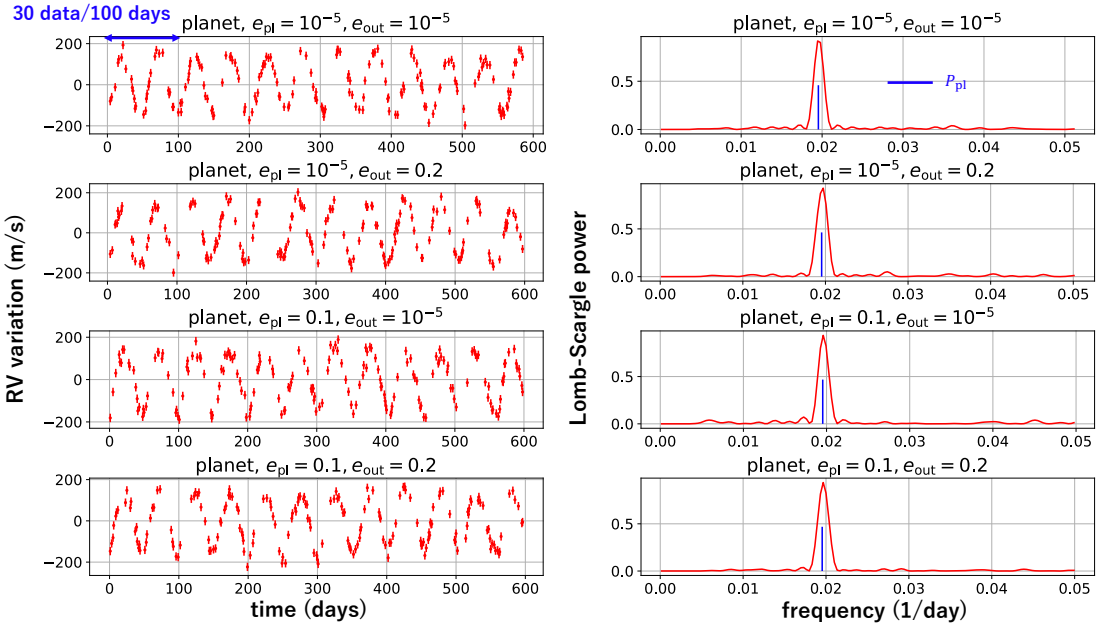

Figure 3.10 RV variations induced by an S-type circumbinary planet from mock observation based on the same parameters that are employed in Figure 3.7. Adapted from HWS2020.

pends on whether or not the intensive RV monitoring can identify the short-term RV variations clearly under observational limitations.

In order to address this issue, we generated a series of mock radial velocity curves for coplanar systems following the above strategy. We showed that an inner BBH can be indeed identified reasonably from the short-term RV variations as long as a target star is bright enough to allow for high-resolution spectroscopy, while the precise determination of BBH mass ratio would be difficult.

Finally, we also examined the possible degeneracy with S-type circumbinary planet orbiting a star, and showed that the eccentricity of the tertiary star is useful in breaking the degeneracy. Therefore, we concluded that the short-term RV variations provide a useful probe of inner BBHs for bright stars in most cases.

Chapter 4

Novel methods to detect inner BBHs II: long-term radial velocity variations

4.1 Introduction

In the previous chapter, we considered coplanar triple systems, and showed the short-term RV variations will provide a good probe of hidden inner BBHs in triple systems. In this chapter, we extend the method, and consider non-coplanar triple systems as well. We here examine the long-term RV variations, instead of the short-term RV variations. All the result here are based on HS2020.

For coplanar triples, we find that the precession of argument of pericenter is a useful probe of an inner hidden binary. Contrarily, for non-coplanar triples, we show that the long-term RV amplitude variations induced by the nodal precession and the ZKL oscillation are very effective to search for inner BBHs.

First, we consider the argument precessions for coplanar orbits, and compare the numerical simulations with the analytic secular approximation in Morais & Correia (2011). We show that if we determine the arguments of pericentre at each observational epoch by fittings, they reasonably satisfy the approximation formula. This method will be useful when the short-term RV variations are hardly detected due to observational condition.

Next, we consider non-coplanar triples using numerical simulations. We show that the Kepler motion RV amplitude changes significantly over roughly the ZKL timescale, due to the evolution of the outer orbital inclination. We show that the amplitude modulations can reach the same order of the Kepler motion RV itself. For instance, the modulations reach $\mathcal{O}(100)$ km/s for our fiducial triples. Therefore, they will be easily detected by RV observations.

Finally, we briefly discuss possible effects of the general relativistic corrections and the inverse-ZKL oscillations on our proposed method here. Although the effects possibly affect the stability of triples, we conclude here that they hardly change the

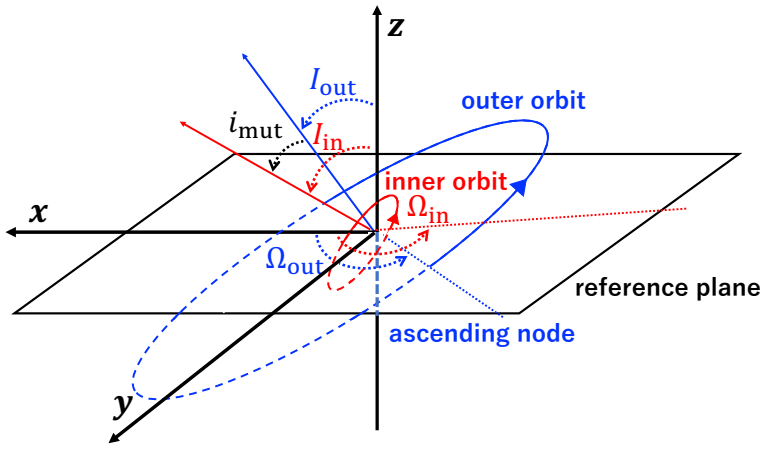

Figure 4.1 Schematic illustration of a triple system that we consider in the present chapter. The orbital angles are defined with respect to the reference Cartesian frame whose origin is set to be the barycenter of the inner orbit. Adapted from HS2020.

results basically.

4.2 Method

Figure 4.1 shows a schematic configuration of a triple system consisting of an inner BBH and an outer orbiting star. Note that we use the subscript $j(=$ in and out) to distinguish between those variables of the inner and outer orbits, respectively.

With respect to the reference coordinate system, the inner and outer orbits are specified by the instantaneous longitudes of the ascending nodes Ω_j, semi-major axes a_j, eccentricities e_j, arguments of pericenter ω_j, orbital inclinations I_j, and their mutual inclination $i_{\rm mut}$. Note that our reference plane in Figure 4.1 is arbitrary while it is often chosen as the invariant plane of the triple system.

As in the previous chapter, we fix our fiducial models that is summarized in Table 4.1. The other orbital parameters are fixed as in Table 3.2 in the previous chapter. In this chapter, we add non-coplanar cases (I and O) to show the long-term RV modulations provide significant probes of inner hidden binaries. Although we only consider very narrow range of orbital parameters, the qualitative conclusions hardly change for different choices of parameters.

We perform N-body simulations for a set of triple configurations (Table 4.1) with N-body package `REBOUND` (Rein & Liu 2012). We use `WHFast` integrator (Rein & Tamayo 2015) with a time-step of 10^{-6} yr$/2\pi$, and output the snapshots every 0.1 day over $0 < t < 1000P_{\rm out}^{(0)}$, with $P_{\rm out}^{(0)} = 78.9$ days being the input orbital period of the outer star.

We confirmed that all the systems remain gravitationally bound and stable at least within $1000P_{\rm out}^{(0)}$. It is also confirmed that the GR corrections do not change the

Table 4.1. Simulation models

model	$I_{\rm out}$ (deg)	$I_{\rm in}$ (deg)	$i_{\rm mut}$ (deg)	m_1 ($M_\odot$)	m_2 ($M_\odot$)	$e_{\rm in}$
P1010	90	90	0	10	10	10^{-5}
PE1010	90	90	0	10	10	0.2
R1010	90	270	180	10	10	10^{-5}
O1010	0	90	90	10	10	10^{-5}
I1010	0	45	45	10	10	10^{-5}
P0218	90	90	0	18	2	10^{-5}
PE0218	90	90	0	18	2	0.2
R0218	90	270	180	18	2	10^{-5}
O0218	0	90	90	18	2	10^{-5}
I0218	0	45	45	18	2	10^{-5}

Note. — P, PE, R, O and I indicate prograde, prograde eccentric, retrograde, orthogonal and inclined orbits.

conclusions here using `REBOUNDx` (Tamayo et al. 2020) although our analysis is based on purely Newtonian Gravity. The discussion on the effects of GR corrections are included in the appendix.

In order to determine the base-line Keplerian motion in the simulated RV data, we use the public RV fitting code `RadVel` (Fulton et al. 2018). As in the previous chapter, we examine the evolution of the systems at $t \geq 100 P_{\rm out}^{(0)}$ when possible initial transient behavior goes away.

4.3 Long-term RV variations

In this section, we show how the total RV is modified in the long-term timescale, and how the modulations indicate the presence of inner unseen binary. First, we examine the precession of argument of pericenter for coplanar triples. Next, we move on to the long-term RV amplitude variations for non-coplanar systems.

4.3.1 Precession of the argument of pericenter $\omega_{\rm out}$ for coplanar systems

The analytic approximate RV formula (see equation 3.1) assumes both the outer mean motion $\nu_{\rm out}$ and the argument of pericenter $\omega_{\rm out}$ are constant. In reality, however, they are dependent on time due to the perturbation from the inner binary. The

variation of $\omega_{\rm out}$ changes the location of pericenter, and therefore the shape of RV curves slightly. Therefore, it is expected that the variations are detected from long-term RV observations.

Figure 4.2 plots $\omega_{\rm out}(t)$ from the 0.1-day cadence output of our `REBOUND` run for P1010, PE1010, R1010, and P0218. It is clearly visible that $\omega_{\rm out}(t)$ exhibits periodic modulations with frequency roughly corresponding to $\nu_{\rm out}$ and $\nu_{\rm in}$, in addition to the monotonic increase as t. In order to remove the oscillation components, we compute the time-average of $\omega_{\rm out}$ over $nP_{\rm out}^{(0)} < t < (n+1)P_{\rm out}^{(0)}$ using `RadVel`, and plot the best-fit values $\langle\omega_{\rm out}\rangle$ in solid circles at $t = t_n \equiv nP_{\rm out}^{(0)}$.

Using the secular perturbation approximation, the time-derivative of $\omega_{\rm out}$ is approximately given by (see chapter 2 for details)

$$\frac{\dot{\omega}_{\rm out}}{2\pi} = \frac{3}{4}\frac{1}{P_{\rm out}}\left(\frac{a_{\rm in}}{a_{\rm out}}\right)^2\left(\sqrt{\frac{m_2}{m_1}}+\sqrt{\frac{m_1}{m_2}}\right)^{-2}\frac{1}{(1-e_{\rm out}^2)^2}, \tag{4.1}$$

for a coplanar triple system with $e_{\rm in}^2 \ll 1$. The slope of dashed lines in Figure 4.2 corresponds to the prediction of equation (4.1) evaluating with input values of orbital parameters (see Tables 4.1 and 3.2), which reproduces the behavior of $\langle\omega_{\rm out}\rangle(t)$ very well. This good agreement indicates that the variation of $\omega_{\rm out}$ averaged over $P_{\rm out}^{(0)}$ is well approximated by $\dot{\omega}_{\rm out}t$ with equation (4.1).

Apart from the short-term RV variations, we can likely see the shift of $\omega_{\rm out}$ induced by the inner-binary perturbation with the long-term observations. We divide the long-term RV observational data into multiple segments with one orbital periods. Since the shape of RV curve is sensitive to the argument of pericentre, it is possible to detect the shift of $\omega_{\rm out}$ by evaluating the time evolution of the best-fit $\omega_{\rm out}$ at each segment. We can fit the total RV at each epoch, and search for $\omega_{\rm out}$ variations by comparing with the approximate formula. The timescale is estimated from equation (4.1) as $\sim P_{\rm out}(a_{\rm in}/a_{\rm out})^{-2}$. Thus, we can detect the variations within hundreds of $P_{\rm out}$ in principle.

We can divide long-term RV observational data into multiple segments with one orbital periods. Since the shape of RV curve is sensitive to the argument of pericentre, we can detect the shift of $\omega_{\rm out}$ by evaluating the time evolution of the best-fit $\omega_{\rm out}$ at each segment.

Therefore, the pericenter shift provides an independent signature of the presence of the inner binary. Indeed, this methodology is proposed by Le Verrier (1859) in different context to explain the anomalous perihelion shift of Mercury in Newton's theory before general relativity was discovered by Einstein (1915).

4.3.2 Long-term RV amplitude modulations for non-coplanar orbits

Here, we examine how the non-coplanarity between the inner and outer orbits affects the RV of a tertiary star. Since the general analysis of the non-coplanar case is not

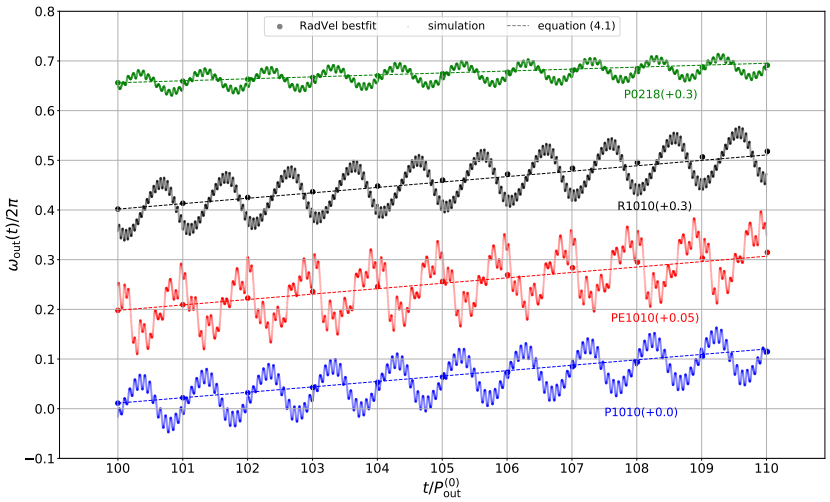

Figure 4.2 Best-fit values of $\omega_{\rm out}(t)$ for P1010, PE1010, R1010 and P0218. Each best-fit value is determined with `RadVel` from simulation data using their 0.1-day cadence outputs over $1P^{(0)}_{\rm out}$ starting at t. The dashed line is calculated using the analytic approximate formula of $\dot{\omega}_{\rm out}$ in equation (4.1). For clarity, the data are translated in y direction with the offset value indicated in parenthesis. Adapted from HS2020.

realistic, we focus on two specific initial configurations that we call inclined ($i_{\rm mut} = 45°$; denoted by I) and orthogonal ($i_{\rm mut} = 90°$; denoted by O) as specified in Table 4.1.

The results are plotted in Figure 4.3, 4.4, 4.5, and 4.6 for I1010, O1010, I0218, and O0218, respectively. Each figure has eight panels; Top-left panels display the trajectory of the direction of the angular momentum vectors of the inner (red) and outer (blue) orbits. The numbers in the plot indicate $t/P^{(0)}_{\rm out}$. Top-right panels show the corresponding evolution of the mutual inclination ($i_{\rm mut}$), orbital inclinations ($I_{\rm in}$ and $I_{\rm out}$), and longitudes of the ascending nodes ($\Omega_{\rm in}$ and $\Omega_{\rm out}$). Top-right panels of Figures 4.3 - 4.6 are updated from HS2020. While the original figures show the orbital evolution every one $P_{\rm out}$, the updated ones show the evolution every one day (see also appendix E). Middle panels plot the residual RV variations after subtracting base-line Kepler motion, and the corresponding LS periodograms viewed from the x and z-axes of the reference frame (Figure 4.1). Bottom panels plot the total RV curves, instead of the residual RV variations, viewed from the x and z-axes.

Consider first I1010 that has the mutual inclination of $i_{\rm mut} = 45°$ initially. As shown in the top panels of Figure 4.3, the inner and outer orbits precess around the total angular momentum axis of the entire system in a fairly periodic and regular fashion. As discussed in chapter 2, this corresponds to the precession of the inner and outer orbits around the total angular momentum axis of the triple system. The period of $\approx 65P^{(0)}_{\rm out}$ is indeed well explained by the approximate formula in equation (2.36). This roughly corresponds to the ZKL oscillation timescale $T_{\rm ZKL}$(Kozai 1962; Lidov 1962; von Zeipel 1910) (see chapter 2).

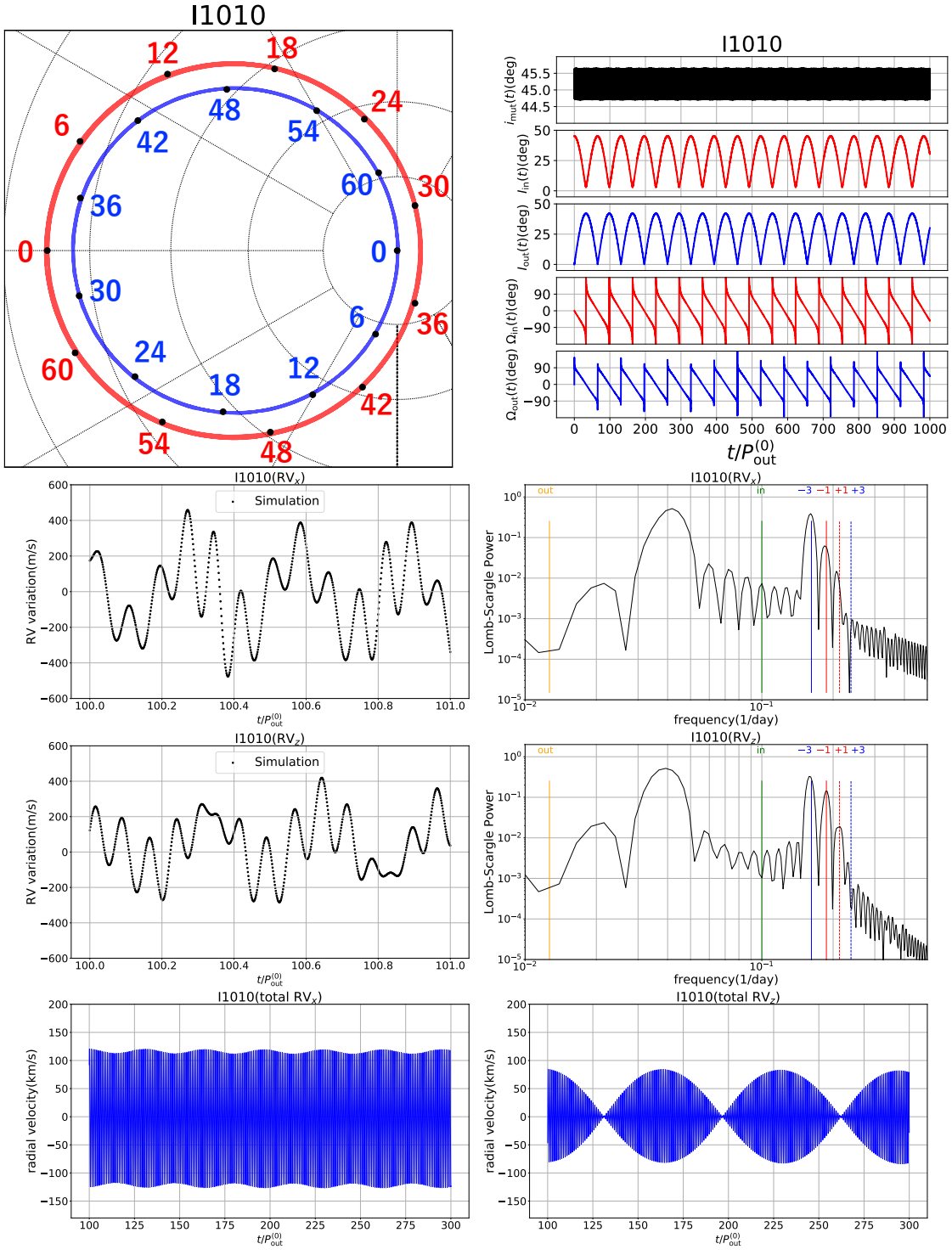

Figure 4.3 Behavior of the non-coplanar triple I1010: *Top:* evolution of orientation of inner and outer orbits (in red and blue, respectively). The longitudinal and latitudinal lines in the left panel are drawn every 30 and 10 degrees, respectively. *Middle:* time series of RV variations along x, z axes, and the corresponding LS periodograms. *Bottom:* total RV curves along x (left) and z (right) axes. Updated from HS2020.

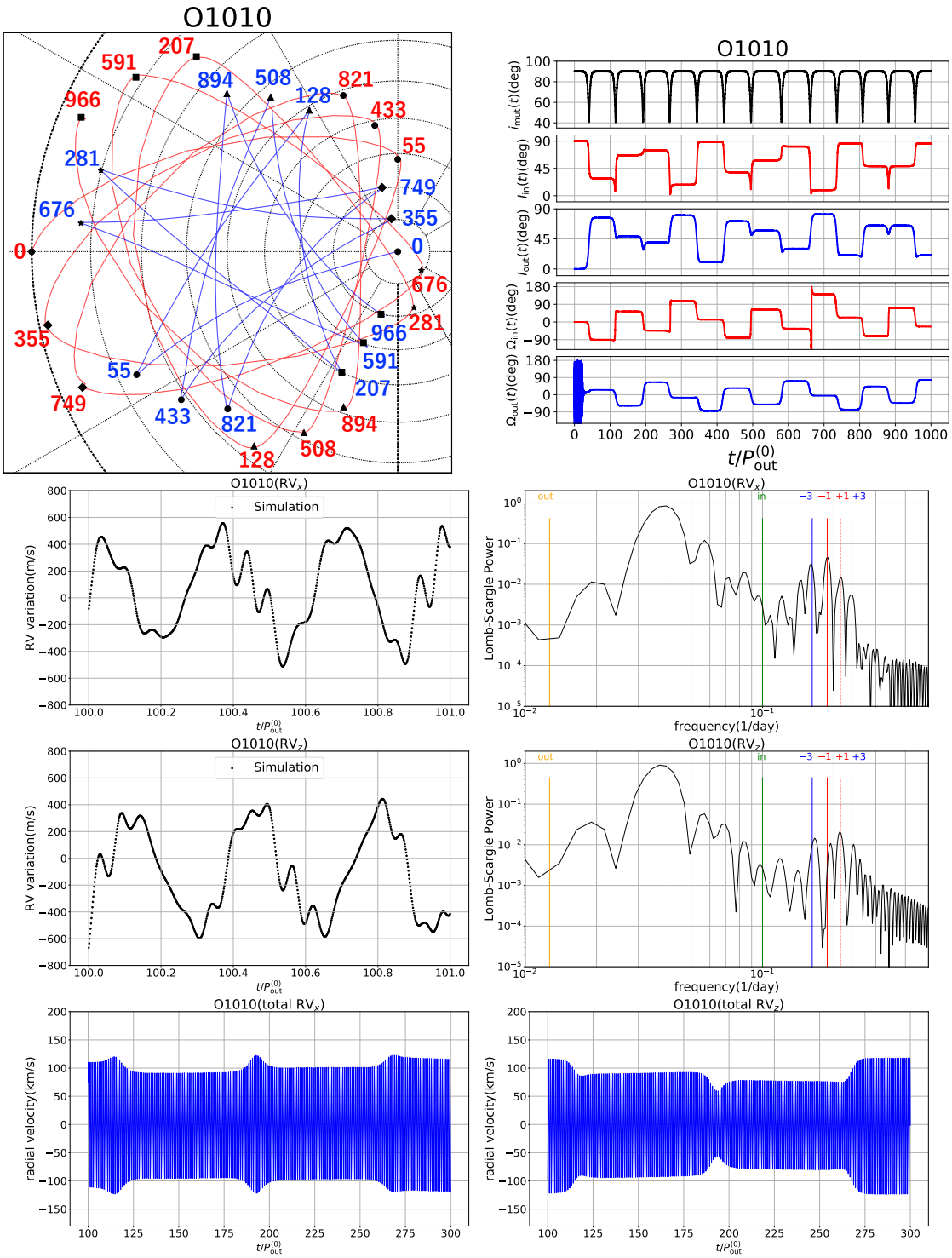

Figure 4.4 Same as Figure 4.3 but for O1010. Updated from HS2020.

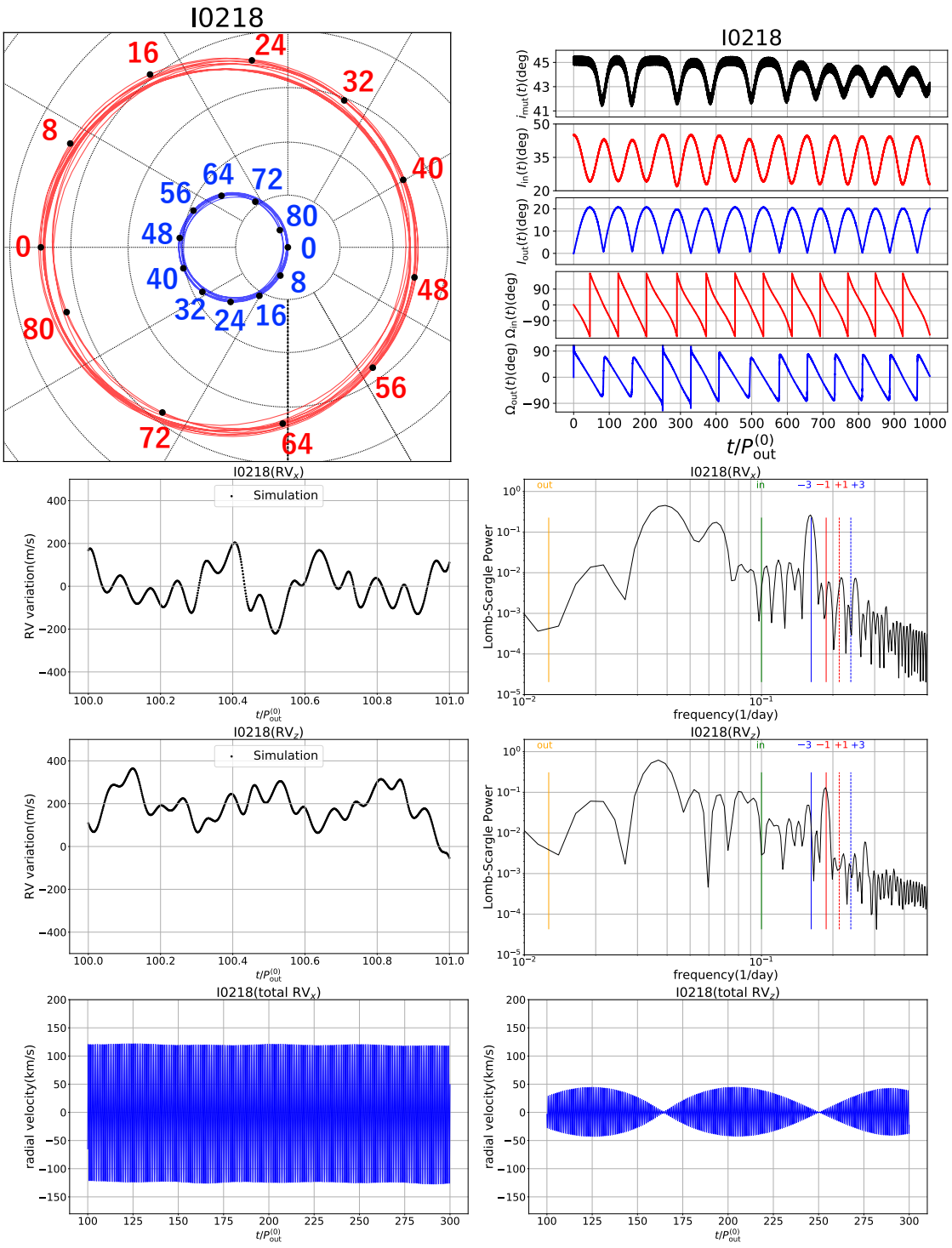

Figure 4.5 Same as Figure 4.3 but for I0218. Updated from HS2020.

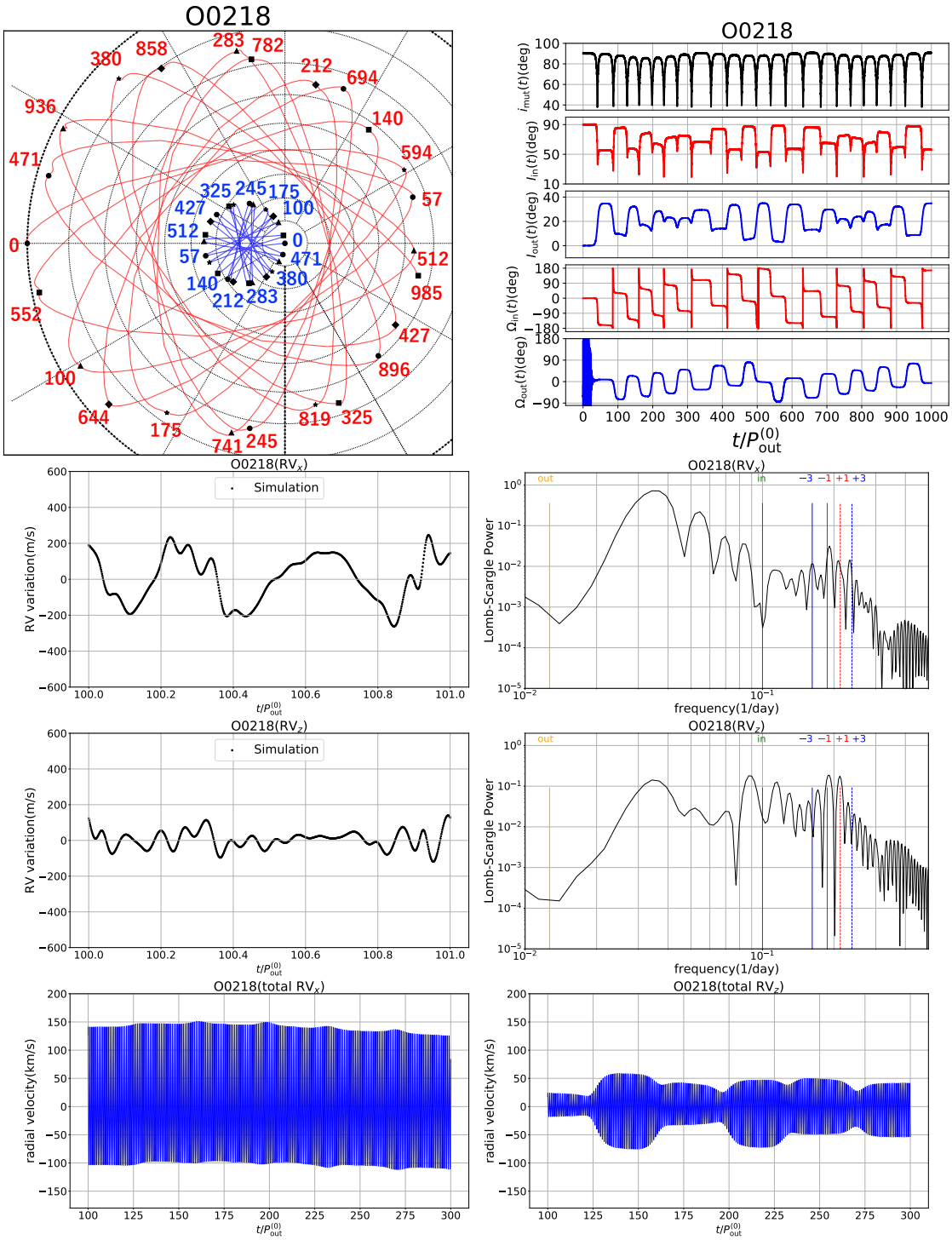

Figure 4.6 Same as Figure 4.3 but for O0218. Updated from HS2020.

Table 4.2. Parameters relevant to precession timescales for fiducial non-coplanar models

case	$i_{\rm mut}$ (deg)	$G_{\rm in}/C_{\rm quad}P_{\rm out}^{(0)}$	$G_{\rm out}/C_{\rm quad}P_{\rm out}^{(0)}$	$G_{\rm tot}/C_{\rm quad}P_{\rm out}^{(0)}$	$P_\Omega/P_{\rm out}^{(0)}$
I1010	45	153.8	175.3	304.2	65.6
O1010	90	153.8	175.3	233.2	$+\infty$
I0218	45	153.8	486.9	605.6	91.6
O0218	90	153.8	486.9	510.7	$+\infty$

We compute the periods for our four non-coplanar models (in which $G_{\rm out} \sim G_{\rm in}$) from equation (2.36), and summarized the values in Table 4.2. Indeed, the periods are in reasonable agreement with the results shown in Figures 4.3 and 4.5 ($i_{\rm mut} = 45°$, moderate inclinations).

In this case, evolution of the mutual inclination is fairly moderate, except for the precession, and the inner and outer orbits remain to be near-prograde each other. Therefore, despite that the additional periodic terms are present in the RV variations, both the time series and the LS periodograms show clear modulations due to the inner binary at frequencies of ν_{-3} and ν_{-1}. Those trends should be generic for moderately inclined systems with $i_{\rm mut} < 45°$.

More importantly, an interesting observable feature appears as the significant modulation of the Keplerian RV component over a timescale of $T_{\rm ZKL}$, induced by the periodic variation of $I_{\rm out}$. The bottom panels of Figure 4.3 show the RV amplitude modulation from nearly edge-on (x-axis) and face-on (z-axis) line-of-sights. Since the time-dependence of the total RV semi-amplitude is approximately given as

$$\begin{aligned} K_{\rm out}(t) &\approx K_0 \sin(I_{\rm out}(t)) \\ &\approx K_0 \sin(I_{\rm out}(t_0)) + K_0 \dot{I}_{\rm out}(t_0) \cos(I_{\rm out}(t_0))(t-t_0) + \mathcal{O}((t-t_0)^2), \end{aligned} \quad (4.2)$$

large variations, possibly reaching the same order of K_0, are expected especially for a nearly face-on (i.e. $I_{\rm out}(t_0) \approx 0°$) case.

If the mutual inclination of the two orbits is much larger, the orbital orientations exhibit substantial dynamical evolution. This is in marked contrast to the case of the initially orthogonal orbits; see the top-left panel of Figure 4.4. The trajectories of the orientations of the inner and outer orbits for O1010 in the top-left panel of Figure 4.4 seem to evolve in an irregular fashion. They first stay at the initial location represented by the filled circles labeled by 0 (blue and red for outer and inner orbits, respectively) until $t \approx 30P_{\rm out}^{(0)}$. Then, they move along the trajectories rapidly and reach the next temporary stationary location at $t = 55P_{\rm out}^{(0)}$ as the top-right panel indicates. Then the orientations of the angular momenta stay the same location until $t \approx 105P_{\rm out}^{(0)}$, and reach the next location at $t = 128P_{\rm out}^{(0)}$. This evolution pattern continues, while

their mutual inclination $i_{\rm mut}$ oscillates between 40° and 90° in a regular and periodic fashion.

In this case, the ZKL oscillation (Kozai 1962; Lidov 1962; von Zeipel 1910) plays an important role in the evolution of inclinations themselves. Since the precession period given by equation (2.36) is inversely proportional to $\cos i_{\rm mut}$, the system stays for a long time at highly inclined states of $i_{\rm mut} \approx \pi/2$. Indeed, Table 4.2 expects the timescale is infinite at the stage. However, the ZKL oscillation enhances the inner eccentricity, and $i_{\rm mut}$ begins to decrease afterwards. The approximate timescale is no longer valid although its timescale is comparable to $T_{\rm ZKL}$. This behavior explains the drastic modulation on the semi-amplitude of RV as shown in the bottom panels of Figure 4.4.

Independently of such complicated behavior of orbital angles, the RV variations of frequencies $\nu_{\pm 3}$ and $\nu_{\pm 1}$ can be used as a signature of inner binaries as indicated by the middle panels of Figure 4.4. This implies that we can use the same strategy to detect an inner binary as well, even for a non-coplanar system. Nevertheless, the bottom panels show that the total RV amplitude modulations will provide a strong probe of inner unseen binary for orthogonal triples as well.

Just for completeness, Figures 4.5 and 4.6 show the results for non-coplanar very unequal-mass cases: I0218 and O0218. The resulting figures support the overall behavior is very similar to equal-mass cases, except for higher-order effects which may come from the octupole disturbing function. Since the angular momentum of the inner binary is smaller than that in equal-mass cases, the total angular momentum is dominated by that of the outer orbit. Therefore, the outer orbital inclination is more stable. The RV variations and LS periodograms confirm again that the basic strategy for detecting an inner binary is valid also for unequal-mass and non-coplanar triple systems.

Even a non-detection of such long-term RV variations induced by the evolution of the outer orbital plane can put constraints on the presence of the inner binary. Since the expected variations are huge, we need not perform the intensive RV monitoring unlike the short-term RV variations. If an outer star has a relatively short orbital period, the longer-term monitoring of the total RV amplitude may easily reveal a possible non-coplanar inner binary. This methodology is indeed successful to put a constraint on the lower limit of mutual inclination for a stellar triple HD109648 from the detection of long-term RV variations; $5.4° \leq i_{\rm mut}$ (prograde case) and $i_{\rm mut} \leq 174.6°$ (retrograde case) (Jha et al. 2000). If an outer star of triples has a relatively short orbital period, the longer-term monitoring of the total RV amplitude may reveal a possible non-coplanar inner binary.

The detection of non-coplanar triples including BBHs is interesting even from a theoretical aspect. Barnes & O'Brien (2002); Liu & Lai (2017, 2018); Thompson (2011) among others have suggested that the ZKL oscillation acting on an inner BBH may significantly accelerate the BBH merging timescale. The detection of non-coplanar triples containing a BBH, thus, would provide very interesting opportunities to understand the formation pathway to the population of BBHs that have been continuously

detected with gravitational wave signals.

4.4 Discussion on the GR and inverse-ZKL effects

In this section, we discuss possible effects of the GR corrections and the inverse ZKL oscillations on our proposed methodology. This is important to guarantee the feasibility of the methodology.

It is known that the GR precession of an inner binary suppresses the ZKL oscillation effectively when its precession rate $\dot{\omega}_{\rm GR}$ exceeds the ZKL precession rate $\dot{\omega}_{\rm K}$. Their ratio is given by

$$\frac{\dot{\omega}_{\rm GR}}{\dot{\omega}_{\rm K}} = \frac{3(1-e_{\rm out}^2)^{3/2}}{\sqrt{1-e_{\rm in}^2}} \left(\frac{v_{\rm in}}{c}\right)^2 \left(\frac{P_{\rm out}}{P_{\rm in}}\right)^2 \frac{m_1+m_2+m_*}{m_*}, \tag{4.3}$$

where $v_{\rm in} \equiv \sqrt{\mathcal{G}(m_1+m_2)/a_{\rm in}}$ corresponds to the orbital velocity of inner binary (e.g. Liu et al. 2015).

The left-panel of Figure 4.7 shows the precession ratio, equation (4.3), against $e_{\rm in}$ for $P_{\rm in} = 1$, 3, 5 and 10 days, where we adopt the fiducial values for the other parameters. The plot indicates that the GR precession effect is safely neglected unless the inner binary is highly eccentric and/or has a very short orbital period. Moreover, we performed simulations for non-coplanar models in Table 4.1 using `REBOUNDx` with GR corrections, and confirmed that the maximum inner eccentricity changes less than 3 % over 1000 $P_{\rm out}^{(0)}$ for both O1010 and O0218. Thus we conclude that our results based on purely Newtonian gravity are not affected by the GR precession. The GR effect, however, might change the evolution of the triple over a much longer timescale, including the the secular stability of the system.

The gravitational wave (GW) emission may also affect the long-term stability of the system. The GW induced merger timescale for an eccentric isolated binary is analytically given by (Peters 1964)

$$\tau_{\rm GW} = \frac{12}{19}\frac{c_0^4}{\beta}\int_0^{e_0} \frac{de\; e^{\frac{29}{19}}\left(1+\frac{121}{304}e^2\right)^{\frac{1181}{2299}}}{(1-e^2)^{3/2}}, \tag{4.4}$$

where

$$c_0 \equiv \frac{(1-e_0^2)}{e_0^{12/19}}\left(\frac{\mathcal{G}(m_1+m_2)P_0^2}{4\pi^2}\right)^{1/3}\left(1+\frac{121}{304}e_0^2\right)^{-\frac{870}{2299}} \tag{4.5}$$

and

$$\beta \equiv \frac{64}{5}\frac{{\rm G}^3 m_1 m_2 (m_1+m_2)}{c^5} \tag{4.6}$$

with P_0 and e_0 being initial orbital period and eccentricity, respectively.

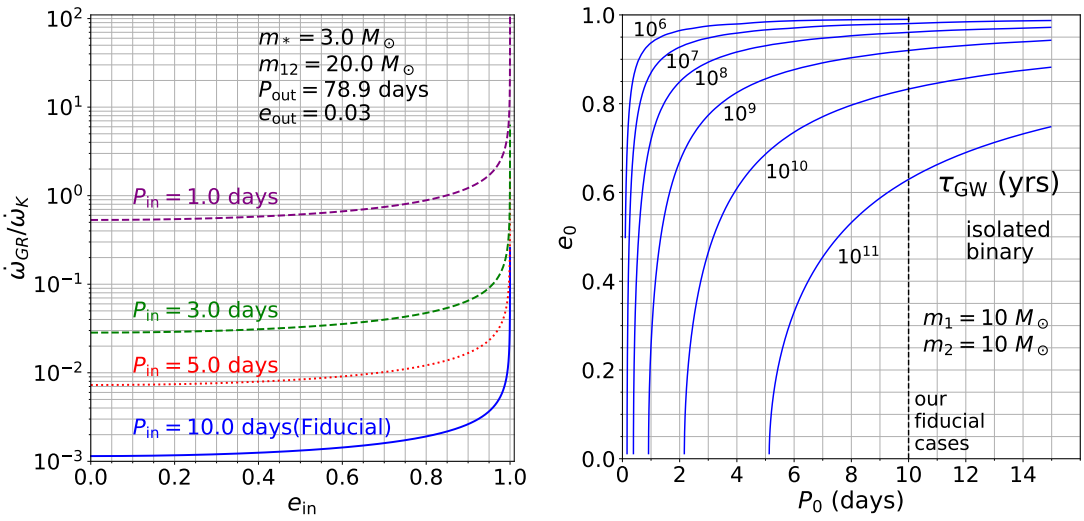

Figure 4.7 Characteristic timescales of the GR corrections: *Left:* the ratio of GR and ZKL precession rates $\dot{\omega}_{\rm GR}/\dot{\omega}_{\rm K}$ of inner pericenter arguments ω against the eccentricity of the inner binary $e_{\rm in}$ for $P_{\rm in} = 1$, 3, 5 and 10 days. *Right:* contour plots of the merger time $\tau_{\rm GW}$ due to the gravitational wave emission on the $P_0 - e_0$ plane for an isolated binary (neglecting the effect of the tertiary star). Adapted from HS2020.

The right-panel of Figure 4.7 plots the contour of $\tau_{\rm GW}$ as a function of the eccentricity and orbital period at the initial epoch, e_0 and P_0. Again, the GW emission is largely negligible unless the binary is highly eccentric and/or has a very short orbital period, which is not the case for our models considered here. This estimate, however, neglects the dynamical effect by the tertiary object on the inner binary, and may vary in a case that the ZKL oscillation excites significantly the eccentricity of the inner binary.

It is also possible that the orbit of the outer star is affected by the inverse-ZKL and other eccentricity-inclination resonances(e.g. de Elía et al. 2019; Naoz et al. 2017, 2020; Vinson & Chiang 2018), which may enhance the outer eccentricity effectively, depending on the initial conditions. For example, Vinson & Chiang (2018) showed that the eccentricity of an outer test particle can be enhanced up to ~ 0.2 and ~ 0.3 by the inverse ZKL resonance and octupole resonance on $\varpi_{\rm out}+\varpi_{\rm in}-2\Omega_{\rm out}$, respectively. They also pointed out that the outer eccentricity enhancement becomes stronger as the inner eccentricity increases, due to the octupole apse-aligned resonance. The outer eccentricity enhancement may lead to the orbital crossing and the system may becomes unstable eventually.

For our fiducial cases, however, the amplitudes of the inner and outer orbital angular momenta are comparable. Thus the test particle approximation for the tertiary star is not valid. In this case, the total angular momentum conservation may prohibit the significant enhancement of the outer eccentricity. Nevertheless, the inverse ZKL effect and other resonances may play an important role in the orbital evolution and

secular stability of triples in certain sets of orbital parameters of the triples. The long-term stability of triples that we consider is important to guarantee the feasibility of our methodologies, and partly discussed in chapter 6.

4.5 Summary

In this chapter, we examined the long-term RV variations induced by the inner-binary perturbations, and proposed a method to search for inner BBHs through these effects. Since the detection of long-term RV variations should not require high-cadence RV monitoring, this method will be complementary to the short-term RV variations proposed in the previous chapter.

We first considered the shift of the outer pericenter argument $\omega_{\rm out}$ for coplanar triples, and found that the time-averaged $\omega_{\rm out}$, which was determined by RV fitting of $\omega_{\rm out}$ at each epoch, reasonably followed the analytic approximate formula of $\dot{\omega}_{\rm out}$. Therefore, we concluded that the pericentre argument shift can be used to detect an inner binary for coplanar triples, independently of the short-term RV variations.

Next, we considered the long-term RV amplitude modulations for non-coplanar triples. We showed that the total RV semi-amplitude varies periodically due to the precession of inner and outer orbital planes over roughly the ZKL oscillation timescale. We found that the amplitude of the modulations depends on the observer's line-of-sight, but reaches the order of 100 km/s in principle. Although the modulation timescale is usually long, we found that it is possible to detect them over decades, if the outer orbital period is relatively short. For instance, we showed that the modulation can be detected within a decade for our fiducial triples.

Incidentally, we note here that Jha et al. (2000) detected the RV semi-amplitude variation for a tight stellar triple HD109648, due to its nodal precession over their 8-yr RV observation. Thus the similar detection for star-BBH triples should be quite feasible. Since the expected amplitude is so huge compared with the short-term RV variations, it is not required to perform very precise RV observations in general. This is another advantage over the short-term RV variations. Therefore, we concluded that the long-term RV variations are very effective especially for non-coplanar triples.

Furthermore, we also discussed the possible effects from GR corrections and inverse-ZKL oscillations briefly since they possibly affect non-coplanar triples, and therefore our method proposed here. We showed that the effects hardly change the results here through the discussion on timescales, while the effects should affect the long-term stability of systems.

Chapter 5

Novel methods to detect inner BBHs III: pulsar arrival time delays

5.1 Introduction

The previous two chapters were dedicated to the radial-velocity method for a tertiary star. In the present chapter, we rather consider a tertiary pulsar, and extend our methodology on the basis of the pulsar timing method. All the results here are based on HS2021.

Although the presence of (tertiary pulsar - BBH) triples is highly uncertain, and the fraction is expected to be smaller even compared with (star - BBH) triples, a tertiary pulsar, if exists, is an ideal probe of inner BBHs. Great precisions of pulsar timing observations should identify inner BBHs clearly. In addition, pulsar timing observations will be possibly applied for more distant triples, compared with RV observations, which are applicable only to near-by stars with typically much less that ~ 1 kpc. Therefore, these two methods are regarded as compliments.

We here consider a tertiary pulsar orbiting around an inner invisible BBH, and show that the short-term variations in the Rømer delay can be indeed used as a clear signature of the inner binary. Furthermore, we consider two general relativistic pulsar arrival time delays, the Shapiro delay and the Einstein delay. We show that the simultaneous detections of these delays improve significantly the determination of the orbit of inner BBH.

First, we introduce an overview of the pulsar arrival time delays in triples. We compare the expected amplitude of each delay, using the analytic approximation formulae for a coplanar and near-circular triple. Then, we show how we can determine the orbital parameters of triples, such as masses and orbital separations, using each delay, in detail.

Next, we show the example time-delay curves of each effect for three orbital configurations using the analytic expressions of time-delay effects.

As one specific application, we put rough constraints on possible inner binary companions of the currently known double neutron-star (DNS) binaries from root

mean squares of the observational time residuals. Although it is unlikely that unseen companions in DNS binaries are indeed invisible inner binaries, the results clearly show how effectively our method can constrain on possible binaries.

Finally, we discuss the possible synergy between this method and future direct observation of low-frequency GWs with space-based GW detectors including LISA, DECIGO, and BBO.

5.2 A method using the pulsar timing analysis

5.2.1 Triple configuration

As described in Figure 4.1 in the previous chapter, we consider a hierarchical triple system consisting of an inner binary and a tertiary. The inner binary comprises of two compact objects of masses m_1 and m_2, and is orbited by a tertiary pulsar of mass m_3 in this chapter.

In terms of the Jacobi coordinates, the inner and outer orbits are specified by the semi-major axis a_j, the eccentricity e_j, and the argument of pericenter ω_j, where the index $j = \{\mathrm{in}, \mathrm{out}\}$ refers to the inner and outer orbits, respectively. The orientation of each orbit is specified by two angles relative to the reference frame; the inclination I_j (the angle between the normal vector of the orbit and z-axis) and the longitude of ascending node Ω_j measured from x-axis.

The mutual inclination between the inner and outer orbits is denoted by i_{mut}, and the orbital period and the corresponding mean motion for each orbit are defined as P_j and $\nu_j (= 2\pi/P_j)$. Since we consider a hierarchical triple system, we assume that $P_{\mathrm{in}} \ll P_{\mathrm{out}}$. For definiteness, we assume that the distant observer is located in the negative z-axis in Figure 4.1

For demonstration, we assume a fiducial set of parameters, $P_{\mathrm{in}} = 10$ days, $P_{\mathrm{out}} = 100$ days, and $m_1 = m_2 = 10\ M_\odot$, which will be used in evaluating characteristic amplitudes of the time delays.

5.2.2 Pulsar arrival time delays

The architecture of the triple system is encoded in the motion of the tertiary object orbiting the unseen inner binary. If the tertiary is a visible star, its radial velocity carries the key information.

On the other hand, if a tertiary is a pulsar, its arrival time variation has almost identical information of its radial velocity, but with much higher precision. Furthermore, general relativistic effects provide additional and complementary information on the parameters of the triple system.

The arrival time of the pulsar is modulated due to the periodic change of the position of the pulsar. For a pulsar binary system, there are three well-known effects including the Rømer delay $\Delta_{\mathrm{R}}(t)$, the Einstein delay $\Delta_{\mathrm{E}}(t)$, and the Shapiro delay $\Delta_{\mathrm{S}}(t)$. In the case of the hierarchical triple system, the main contribution to those

three terms comes from the approximate binary motion of the pulsar relative to the barycenter of the inner binary of mass $m_{12} \equiv m_1 + m_2$, whose explicit expressions(e.g Backer & Hellings 1986; Edwards et al. 2006) are given in this subsection. More importantly, the inner binary produces an additional modulation of a period of approximately $P_{\rm in}/2$ in the motion of tertiary. Consequently, the Rømer delay is given by $\Delta_{\rm R,Kep}(t)$ and $\Delta_{\rm R,BBH}(t)$ that can be distinguished from their different frequencies. Indeed the inner binary information is imprinted in $\Delta_{\rm R,BBH}(t)$ as we will see below.

The Rømer delay due to the Keplerian motion of the tertiary pulsar

The Rømer delay is caused by the change of the distance of the pulsar relative to the observer. To the lowest order, the pulsar moves along a Keplerian orbit around the barycenter of the triple system. The corresponding Rømer delay is written in terms of the eccentric anomaly of the outer orbit, $E_{\rm out} = E_{\rm out}(t)$, as

$$\Delta_{\rm R,Kep}(t) = x[\sin\omega_{\rm out}(\cos E_{\rm out} - e_{\rm out}) + \sqrt{1-e_{\rm out}^2}\cos\omega_{\rm out}\sin E_{\rm out}] \tag{5.1}$$

The eccentric anomaly is expressed implicitly as function of time through Kepler's equation:

$$2\pi t = P_{\rm out}(E_{\rm out} - e_{\rm out}\sin E_{\rm out}). \tag{5.2}$$

Note that we can only observe the difference of the time delay, and can choose arbitrarily the zero point of the overall time delays.

Since the semi-major axis of the outer orbit, $a_{\rm out}$, is defined with respect to the center of mass of the inner binary, that of the pulsar orbit with respect to the barycenter of the triple is given by $a_{\rm p} = (m_{12}/m_{123})a_{\rm out}$, where $m_{12} \equiv m_1 + m_2$ and $m_{123} \equiv m_1 + m_2 + m_3$. Thus the amplitude of the Rømer delay for a distant observer at the negative z-direction (Fig.4.1) reduces to

$$x \equiv \frac{m_{12}}{m_{123}}\frac{a_{\rm out}\sin I_{\rm out}}{c} \approx 570\ {\rm sec}\left(\frac{m_{12}}{m_{123}}\right)\left(\frac{m_{123}}{20\ M_\odot}\right)^{1/3}\left(\frac{P_{\rm out}}{100\ {\rm days}}\right)^{2/3}\sin I_{\rm out}. \tag{5.3}$$

The Einstein delay and the Shapiro delay

In addition to the Rømer delay, there are two important general relativistic effects that carries the information of the triple system; the Einstein delay and the Shapiro delay.

The Einstein delay is caused by the difference between the proper time of the pulse emission and the coordinate time of the barycenter of the binary under the gravitational field, and is explicitly expressed as

$$\Delta_{\rm E}(t) = \gamma_{\rm E}\sin E_{\rm out}, \tag{5.4}$$

where the amplitude is given by

$$\gamma_{\rm E} \equiv \left(\frac{\mathcal{G}}{c^3}\right)^{\frac{2}{3}}\left(\frac{P_{\rm out}}{2\pi}\right)^{\frac{1}{3}} e_{\rm out}\frac{m_{12}(m_3+2m_{12})}{m_{123}^{4/3}}$$

$$\approx 2.4 \text{ msec} \left(\frac{P_{\rm out}}{100 \text{ days}}\right)^{\frac{1}{3}} \left(\frac{m_{12}}{20\ M_\odot}\right) \left(\frac{m_{123}}{20\ M_\odot}\right)^{-\frac{1}{3}} \left(1+\frac{m_{12}}{m_{123}}\right) \left(\frac{e_{\rm out}}{0.01}\right) \quad (5.5)$$

with $\mathcal{G}$ being the gravitational constant.

The Shapiro delay is the time delay during the passage of the photon in the gravitational field of the companion, and is given by

$$\begin{aligned} \Delta_{\rm S}(t) &= -2r \ln [1 - e_{\rm out} \cos E_{\rm out} \\ &\quad -s \left(\sin \omega_{\rm out} (\cos E_{\rm out} - e_{\rm out}) + \sqrt{1-e_{\rm out}^2} \cos \omega_{\rm out} \sin E_{\rm out} \right)], \end{aligned} \quad (5.6)$$

where r and s are the major observables and usually referred to as "range" and "shape" parameters(e.g Backer & Hellings 1986; Edwards et al. 2006):

$$r \equiv \frac{\mathcal{G} m_{12}}{c^3} \approx 98\ \mu\text{sec} \left(\frac{m_{12}}{20\ M_\odot}\right), \quad (5.7)$$

$$s \equiv \sin I_{\rm out}. \quad (5.8)$$

As equations (5.4) and (5.6) indicate, $\Delta_{\rm S} \ll \Delta_{\rm E}$ except for for a nearly circular and edge-on system ($e_{\rm out} \approx 0$ and $s \approx 1$). A notable example is a binary pulsar system PSR J1614-2230 with $e_{\rm out} = 1.30 \times 10^{-6}$ and $I_{\rm out} = 89.17$ deg, which reveals the mass of the pulsar is as massive as 1.97 $M_\odot$ via the analysis of the Shapiro delay (Demorest et al. 2010).

In principle, the Shapiro delays for both inner and outer orbits may be separately detected, especially for nearly edge-on coplanar systems ($I_{\rm out} \approx I_{\rm in} \approx \pi/2$). In this case, the Shapiro delays alone directly reveal the existence of the inner binary and their individual masses m_1 and m_2. In what follows, however, we conservatively consider only the Shapiro delay for the outer orbit, assuming the inner binary as a single object of mass m_{12}.

The Rømer delay due to the inner binary motion

The orbital motion of the inner BBH perturbs the Keplerian motion of the tertiary. The previous two chapters proposed to detect the induced radial velocity modulation of the tertiary star to search for a possible inner BBH in the triple systems. In the case of a coplanar and near-circular hierarchical triple, the corresponding radial velocity variation up to the quadrupole order of the BBH potential is approximately given by equation (3.1).

Thus, integrating the formula over time and translating it into the time delay, we can obtain the short-term Rømer delay as follows.

$$\begin{aligned} \Delta_{\rm R,BBH}(t) \equiv \frac{z_{\rm BBH}(t)}{c} &= \frac{15}{16} \frac{K_{\rm BBH} P_{\rm in}}{4\pi c} \left(\frac{2\nu_{\rm in}}{\nu_{-3}}\right) \sin I_{\rm out} \sin(\nu_{-3} t + \theta_{0,-3}) \\ &+ \frac{3}{16} \frac{K_{\rm BBH} P_{\rm in}}{4\pi c} \left(\frac{2\nu_{\rm in}}{\nu_{-1}}\right) \sin I_{\rm out} \sin(\nu_{-1} t + \theta_{0,-1}), \end{aligned} \quad (5.9)$$

where

$$\nu_{-3} \equiv 2\nu_{\rm in} - 3\nu_{\rm out} \tag{5.10}$$
$$\nu_{-1} \equiv 2\nu_{\rm in} - \nu_{\rm out} \tag{5.11}$$

and

$$K_{\rm BBH} \equiv \frac{m_1 m_2}{m_{12}^2}\sqrt{\frac{m_{123}}{m_{12}}}\left(\frac{a_{\rm in}}{a_{\rm out}}\right)^{7/2}\left(\frac{m_{12}}{m_{123}}a_{\rm out}\nu_{\rm out}\right). \tag{5.12}$$

In the above equations, $\theta_{0,-3}$ and $\theta_{0,-1}$ denote the initial phases.

The characteristic amplitude of the time delay equation (5.9) is

$$\begin{aligned}\frac{K_{\rm BBH}P_{\rm in}}{4\pi c}\sin I_{\rm out} &= \frac{1}{2}\frac{m_1 m_2}{m_{12}^2}\left(\frac{m_{12}}{m_{123}}\right)^{2/3}\left(\frac{P_{\rm in}}{P_{\rm out}}\right)^{7/3} x \\ &\approx 23\ {\rm msec}\left(\frac{K_{\rm BBH}}{100\ {\rm m/s}}\right)\left(\frac{P_{\rm in}}{10\ {\rm days}}\right)\sin I_{\rm out},\end{aligned} \tag{5.13}$$

implying that the inner BBH motion is much larger than the general relativistic terms in general. Furthermore, the high-cadence monitoring of the pulsar timing can break the degeneracy between the ν_{-3} and ν_{-1} modes more easily than in the radial velocity measurements of main-sequence stars.

Figure 5.1 show the contour plots of the characteristic amplitude of the Rømer delay induced by the inner BBH, equation (5.13), for the case of a coplanar and near-circular triple with our fiducial set of parameters. The top panel is plotted on the m_2/m_1 and $P_{\rm in}$ plane for $P_{\rm out} = 100$ days, while the bottom panel is plotted on the $P_{\rm out}$ and $P_{\rm in}$ plane for $m_1 = m_2 = 10\ M_\odot$. Since typical amplitudes of the pulsar timing noise is less than $\mathcal{O}(100)$ μsec (see, e.g., Table 5.2), the Rømer delay induced by the inner BBH for our fiducial triple may be easily detected as long as precise and high-cadence pulsar-timing data are available.

Figure 5.2 compares the characteristic amplitudes of the four time delays as a function of the mass m_{12} and the outer orbital period $P_{\rm out}$ for an equal-mass inner binary with the tertiary mass of $m_3 = 1.4\ M_\odot$. The upper-left, upper-right, lower-left, and lower-right panels show the Rømer delay of the outer Keplerian motion, the Einstein delay, the Shapiro delay, and the Rømer delay induced by the inner binary perturbation, respectively. The solid and dotted black lines in the lower-right panel show the contour curves for the cases that $P_{\rm in} = P_{\rm out}/10$, $P_{\rm out}/50$, respectively. Note that the amplitude of the Shapiro delay is very sensitive to the shape parameter $s = \sin I_{\rm out}$ as indicated by equation (5.6). Therefore, the amplitude of the range parameter r plotted in Figure 5.2 should be regarded as a very rough estimate of the expected Shapiro delay.

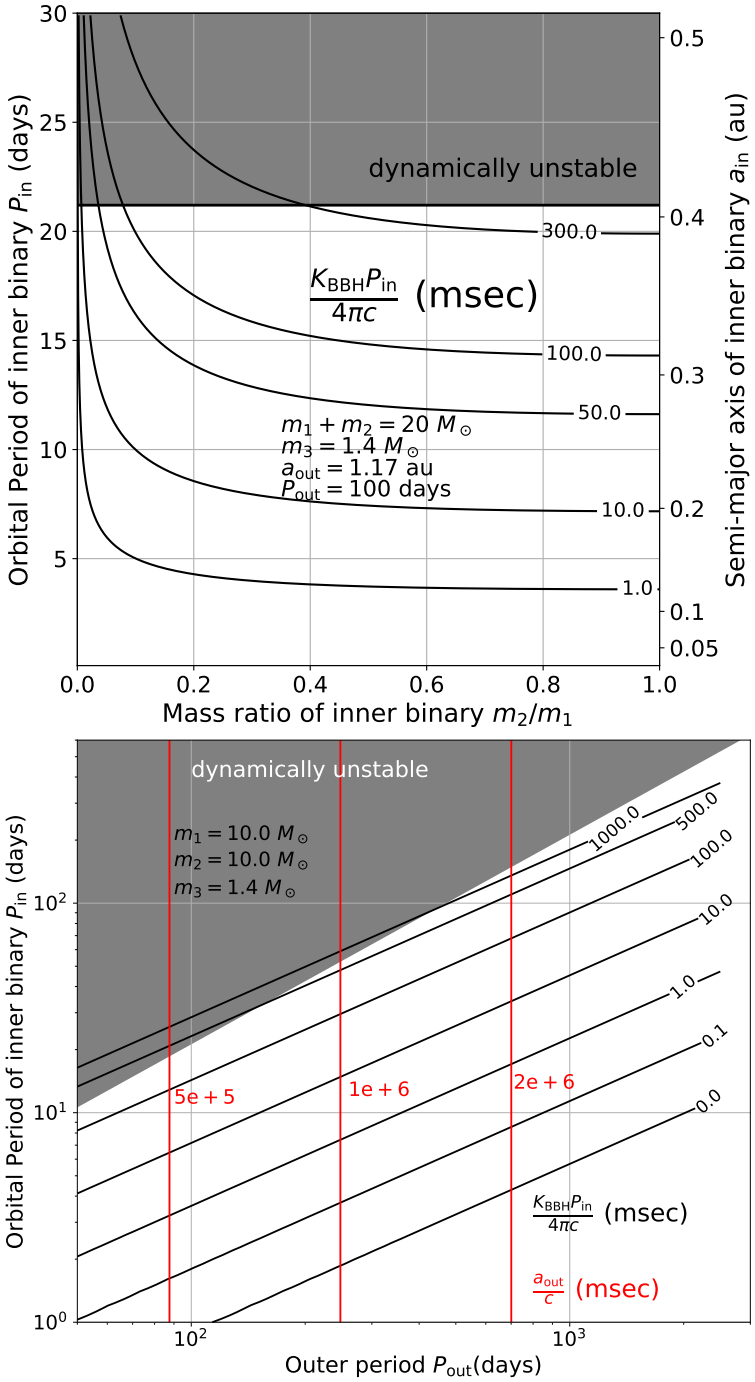

Figure 5.1 Top: characteristic amplitude of the Rømer delay induced by the inner BBH as a function of the inner-binary orbital period ($P_{\rm in}$) and mass ratio (m_2/m_1). The outer orbital period $P_{\rm out}$ is fixed at 100 days (corresponding to $a_{\rm out} = 1.17$ au) in this plot. Bottom: Characteristic amplitude of the Rømer delay induced by the equal-mass inner-BBH as a function of the inner and outer orbital periods. The mass ratio m_2/m_1 is fixed at unity in this plot. In both plots, we assume a coplanar and circular triple system with the following parameters; the total mass of the inner BBH $m_1 + m_2 = 20\ M_\odot$, the tertiary pulsar mass $m_3 = 1.4\ M_\odot$. The upper shaded region is dynamically unstable from the criterion by Mardling & Aarseth (1999). Adapted from HS2021.

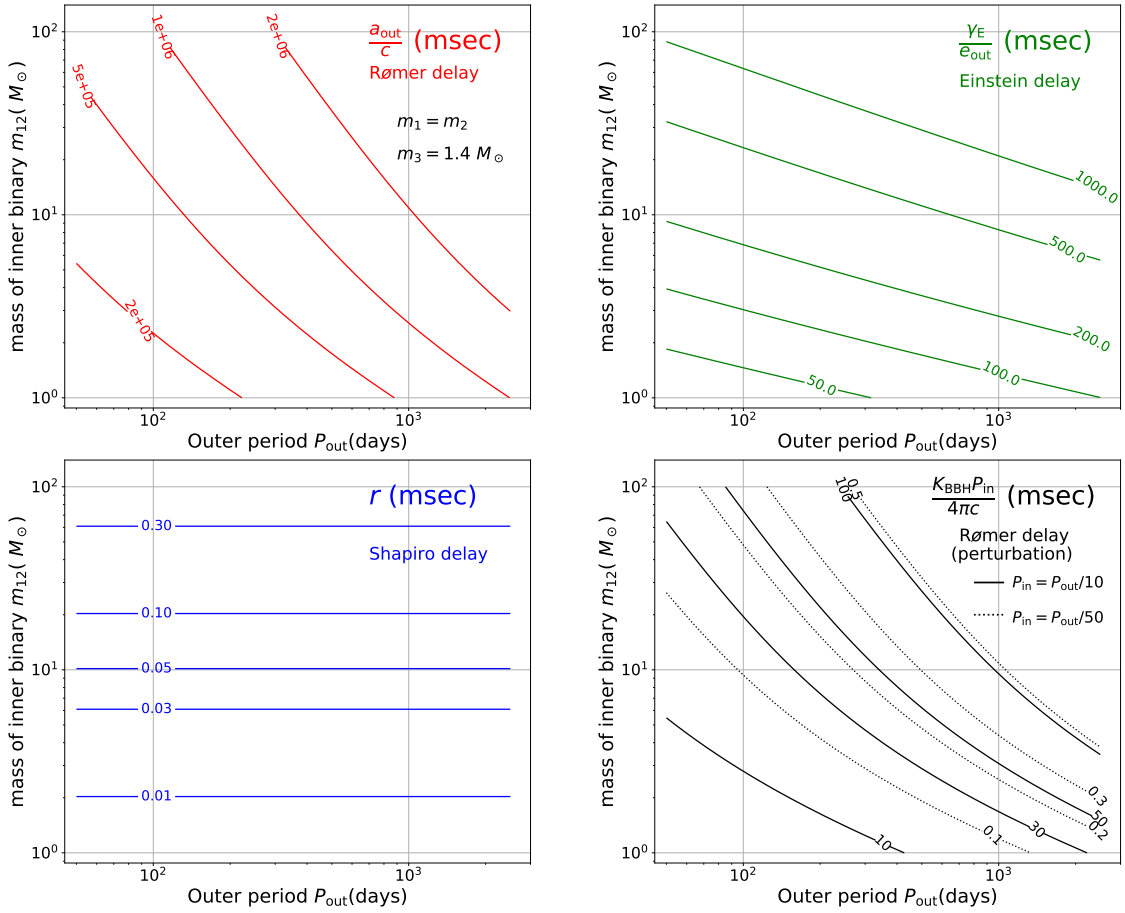

Figure 5.2 Characteristic amplitudes of each time-delay effect as a function of the outer orbital period $P_{\rm out}$ and total mass of the inner BBH m_{12}. The upper-left, upper-right, lower-left, and lower-right panels plot the Rømer delay of the Keplerian motion, the Einstein delay, the Shapiro delay, and the Rømer delay by the inner binary perturbation, respectively. The solid and dotted black lines in the lower-right panel show the Rømer time delay induced by the inner binary with $P_{\rm in}$ being $P_{\rm out}/10$ and $P_{\rm out}/50$, respectively. Note that the amplitude of the Shapiro delay is sensitive to the inclination $I_{\rm out}$, or equivalently to the shape parameter $s = \sin I_{\rm out}$ (see Figure 5.4, for example). Thus, the range parameter r is just a very crude estimate of the amplitude. Adapted from HS2021.

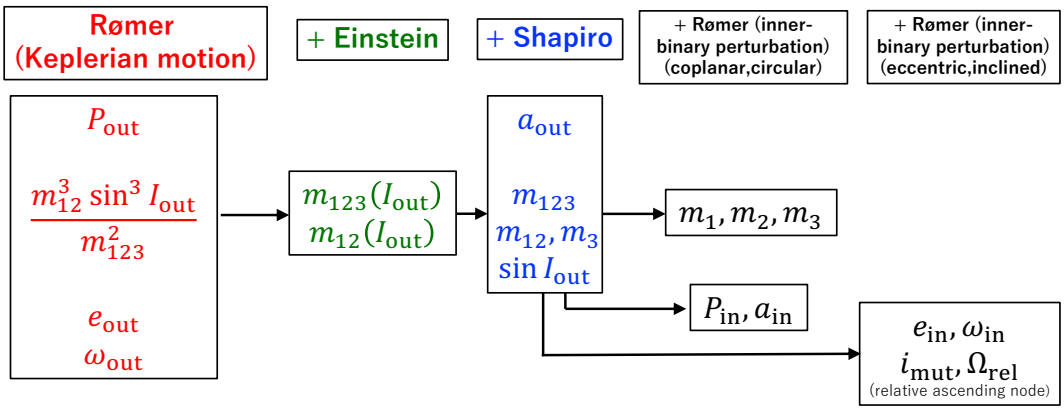

Figure 5.3 Summary of orbital parameters that are estimated from the pulsar arrival timing analysis.Adapted from HS2021.

5.3 Estimations and constraints on parameters from the detection of time delays

In this section, we discuss how the detections of each time delay contribute the estimations and constraints on the parameters of the system. We first consider constraints on the parameters of systems from individual detections of time delays. Next, we consider how their combination determines the properties of the inner BBH.

5.3.1 Constraints on parameters from individual time delay data

There are 13 parameters (three masses and ten orbital parameters except for the initial positions of the bodies) in total that specify the triple system, and the four time delays discussed in the above subsection put different constraints on these parameters. We show these constraints separately for each time delay measurement in this subsection. The procedure to estimate orbital parameters for the triple system with a tertiary pulsar is summarized in Figure 5.3

Consider first the Rømer time delay of the Keplerian motion. Strictly speaking, all orbital parameters in equation (5.1) are not constant except for the two-body system. For the hierarchical triple system that we consider here, those parameters typically vary over the ZKL timescale:

$$\tau_{\rm ZKL} \equiv \frac{m_{12}}{m_3}\frac{P_{\rm out}}{P_{\rm in}}P_{\rm out}. \tag{5.14}$$

Throughout this chapter, we assume that the duration of the pulsar arrival time data is much less than $\tau_{\rm ZKL}$, and that the orbital parameters are approximately constant. Even if it is not the case, however, the method that we propose here remains the same,

but it requires numerical integration of the three-body dynamics so as to properly account for the time-dependence of the orbital parameters.

Under the approximation, fitting equation (5.1) to the series of the pulsar arrival time data determines the values of $e_{\rm out}$, $\omega_{\rm out}$, and $P_{\rm out}$, in addition to the overall amplitude $x = m_{12}a_{\rm out}\sin I_{\rm out}/(cm_{123})$. Combining Kepler's third law $a_{\rm out}^3/P_{\rm out}^2 = (\mathcal{G}m_{123}/4\pi^2)$, one obtains the following relation:

$$\frac{m_{12}^3 \sin^3 I_{\rm out}}{(m_{12}+m_3)^2} = (cx)^3\mathcal{G}^{-1}\left(\frac{2\pi}{P_{\rm out}}\right)^2. \tag{5.15}$$

Indeed, this is the binary mass function expressed in the observables from the Rømer delay measurement.

Second, the Einstein delay, equation (5.4), yields $e_{\rm out}$ and $P_{\rm out}$ through equation (5.2), and $\gamma_{\rm E}$. From the three parameters, one obtains

$$\frac{m_{12}(m_{123}+m_{12})}{m_{123}^{4/3}} = \frac{\gamma_{\rm E}}{e_{\rm out}}\left(\frac{2\pi}{P_{\rm out}}\right)^{1/3}\left(\frac{\mathcal{G}}{c^3}\right)^{-2/3}. \tag{5.16}$$

Equation (5.16) is another useful constraint on m_{123} and m_{12} that is independent of $I_{\rm out}$ unlike equation (5.15) from the Rømer delay.

Third, the Shapiro delay, equation (5.6), is particularly useful to determine $I_{\rm out}(=\sin^{-1}s)$, in addition to $e_{\rm out}$, $P_{\rm out}$, and r. Also the range parameter r, equation (5.7), is directly related to the total mass of the inner BBH binary:

$$m_{12} = r\left(\frac{\mathcal{G}}{c^3}\right)^{-1}. \tag{5.17}$$

Thus, the detection of the Shapiro delay plays a crucial and complementary role in breaking the degeneracy of the parameter estimation, especially for systems with $\sin I_{\rm out} \approx 1$. We also emphasize that the individual detection of the Shapiro delays for both components of the inner orbit would clearly break the degeneracy of the triple architecture of the system. This is likely to be the case if the triple is a nearly coplanar and edge-on system, and one can separately estimate the mass of the inner binary m_1 and m_2 from the Shapiro delays alone.

So far the above observables are mainly for the outer orbital parameters, and the Rømer delay by inner binary motion is the key observable to unveil the properties of the inner BBH. In order to show an specific example, we consider a coplanar near-circular triple expressed in equation (5.9). Fitting equation (5.9) to the pulsar arrival timing data yields

$$P_{\rm in} = \frac{8\pi}{3\nu_{-1}-\nu_{-3}} \tag{5.18}$$

and

$$\frac{m_1m_2}{m_{12}^2}\left(\frac{a_{\rm in}}{a_{\rm out}}\right)^{7/2}\sqrt{\frac{m_{123}}{m_{12}}} = \frac{K_{\rm BBH}}{cx}\left(\frac{P_{\rm out}}{2\pi}\right). \tag{5.19}$$

5.3.2 Inner-binary parameters from joint analysis of time delays

In this section, we show how the orbital parameters of an unseen inner BBH can be recovered from the joint analysis of the pulsar arrival time.

As discussed in the previous subsection, the dominant contribution comes from the Rømer delay from the Keplerian motion of the outer orbit, which derives $e_{\rm out}$, $P_{\rm out}$, $\omega_{\rm out}$, and x. If the Einstein delay is detected as well, the total mass of the system m_{123} and inner binary mass m_{12} are written in terms of the observables and $\sin I_{\rm out}$ from combining equations (5.15) and (5.16):

$$m_{123} = \left(\frac{\mathcal{G}}{c^3}\right)^{-1} \frac{1}{x^3}\left(\frac{P_{\rm out}}{2\pi}\right)\left[\frac{\gamma_{\rm E}}{e_{\rm out}} - \frac{x^2}{\sin^2 I_{\rm out}}\left(\frac{P_{\rm out}}{2\pi}\right)^{-1}\right]^3 \tag{5.20}$$

and

$$m_{12} = \left(\frac{\mathcal{G}}{c^3}\right)^{-1} \frac{1}{x\sin I_{\rm out}}\left[\frac{\gamma_{\rm E}}{e_{\rm out}} - \frac{x^2}{\sin^2 I_{\rm out}}\left(\frac{P_{\rm out}}{2\pi}\right)^{-1}\right]^2 . \tag{5.21}$$

In addition, if the Shapiro delay is detected, $\sin I_{\rm out}$ and m_{12} are derived directly from the range and shape parameters r and s, respectively. Thus equation (5.21) provides a consistency relation among observables:

$$r = \frac{1}{sx}\left[\frac{\gamma_{\rm E}}{e_{\rm out}} - \frac{x^2}{s^2}\left(\frac{P_{\rm out}}{2\pi}\right)^{-1}\right]^2 . \tag{5.22}$$

Using equation (5.22), equation (5.20) is rewritten in terms of the observables alone:

$$m_{123} = \left(\frac{\mathcal{G}}{c^3}\right)^{-1}\left(\frac{sr}{x}\right)^{3/2}\left(\frac{P_{\rm out}}{2\pi}\right). \tag{5.23}$$

Therefore, the mass of the tertiary can be estimated as

$$m_3 = m_{123} - m_{12} = \left(\frac{\mathcal{G}}{c^3}\right)^{-1}\left[\left(\frac{sr}{x}\right)^{3/2}\left(\frac{P_{\rm out}}{2\pi}\right) - r\right]. \tag{5.24}$$

Since the mass of a neutron star is $(1-2)\,M_\odot$, equation (5.24) may be also used as a consistency check of the analysis. Similarly the semi-major axis of the outer orbit can be written as

$$a_{\rm out} = c\left(\frac{P_{\rm out}}{2\pi}\right)\left(\frac{sr}{x}\right)^{1/2} . \tag{5.25}$$

Finally, the Rømer delay by the inner binary perturbation, if observed at all, elucidates the inner orbital parameters from the inner orbital period $P_{\rm in}$, and the velocity variation amplitude $K_{\rm BBH}$; see equation (5.9).

Each mass of inner binary components $m_{1,2}$ and the inner orbital semi-major axis $a_{\rm in}$ are specifically written as follows:

$$a_{\rm in} = cr^{1/3}\left(\frac{P_{\rm in}}{2\pi}\right)^{2/3} \tag{5.26}$$

and

$$m_{1,2} = \left(\frac{\mathcal{G}}{c^3}\right)^{-1}\left(\frac{r}{2}\right)\left[1 \pm \sqrt{1 - \frac{4K_{\rm BBH}}{c}\left(\frac{2\pi r}{P_{\rm in}}\right)^{7/3}\left(\frac{P_{\rm out}}{2\pi}\right)^{4}(rx)^{-2}}\right]. \tag{5.27}$$

Note that the above equations are written in terms of the observables from the Rømer delays of the Keplerian motion and inner binary perturbation, and the Shapiro delay, but without the Einstein delay measurement.

5.4 Effects of the eccentricity and inclination of the inner binary on the pulsar arrival time

While the analytic discussion presented in the previous section assumes a coplanar near-circular triple, the procedure of the triple parameter extraction is the same except that the evolution of the triple system needs to be computed numerically in general. We demonstrate the eccentricity and inclination effects on the pulsar arrival time separately in this section using the approximate analytic formulae by Morais & Correia (2011).

For that purpose, we consider three models listed in Table 5.1; a coplanar circular triple (model CC), a coplanar eccentric triple (model CE), and an inclined circular triple (model IC).

Figure 5.4 plots the time-delay curves for the three models. The upper-left, upper-right, and lower-left panels show the Rømer, Einstein, and Shapiro delays, respectively, due to the outer Keplerian motion of a tertiary pulsar of period $P_{\rm out}$. Strictly speaking, the outer orbit is perturbed by the inner-binary motion as well, but we neglect such small perturbations in those three panels for simplicity. Therefore these three time-delays are computed from equations (5.1), (5.4), and (5.6). The perturbed outer Keplerian motion has been extensively discussed in the previous two chapters.

Thus the unseen inner-binary parameters are encoded only in the Rømer delay modulation plotted in the lower-right panel of Figure 5.4, which is computed from equation (5.9) for model CC, and the analytic perturbative formulae derived in Morais & Correia (2011) for models CE and IC.

The upper-left panel of Figure 5.4 indicates that the outer eccentricity $e_{\rm out}$ distorts the sinusoidal curve of the Rømer delay to some extent, according to equation (5.1). Note that the constant offset in the figure is not relevant, and the eccentricity changes the shape of the delay. On the other hand, the Einstein delay (upper-right panel) is very sensitive to $e_{\rm out}$ since equation (5.4) is proportional to $e_{\rm out}$.

Table 5.1. Models of non-circular/non-coplanar triples

	$e_{\rm in}$	$e_{\rm out}$	$i_{\rm mut}$ (deg)
CC (coplanar circular)	0.0	0.01	0.0
CE (coplanar eccentric)	0.2	0.3	0.0
IC (inclined circular)	0.0	0.01	45

Note. — We adopt the same values for the other triple parameters: $m_1 = m_2 = 10\ M_\odot$, $m_3 = 1.4\ M_\odot$. $P_{\rm in} = 10$ days, $P_{\rm out} = 100$ days. The angles are $\omega_{\rm in} = 30$ deg, $\omega_{\rm out} = 60$ deg, $\Omega_{\rm in} = \Omega_{\rm out} = 0$ deg, and the initial true anomalies $f_{\rm in} = 120$ deg and $f_{\rm out} = 0$ deg.

Since the Shapiro delay is especially sensitive to the inclination of the outer orbit relative to the observer, the lower-left panel plots three different cases for $I_{\rm out}$; nearly edge-on (85 deg), moderately inclined (60 deg), and nearly face-on (30 deg) for each model. While the amplitude of the Shapiro delay is smaller than the Rømer delay and the Einstein delay for an eccentric orbit, it provides a unique constraint on $I_{\rm out}$, especially for an inclined outer orbit, that is useful to break the parameter degeneracy as emphasized in the previous section.

Finally the lower-right panel, the Rømer delay due to the inner-binary perturbation, exhibits a clear shorter-term modulation (of period $\approx P_{\rm in}/2$) periodicity, whose shape is also sensitive to the inner eccentricity and inclination. Therefore, the detection of such short-term periodic features in the time delay component is a promising probe of the possible inner BBH of the unseen companion of the pulsar.

5.5 Application of our method : a proof of concept to constrain an unseen inner binary

Our method proposed in this chapter requires target pulsar binary systems with an unseen massive companion. The detection of the Rømer delay modulation much shorter than the pulsar's Keplerian orbital period is an unambiguous proof that the unseen companion is indeed a binary, instead of a single object. While no interesting candidate is known for which our method can be applied, we attempt to put constraints on a possible inner binary for a companion of existing double neutron star (DNS) binaries through available pulsar arrival timing data.

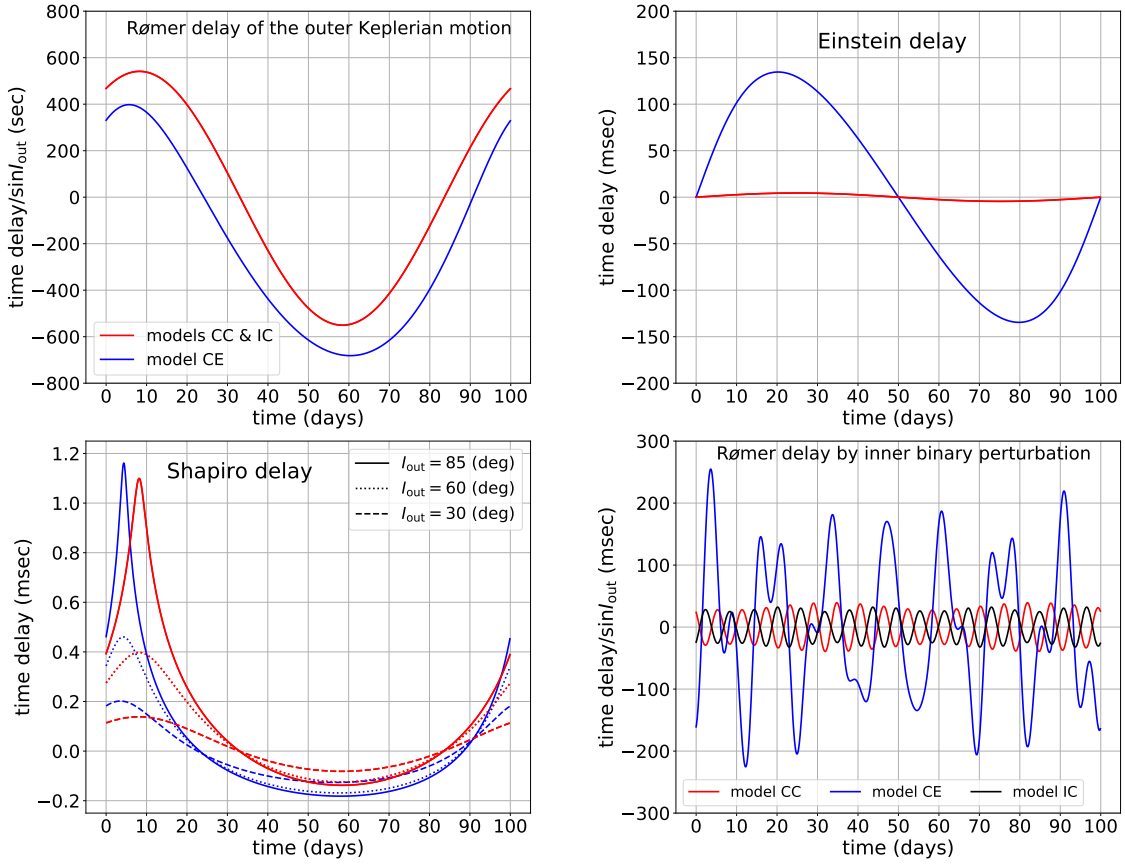

Figure 5.4 The time-delay curves of the Rømer delay by the outer Keplerian motion (upper-left), the Einstein delay (upper-right), the Shapiro delay (lower-left), and the Rømer delay induced by the inner binary perturbation (lower-right) for the three models listed in Table 5.1, respectively. The Rømer delay by the inner-binary perturbation only shows the time-delay modes associated with the inner-binary frequency $\nu_{\rm in}$. Adapted from HS2021.

5.5.1 Pulsar arrival timing constraints on existing binary neutron stars

Table 5.2 summarizes the current list of known DNS systems with their orbital parameters derived from the pulsar timing observations. Since they are interpreted as a binary system, m_{12} and m_{123} in Table 5.2 correspond to the companion mass of the pulsar, and the total mass of the system, respectively. Since both m_{12} and $m_{123} - m_{12}$ are in the typical mass range of neutron stars, it is very unlikely that those companions are really binaries of white dwarfs or black holes. Nevertheless, the null detection of the Rømer delay modulation due to the inner binary motion within the root mean square of the residuals $\sigma_{\rm rms}$ (the eighth column of Table 5.2) can put observational constraints on the inner binary.

In the practical analysis of the pulsar timing, however, the signals from a triple may be degenerated with other parameters on a pulsar, which may obscure the interpretation or even the presence of the inner BBH if one relies on the standard pipeline that neglects the possible triple effects. Therefore, an improved analysis taking account of such effects is required to constrain the system in a more quantitative and reliable fashion. This is so far beyond the scope, and therefore the following constraints should be interpreted as the proof of concept.

Because this is intended to be a merely proof-of-concept analysis, we simply constrain those systems by assuming a coplanar near-circular inner binary. Then using equation (5.9), the inner orbital period $P_{\rm in}$ is constrained as

$$\frac{K_{\rm BBH} P_{\rm in}}{4\pi c} \sin I_{\rm out} = \frac{1}{2} \frac{m_1 m_2}{m_{12}^2} \left(\frac{m_{12}}{m_{123}} \right)^{2/3} \left(\frac{P_{\rm in}}{P_{\rm out}} \right)^{7/3} x < \sigma_{\rm rms}. \tag{5.28}$$

If we further assume an equal-mass inner binary ($m_1 = m_2$), the above inequality reduces to

$$\frac{P_{\rm in}}{P_{\rm out}} < \left(\frac{8\sigma_{\rm rms}}{x} \right)^{3/7} \left(\frac{m_{123}}{m_{12}} \right)^{2/7} \approx 0.009 \left(\frac{\sigma_{\rm rms}}{10\ \mu{\rm sec}} \right)^{3/7} \left(\frac{x}{5\ {\rm sec}} \right)^{-3/7} \left(\frac{m_{123}}{m_{12}} \right)^{2/7}. \tag{5.29}$$

The second column of Table 5.3 corresponds to the above upper limit on $P_{\rm in}$ for a hypothetical equal-mass inner binary in a coplanar near-circular triple. Those upper limits on $P_{\rm in}$ are typically less than an hour, implying the future pulsar timing observation for pulsar – massive BH binary candidates, if discovered in future, would strongly constrain the unseen inner binary in a similar fashion.

5.5.2 Synergy with future low-frequency gravitational wave surveys

If $P_{\rm in}$ is sufficiently small compared with $P_{\rm out}$, the inner binary is difficult to be distinguished from a single massive object from the tiny anomalous tertiary motion since the perturbations get weaker. On the other hand, the gravitational wave (GW) from such short-period compact binaries may become detectable. Thus the presence of the

Table 5.2 List of known double neutron star systems

System	$P_{\rm pulse}$ (msec)	$P_{\rm out}$ (days)	$e_{\rm out}$	x (sec)	m_{123} ($M_\odot$)	m_{12} ($M_\odot$)	$\sigma_{\rm rms}$ (μsec)	$T_{\rm obs}$ (yrs)	Ref.
J0453+1559	45.8	4.072	0.113	14.467	2.733	1.174	3.88	2.4	(1)
J0509+3801	76.5	0.380	0.586	2.051	2.80	1.46	102.36	3.1	(2)
J0737-3039A	22.7	0.102	0.088	1.415	2.587	1.249	54	2.7	(3)
J0737-3039B	2773	0.102	0.088	1.516	2.587	1.249	2169	2.7	(3)
J1411+2551	62.5	2.616	0.170	9.205	2.538	> 0.92	32.77	2.4	(4)
J1518+4904	40.9	8.634	0.249	20.044	2.718	> 1.55	6.05	13	(5)
B1534+12	37.9	0.421	0.274	3.729	2.679	1.346	4.57	22	(6)
J1753-2240	95.1	13.638	0.304	18.115	–	> 0.4875	400	1.8	(7)
J1756-2251	28.5	0.320	0.181	2.756	2.571	1.230	19.3	9.6	(8)
J1757-1854	21.5	0.184	0.606	2.238	2.733	1.3946	36	1.6	(9)
J1811-1736	104.2	18.779	0.828	34.783	2.57	> 0.93	851.2	7.6	(10)
J1829+2456	41.01	1.176	0.139	7.237	2.606	1.310	10.086	17	(11)
J1913+1102	27.3	0.206	0.090	1.755	2.89	1.27	56	7.3	(12)
B1913+16	59.0	0.323	0.617	2.342	2.828	1.3867	–	29	(13)
J1930-1852	185.5	45.060	0.399	86.890	2.59	> 1.30	29	2.1	(14)
J1946+2052	17.0	0.078	0.064	1.154	2.50	> 1.18	95.04	0.2	(15)

The values are based on: (1) Martinez et al. (2015) (2) Lynch et al. (2018) (3) Kramer et al. (2006) (4) Martinez et al. (2017) (5) Janssen et al. (2008) (6) Fonseca et al. (2014) (7) Keith et al. (2009) (8) Ferdman et al. (2014) (9) Cameron et al. (2018) (10) Corongiu et al. (2007) (11) Haniewicz et al. (2020) (12) Ferdman et al. (2020) (13) Weisberg & Taylor (2005) and Taylor & Weisberg (1982) (14) Swiggum et al. (2015) (15) Stovall et al. (2018)

Table 5.3. Constraints on DNS Systems

System	$P_{\rm in,max}$ (hrs)	$h(4\pi/P_{\rm in,max})$	$t_{\rm merge}(P_{\rm in,max})$ (yrs)	D (kpc)
J0453+1559	0.463	8.4×10^{-22}	3.9×10^{6}	0.52
J0509+3801	0.384	1.0×10^{-22}	1.6×10^{6}	7.08
J0737-3039A	0.0939	1.2×10^{-21}	4.9×10^{4}	1.17
J1411+2551	0.946	1.6×10^{-22}	3.9×10^{7}	1.13
J1518+4904	0.952	4.5×10^{-22}	1.7×10^{7}	0.96
B1534+12	0.0878	1.8×10^{-21}	3.6×10^{4}	0.93
J1753-2240	–	–	–	6.93
J1756-2251	0.143	1.1×10^{-21}	1.6×10^{5}	0.95
J1757-1854	0.115	7.5×10^{-23}	7.1×10^{4}	19.6
J1811-1736	15.5	2.8×10^{-24}	6.6×10^{10}	10.16
J1829+2456	0.259	8.5×10^{-22}	6.8×10^{5}	0.91
J1913+1102	0.180	1.3×10^{-22}	2.7×10^{5}	7.14
B1913+16	–	–	–	5.25
J1930-1852	5.38	4.1×10^{-23}	2.3×10^{9}	2.48
J1946+2052	0.100	3.5×10^{-22}	6.5×10^{4}	3.51

Note. — The upper limits of inner orbital period from the equation (5.29), and the corresponding GW strain h (see equation (5.30)) and the merger time assuming equal-mass circular binaries. We assume minimum-mass companions for the systems that only the lower limits of companion masses are determined.
The fifth column denotes the mean values of the distances of the systems in Haniewicz et al. (2020), which are mainly determined by the dispersion measures.

inner binary can be probed in a complementary fashion by combining the pulsar timing and the GW data. Indeed as we show below, if the existing DNS systems have an inner BBH whose orbital period is shorter than the pulsar timing constraint, their low-frequency GW may be detectable by future space-based GW missions.

For instance, LISA (e.g. Amaro-Seoane et al. 2017), whose launch is scheduled in 2030's, will be sensitive to very low-frequency GW signals down to $\sim 10^{-4}$ Hz, and there are many proposals and discussions to search for the low-frequency GW sources with LISA, including compact binary (e.g. Nelemans et al. 2001), ultrashort-period planet (e.g. Cunha et al. 2018; Wong et al. 2019), and the ZKL oscillations (e.g. Gupta et al. 2020). We argue that an inner BBH in a triple that cannot be ruled out by the pulsar timing will be significantly constrained, or even detected by future space-based GW missions including LISA, DECIGO (e.g. Sato et al. 2017), and BBO (e.g. Harry et al. 2006).

In reality, the GW signals from an inner binary are also modulated in frequency and phase depending on the outer orbit parameters. Therefore, the precise detection of the inner BBHs in triple systems requires to take account of such triple effects simultaneously. In the following calculation, however, as a proof-of-concept, we simply assume that the outer orbital parameters are determined with high precision and properly subtracted from the entire signals. This is yet another reason why the following results should be regarded as a proof-of-concept example.

The characteristic amplitude of the GW strain emitted from a circular binary is (e.g. Hartle 2003; Schutz 2009)

$$h(\nu) \sim \frac{1}{a_{\rm in}(\nu) D}\left(\frac{2\mathcal{G}m_1}{c^2}\right)\left(\frac{2\mathcal{G}m_2}{c^2}\right) = \frac{2^{4/3}\mathcal{G}^{5/3}\mathcal{M}^{5/3}}{Dc^4}\nu^{2/3} \tag{5.30}$$

$$\approx 7.7\times10^{-20}\left(\frac{\mathcal{M}}{8.7\ M_\odot}\right)^{5/3}\left(\frac{P_{\rm in}}{0.01\ {\rm days}}\right)^{-2/3}\left(\frac{D}{1\ {\rm kpc}}\right)^{-1}, \tag{5.31}$$

where D is the distance to the system, ν is the GW frequency, which corresponds to $4\pi/P_{\rm in}$ for a circular binary, and $\mathcal{M}$ is the chirp mass of the binary:

$$\mathcal{M} \equiv \frac{(m_1m_2)^{3/5}}{m_{12}^{1/5}} \approx 8.7\ M_\odot\left(\frac{m_1m_2}{100\ M_\odot^2}\right)^{3/5}\left(\frac{m_{12}}{20\ M_\odot}\right)^{-1/5}. \tag{5.32}$$

As a specific example, we consider the DNS binary J0453+1559, and assume that it is indeed a triple with the unseen companion being a coplanar near-circular inner compact binary of the mass ratio m_2/m_1 and the orbital period $P_{\rm in}$, instead of a single neutron star. The left panel of Figure 5.5 plots the amplitudes of the corresponding GW strain (thick solid lines) and the Rømer delay modulation (thin dashed lines). The region above the red line $P_{\rm in} > P_{\rm in,max}$ is excluded because it should exhibit the arrival time modulation larger than the observed $\sigma_{\rm rms}$. Interestingly, the region below the limit indicates that the GW strain at the frequency corresponding to $4\pi/P_{\rm in,max}$ amounts to $h > 10^{-21}$ that may be detectable including LISA, DECIGO, and BBO; see Figure 5.6 below.

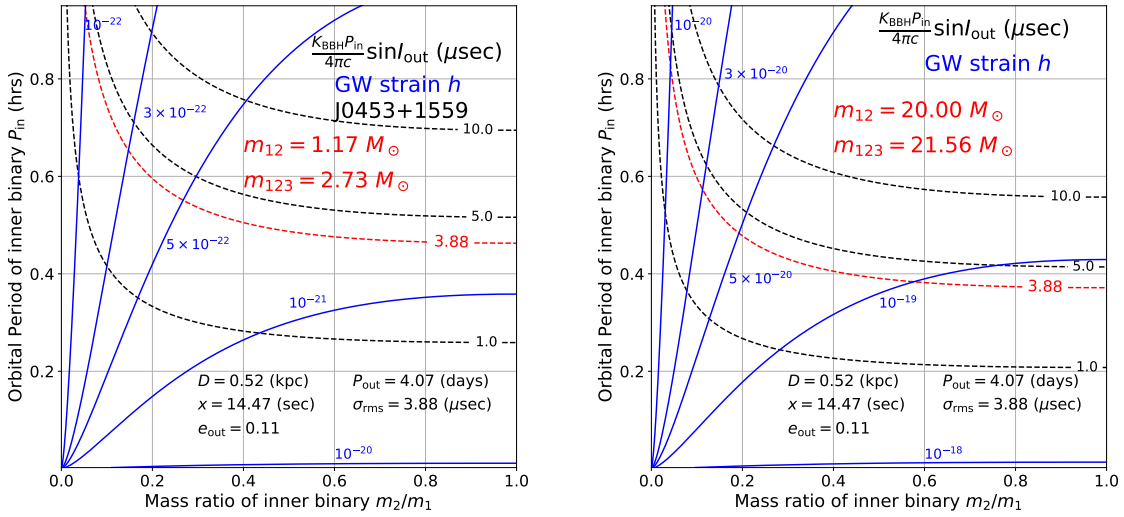

Figure 5.5 Characteristic amplitudes of the Rømer delay induced by the inner-binary perturbation (dashed black and red lines) and the gravitational wave strain h (solid blue line) as the function of inner-binary orbital period $P_{\rm in}$ and mass ratio m_2/m_1. The left and right panels show the constraints for J0453+1559 and a hypothetical inner BBH with $m_{12} = 20\ M_\odot$, respectively.Adapted from HS2021.

Assuming that each DNS system has an equal-mass circular inner binary, we can put rough constraints on the properties of the possible inner binaries. The GW emission merger time $t_{\rm merge}(P_{\rm in})$ for an equal-mass circular binary is (Peters 1964)

$$t_{\rm merge}(P_{\rm in}) = \frac{5}{64}\left(\frac{\mathcal{G}m_{12}}{c^3}\right)^{-5/3}\left(\frac{P_{\rm in}}{2\pi}\right)^{8/3} \approx 3.92\times10^7\left(\frac{P_{\rm in}}{\rm hrs}\right)^{8/3}\left(\frac{m_{12}}{M_\odot}\right)^{-5/3}\ {\rm yrs} \quad (5.33)$$

Table 5.3 summarizes the upper limit on the inner binary period $P_{\rm in,max}$, the corresponding GW strain $h(4\pi/P_{\rm in,max})$, and the GW emission merger time $t_{\rm merge}(P_{\rm in,max})$.

In order to examine the feasibility to constrain the inner BBH in triple systems, we assume exactly the same triple parameters for the DNS binary J0453+1559 except that the inner companion mass is $m_{12} = 20\ M_\odot$. The amplitudes of the Rømer delay modulation and the GW strain for the hypothetical system are plotted in the right panel of Figure 5.5. Since the GW strain becomes about two orders of magnitude larger compared with the left panel, an inner BBH, if exists at all, would be detected for almost all the the parameter space with either the precise high-cadence pulsar timing or the low-frequency GW observation.

Assuming monochromatic GW signals, the characteristic GW strain $h_{\rm c}$ for observational duration $T_{\rm obs}$ can be evaluated as follows (e.g. Moore et al. 2015; Wong et al. 2019):

$$h_{\rm c}(P_{\rm in}) = \left[2f\int_0^{T_{\rm obs}} h(t)^2\right]^{1/2} \approx \sqrt{2}\sqrt{\frac{T_{\rm obs}}{P_{\rm in}}}h, \quad (5.34)$$

where f and h are the GW frequency, and the amplitude of GWs, respectively. Figure 5.6 plots the characteristic GW strain $h_{\rm c}(P_{\rm in})$ for $T_{\rm obs} = 4$ yrs for hypothetical circular inner binaries; long-dashed, short-dashed, dotted and dash-dotted lines corresponds to the inner BBHs of $(m_1, m_2) = (30\ M_\odot, 30\ M_\odot)$, $(10\ M_\odot, 10\ M_\odot)$, $(15\ M_\odot, 5\ M_\odot)$, and $(5\ M_\odot, 5\ M_\odot)$, located at $D = 10$ kpc from us. Solid lines indicate $h(4\pi/P_{\rm in})$ from the existing DNS systems shown in Table 5.3, assuming an equal-mass circular inner binary instead of the companion neutron star. We also show the expected LISA sensitivity curve in 4 year mission (Robson et al. 2019), the expected sky-averaged sensitivity curves of DECIGO and BBO (Yagi & Seto 2011, 2017), and the aLIGO sensitivity curve from a technical note T1800044-v5 (Barsotti et al. 2018). The figure shows that very short-period inner binary companions are already excluded by non-detection with aLIGO, and the other space-based missions (LISA, DECIGO, and BBO) have enough sensitivity to detect an inner binary with hour-scale orbital period in the future.

Clearly, the joint analysis of the pulsar timing and GW observation is very effective, and can constrain the presence of an unseen inner binary in a complementary fashion; inner BBHs with a shorter orbital period that cannot be probed by the pulsar timing analysis will be detectable by future space-based GW detectors such as LISA, DECIGO, and BBO. Additionally, very short-period inner binaries with sub-second orbital periods can be already probed or constrained by current ground-based GW detectors such as aLIGO.

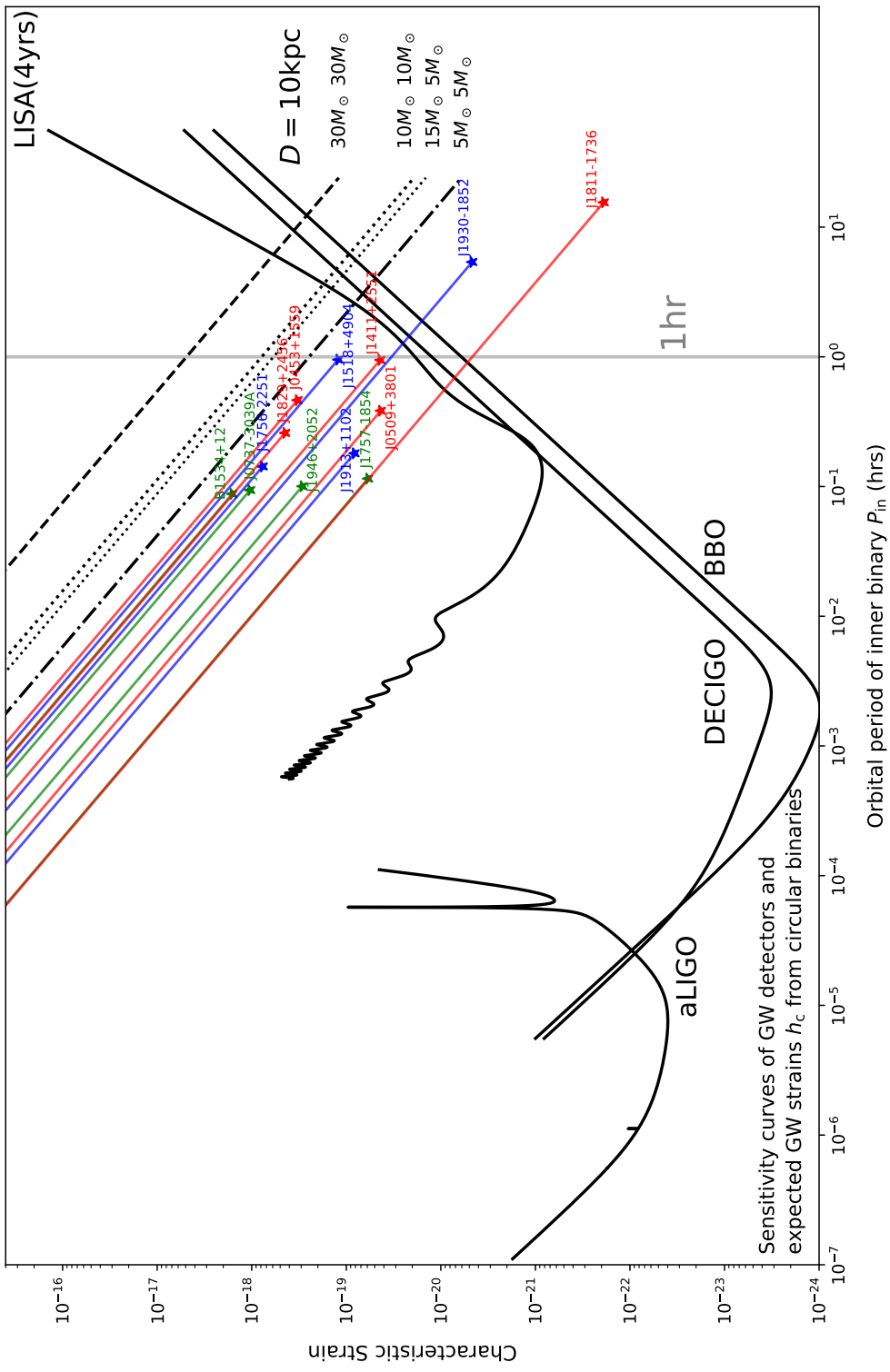

Figure 5.6 The sensitivity curves of three future space-based GW detectors (LISA, DECIGO, and BBO) and a present ground-based GW detector (aLIGO). The characteristic GW strains $h_c(P_{in})$ for $T_{obs} = 4$ yrs are also plotted for hypothetical inner circular BBHs located at 10 kpc, and assumed equal-mass circular inner binary companions in the currently known DNS systems. The stars represent the upper limit of inner orbital periods and corresponding GW strains (see Table 5.3). The DNS systems J1753-2240 and B1913+16 are not plotted in this figure since no constraints are available for these systems. All the results presented here assume that the GW modulations in frequency and phase by the outer orbit are properly subtracted by the predetermined outer orbital parameters.

5.6 Summary

In this section, we considered a pulsar-inner BBH triple, and proposed a method to search for an inner hidden BBH on the basis of the pulsar arrival time analysis. While the presence of such triples is currently uncertain, if such a triple exists, we show that pulsar timing with high precision and cadence can clearly detect a BBH inside distant triples beyond several kpc, inaccessible with the radial velocity observation.

We first showed that an inner hidden BBH can be identified from the short-term Rømer delay modulations induced by the inner-binary perturbation. The analytic approximate expression revealed the variations have sufficient amplitudes for detections. For instance, we showed that the amplitudes reach ~ 50 msec for our fiducial triples. We also found that the orbital parameters, such as masses and separations, can be unambiguously determined if we can detect relativistic delays simultaneously. In particular, it was shown that the detection of the Shapiro delay play an important role to determine the inclination, and the mass of each body. The Shapiro delay is $\sim$ msec for a nearly edge-on system in our fiducial cases. Therefore, the detection should be feasible, considering very high precision of pulsar timing observations (μsec-order precisions).

As one specific application of our method, we performed a proof-of-concept analysis, and put rough constraints on possible inner binary companions of existing double neutron-star binaries (DNS) using the root mean square of the residuals in observational arrival timing data. We found that our proposed method has the sensitivity even for inner binaries with relatively short orbital periods down to $\sim$ hrs when $P_{\rm out} < \mathcal{O}(1)$ day and the pulsar timing precision is on the order of μsec. While it is not likely that existing DNS systems indeed have inner binary companions instead of singles, the result indicated that the pulsar timing is very powerful, and may be complementary to future space-based GW detectors.

Furthermore. we discussed the possible synergy between our method and direct GW observations. For instance, inner BBHs with $\lesssim 1$ hr orbital period located at $\lesssim 10$ kpc should produce the GW strains detectable by future space-based GW detectors including LISA, DECIGO, and BBO. On the other hand, we showed that inner BBHs with more than hour-scale orbital period would be effectively searched for by the pulsar timing. Therefore, we concluded that we can cover a large parameter space of inner BBHs combining these two methods in the near future.

Chapter 6

Disruption timescale of triples

6.1 Introduction

The former three sections are devoted to proposing methods to search for an inner BBH inside a triple system. Furthermore, we started the dynamical stability of triples, especially the disruption timescale instead of just estimating the stability/instability. In this chapter, we show the results for this study. Since our proposed methods are applicable only when target triple systems have long survived lifetimes. Therefore, it is important to estimate the dynamical stability of triples to check the applicability of our methods. In addition, this study is important to understand the dependence of stability on orbital configurations to examine the plausible configurations of our target triples.

Even apart from the purpose, the dynamical stability is also very important on its own to understand the orbital evolution of triple systems. Observationally, it is known that more than 70 % of OBA-type stars and 50 % of FGK-type stars belong to multiple systems (Raghavan et al. 2010; Sana et al. 2012), and the number of triples increases continually even at the present epoch (e.g. Hajdu et al. 2021; Tokovinin 2021; Tokovinin & Latham 2020). In the context of BBH mergers, the ZKL oscillations in triples are widely discussed as a possible channel to accelerate the timescale before mergers (e.g. Liu & Lai 2018; Trani et al. 2021). Therefore, the stability of triples, and its dependence on the orbital configuration, get more and more important currently.

Indeed, there are many previous works that considered the stability/instability of triple systems. For instance, Mardling & Aarseth (1999) (hereafter, MA99) proposed a widely used criterion of the dynamical instability of triples. Their stability criterion was later extended to include the dependence of inner orbital elements (e.g. Mylläri et al. 2018) or general relativistic corrections (e.g. Wei et al. 2021). Nevertheless, such criteria judge only the instability of triples, but do not predict the timescale of instability. It is indeed important to consider how long a triple system remains a stable orbit to understand its evolutionary path. Depending on the orbital configuration, some systems may require Gyr-scale orbital evolution before disruption. The fact clearly demonstrates the practical importance to understand the disruption timescale,

in addition to the mere stable/unstable criteria.

Mushkin & Katz (2020) (hereafter, MK20) examined the instability timescale for triple systems consisting of inner and outer highly eccentric orbits by evaluating the Random-Walk-like energy transfer between the two orbits. They proposed a full Random Walk (RW) model, which uses a numerical secular integration, and a simplified RW model in the form of an analytic expression. They showed that both models can reasonably estimate the disruption time of triple systems with an outer very eccentric orbit. However, the RW model is not applicable for all the triple systems, and the limitation depending on the orbital configuration, including the mutual inclination and mass ratios, have not yet been evaluated.

In the present chapter, we compare the disruption time distributions of triples from the three-body simulations with the RW model estimation in MK20, and the dynamical stability criterion in MA99. We here present the results on how orbital configuration affects the disruption timescale distributions, concentrating on three extreme cases: coplanar prograde ($i_{\rm mut} = 0°$), orthogonal($i_{\rm mut} = 90°$), and coplanar retrograde triples($i_{\rm mut} = 180°$). We also consider the dependence on mass ratios $q_{21} \equiv m_2/m_1$ and $q_{23} \equiv m_2/m_3$, which change the mass hierarchy of triples (see Figure 6.2). The results show the importance of taking account of orbital configuration dependency of disruption times, and extending the disruption time estimation models in the future.

In our whole analyses, we assume that the disruption time is scalable on masses and orbital period. For instance, we assume that the disruption time becomes ten times longer if orbital periods are ten times. This assumption is important to justify that our results are not sensitive to the specific choices of masses and orbital periods. This is statistically justified using numerical simulations, and the results are included in appendix. We also briefly discussed the possible dependence of the initial phase values in appendix.

6.2 Initial Setup and Numerical Methods

Figure 6.1 shows the schematic configuration of a hierarchical triple system considered in the present section. The inner binary consists of two massive bodies of m_1 and m_2, and a tertiary with mass m_3 orbits around the binary. We define the primary as the most massive body in the inner binary (so that $m_1 \geq m_2$), and two mass ratios $q_{21} \equiv m_2/m_1$ and $q_{23} \equiv m_2/m_3$. Note that $0 < q_{21} \leq 1$, and $q_{23} > 0$. Figure 6.2 shows the schematic picture of triple systems for very different q_{21} and q_{23} regimes. In the figure, red, blue, and black filled circles correspond to primary. secondary, and tertiary. respectively. We can see that a triple consisting of an inner BBH and a tertiary, that is discussed in the former sections, corresponds to the upper two cases in the figure: $q_{23} > 1$. Nevertheless, the lower two cases with $q_{23} < 1$ are also interesting since stellar triples and planetary systems can belong to the cases.

The orbital parameters of inner and outer orbits are specified in terms of the Jacobi coordinates. Each orbit is characterized by the semi-major axis a_j, the eccentricity e_j,

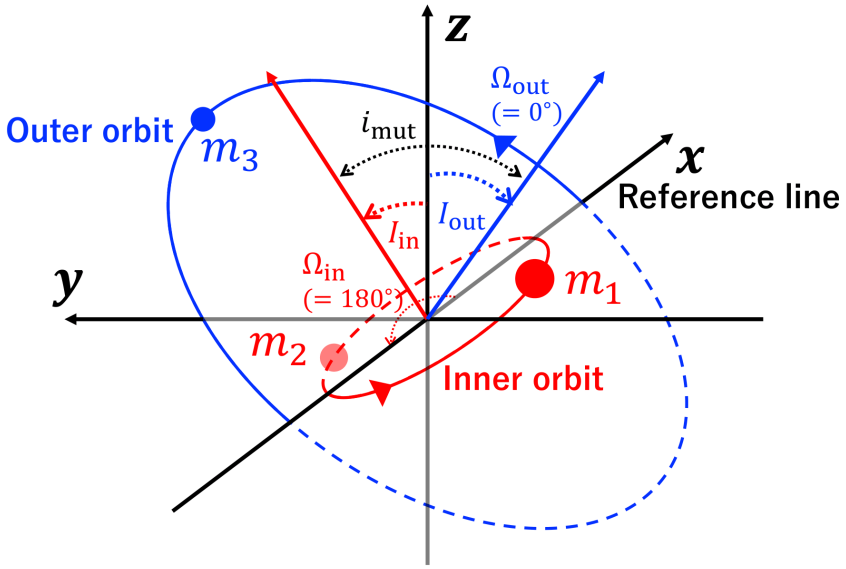

Figure 6.1 Orbital configuration of a triple system consisting of an inner binary and a tertiary. The origin of the reference frame is set to be the barycenter of the inner binary, instead of the triple.

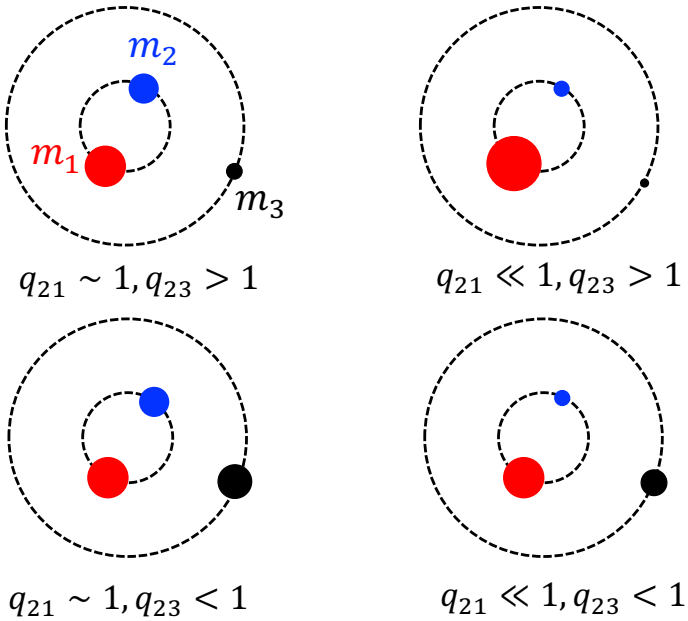

Figure 6.2 Schematic illustrations of triple systems for very different q_{21} and q_{23} regimes. Red, blue, and black filled circles correspond to the primary, secondary, and tertiary, respectively. Note that a triple considered in the former three sections belong to the upper two cases: $q_{23} > 1$. The mass of each body is schematically indicated as the size of filled circles.

and the argument of pericenter ω_j. The orientation of orbits in space are specified by the longitude of ascending nodes Ω_j measured from the reference line, and the mutual inclination $i_{\rm mut}$ between inner and outer orbits. Additionally, we define the orbital period for each orbit as P_j using the above parameters. The index $j = \{\rm in, out\}$ refers to the inner and outer orbits, respectively. Note that the orbital parameters are not constant with time in a triple.

In this chapter, we assume a fiducial set of parameters summarized in Table 6.1. We use these values for the input parameters unless otherwise specified. In order to check the dependence of disruption time $T_{\rm d}$ on the orbital configuration, we specifically vary the mass ratio of the inner binary q_{21}, the mass ratio of secondary and tertiary q_{23}, the outer semi-major axis $a_{\rm out}$, the outer eccentricity $e_{\rm out}$ and the mutual inclination $i_{\rm mut}$. Note that each mass of the body, m_1, m_2 and m_3 is determined by the values of mass ratios q_{21} and q_{23} when fixing m_{12}. The choice of the fiducial values in Table 6.1 is quite specific. This is because we consider an inner BBH with a few tens of $M_\odot$ and mall inner eccentricity $e_{\rm in}$ as our fiducial targets of proposed methods in chapter 3, 4, and 5. In appendix, we show that the normalized disruption time $T_{\rm d}/P_{\rm in}$ is statistically insensitive to specific choice of orbital period $P_{\rm in}$, inner binary mass m_{12}, and initial phases $\omega_{\rm out}$ and $M_{\rm out}$.

In order to obtain the disruption time distributions of triples, we perform a series of numerical simulations with the N-body integrator `TSUNAMI` (Trani et al. 2019, Trani et al., in prep.). `TSUNAMI` is an direct N-body integrator specifically designed to accurately simulate few-body systems. The code solves the Newtonian equations of motion derived from a time-transformed, extended Hamiltonian (Mikkola & Tanikawa 2013a,b). This numerical procedure, also called algorithmic regularization, serves to avoid the well known issue of gravitational integrators when two particles get very close together. When no regularization is employed, the acceleration grows quickly, and the timestep becomes extremely small, sometimes even halting the integration. Furthermore, `TSUNAMI` is suited to evolve hierarchical systems of particles like the ones examined here, thanks to its chain-coordinate system that reduces round-off errors when calculating distances between close particles far from the center of mass of the system (Mikkola & Aarseth 1993). Finally, `TSUNAMI` uses Bulirsch-Stoer extrapolation to improve the accuracy of the integration, ensuring accuracy and adaptability over a wide range of dynamical scales (Stoer & Bulirsch 2002). As a result, `TSUNAMI` can perform accurate three-body simulations roughly $10-100$ times faster than other integrators. In appendix E, we present the comparison of the orbital evolution simulated with `REBOUND` and `TSUNAMI`.

We define the disruption time $T_{\rm d}$ for each triple following the same criterion used in Manwadkar et al. (2021, 2020). At each timestep, the integrator evaluates the binding energy for each of the three pairs of bodies, *i.e.* (m_1, m_2), (m_1, m_3) and (m_2, m_3). The pair with the highest (negative) binding energy is considered as the inner binary, and we consider the pair constituted by the binary and the remaining body as the outer pair. If the binding energy of the outer pair is positive and its radial velocity is also positive (i.e. moving away from the innermost binary), we record the time as the

Table 6.1. Fiducial values for triple systems in chapter 6

orbital parameter	symbol	initial value
inner-binary mass	m_{12}	20 $M_\odot$
inner-binary period	$P_{\rm in}$	1000 days
inner eccentricity	$e_{\rm in}$	10^{-5}
inner pericentre argument	$\omega_{\rm in}$	180 deg
outer pericentre argument	$\omega_{\rm out}$	0 deg
inner longitude of ascending node	$\Omega_{\rm in}$	180 deg
outer longitude of ascending node	$\Omega_{\rm out}$	0 deg
inner mean anomaly	$M_{\rm in}$	45 deg
outer mean anomaly	$M_{\rm out}$	30 deg

Note. — We adopt these values for input of simulations as our fiducial systems unless otherwise specified. We consider $i_{\rm mut}$, $q_{21} \equiv m_2/m_1 (\leq 1)$, $q_{23} \equiv m_2/m_3 (> 0)$, $e_{\rm out}$, $\alpha \equiv a_{\rm in}/a_{\rm out}$ as varied parameters. Note that $a_{\rm in}$ is uniquely determined by m_{12} and $P_{\rm in}$, and m_1, m_2 and m_3 are uniquely determined by m_{12}, q_{21}, and q_{23}.

disruption time. We then wait until the binary-single distance is 20 times the binary semi-major axis before stopping the simulation. If a system rather survives after the total integration time $t_{\rm int}$, we stop the simulation and classify it as stable ($T_{\rm d} > t_{\rm int}$). We fix $t_{\rm int}$ value at $4 \times 10^7 P_{\rm in}$ unless otherwise specified.

In the following, we show some examples of typical evolution paths for triple systems. Figure 6.3 shows the time evolution of semi-major axis ratio α, inner eccentricity $e_{\rm in}$, outer eccentricity $e_{\rm out}$, mutual inclination $i_{\rm mut}$, and the type of temporary triple. The type of temporary triple is defined as described above. For instance, (1-3)-2 means a triple consisting of a (primary-tertiary) inner binary and a secondary orbiting around the binary. Top panel shows a typical orbital evolution of stable triples. In this case, we can see that the orbital parameters only vary within very limited ranges during whole evolution. As a result, the triple system survives beyond the integration time $4.0 \times 10^7\ P_{\rm in}$. On the other hand, middle panel shows a tertiary ejection at $t \approx 1.3 \times 10^5 P_{\rm in}$. Before the disruption, $e_{\rm in}$ and $e_{\rm out}$ increase suddenly, and the tertiary is ejected when $e_{\rm out}$ reaches unity. This is a typical evolution path for tertiary ejections. For orthogonal triples, another important path of disruption events is shown in bottom panel. Here, inner eccentricity $e_{\rm in}$ and mutual inclination $i_{\rm mut}$ evolve very drastically due to the ZKL oscillation. We see that $e_{\rm out}$ also varies with time complicatedly during the evolution. Finally, around $1.1 \times 10^5 P_{\rm in}$, secondary and tertiary are exchanged under an orbital crossing, and the secondary is soon ejected from the system. This is a typical path of secondary ejection under the ZKL oscillation.

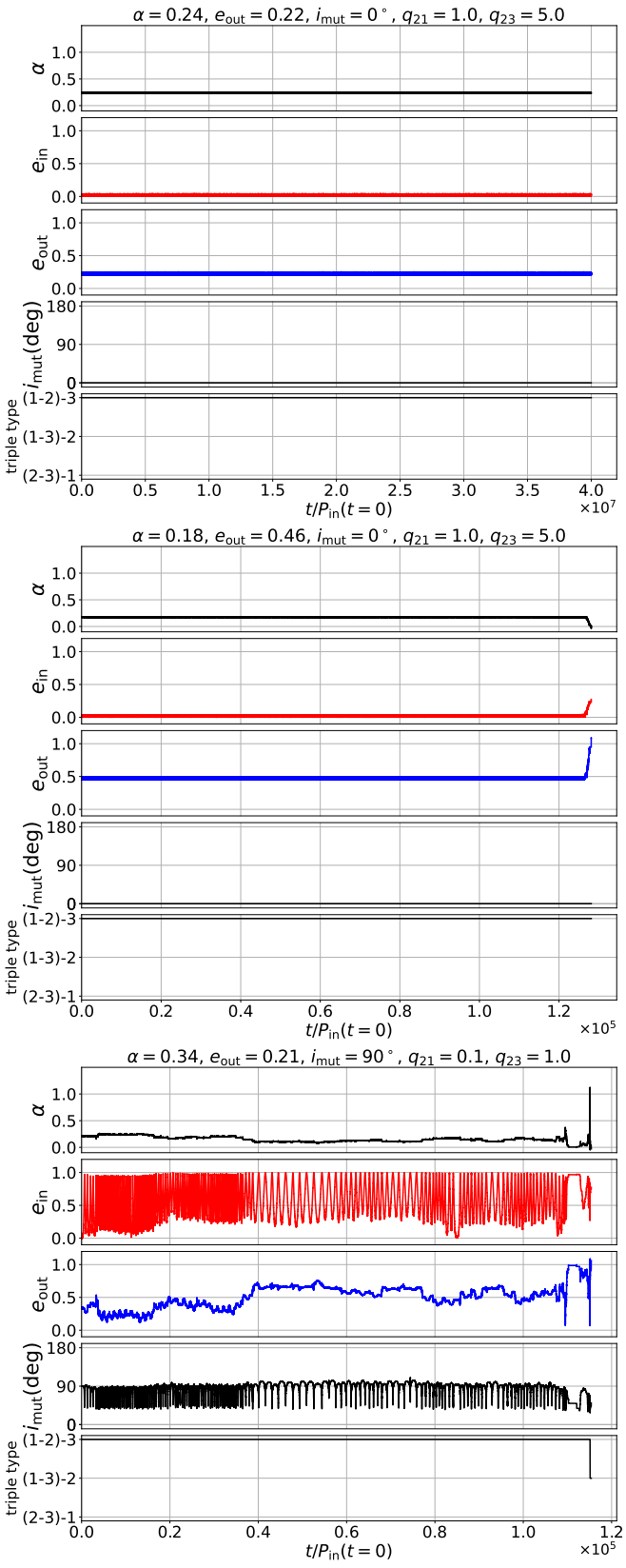

Figure 6.3 Examples of typical orbital evolution of triple systems. Top, middle, and bottom panels represent a stable triple, an unstable triple with tertiary ejection, and an unstable triple with secondary ejection. The specific choices of orbital parameters are specified above each panel.

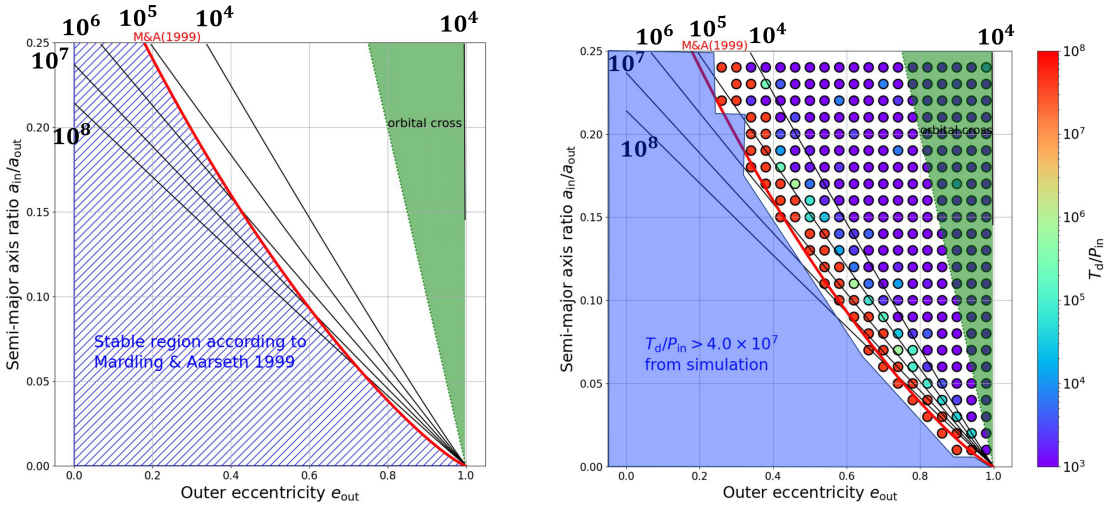

Figure 6.4 The disruption time $T_{\rm d}/P_{\rm in}$ dependence on $e_{\rm out} - \alpha$ for the coplanar, equal-mass inner binary case. The $T_{\rm d}(\alpha, e_{\rm out})$ is specified in colors. Left: The MA99 dynamical stability criterion (red curve) and the disruption time estimation from MK20 (black curves). The stable region from MA99 is denoted with shaded region. Right: The result from numerical simulations.

6.3 Example of disruption time distribution on $e_{\rm out}$ - α plane

In this section, we show an example result of disruption time distribution on $e_{\rm out}$ - α plane. We explain the way our simulations are performed for each orbital configuration along with the result.

Figure 6.4 shows the normalized disruption time $T_{\rm d}/P_{\rm in}$ distribution on $e_{\rm out}$ - α plane for coplanar, and equal-mass inner binaries ($i_{\rm mut} = 0°, q_{21} = 1$). The mass ratio q_{23} is fixed as 0.3, and therefore the tertiary mass m_3 is 3 $M_\odot$ for this specific case. Note that the input values of other orbital parameters are adopted from our fiducial values in Table 6.1. Since the disruption time $T_{\rm d}$ is statistically scalable with $P_{\rm in}$ as discussed in appendix, in what follows, we plot the normalized disruption time $T_{\rm d}/P_{\rm in}$ unless otherwise specified.

The left panel of Figure6.4 shows the predictions from the dynamical stability criterion in MA99 and the RW disruption time estimation model in MK20 on $e_{\rm out}$ - α plane. The red curve indicates the MA99 criterion and the black curves correspond to the disruption time contours according to MK20. The blue-shaded region represents the stable region according to MA99, and the green filled region represents the orbital crossing region, where the outer orbit crosses the inner orbit at the pericentre. We can clearly see that the estimations from MK20 are plotted as nearly straight lines on $e_{\rm out}$ - α plane. This is because the exponential term in the model of MK20 (see chapter 2, equation (2.41)) determines the disruption time estimation dominantly.

The right panel of Figure 6.4 shows the normalized disruption time distributions from simulations in color-coded circles. Our simulations were performed sequentially at each α from high $e_{\rm out}$ towards lower values. Due to the limitation of computational costs, we stopped each simulation at $t_{\rm int} = 4.0 \times 10^7 P_{\rm in}$, which is approximately equal to 0.11 Gyrs for our fiducial triple. If the system is stable up to $t_{\rm int} = 4.0 \times 10^7\ P_{\rm in}$ for two consecutive configurations in a sequence, we do not perform simulations for lower $e_{\rm out}$. As a result, the blue region in the right panel corresponds to $T_{\rm d} > 4.0 \times 10^7 P_{\rm in}$. In what follows, we adopt this procedure to obtain a series of disruption time data for each orbital configuration unless otherwise specified.

The right panel shows that the dynamical stability criterion of MA99 indeed agrees with the boundary of stable/unstable regions for a system with $i_{\rm mut} = 0^\circ$ and $q_{21} = 1$ (i.e. a coplanar and equal-mass inner binary triple). In the right panel, the MA99 criterion seems to coincide with $T_{\rm d} > t_{\rm int} = 4.0 \times 10^7 P_{\rm in}$, but there are likely much longer disruption times in the nominally stable region specified in blue colors in the plot. Later, we show that the simulated boundary does not always agree well with the MA99 criterion, depending on orbital configurations.

As for the RW model estimations from MK20, they agree well with the results from simulations only around the lower-right region in the plot, *i.e.* triples with high $e_{\rm out}$ and low α. This is expected and consistent with the assumption in MK20 since the RW model assumes a highly eccentric outer orbit. Indeed, MK20 confirms that the RW estimation is reasonable down to outer eccentricity 0.7. The right panel, furthermore, implies the value of $e_{\rm out}$ justifying the RW model also depends on α values. Later, we also see the RW estimations have significant discrepancy depending on $i_{\rm mut}$.

6.4 Comparison with simulated disruption times and previously proposed models: prograde, orthogonal, and retrograde orbits

In the present section, we show the comparison of the simulations and two models (MA99 and MK20), and discuss how orbital configuration affects the validity of the models. As three representative orbital configurations, we here concentrate on coplanar prograde ($i_{\rm mut} = 0^\circ$), orthogonal($i_{\rm mut} = 90^\circ$), and coplanar retrograde triples($i_{\rm mut} = 180^\circ$). For each orbital case, we adopt $q_{21} \equiv m_2/m_1 = 1$ and 0.1, and $q_{23} \equiv m_2/m_3$ =5.0, 1.0, and 0.5. Therefore, in total, 18 orbital configurations are considered here.

First, we show the $T_{\rm d}/P_{\rm in}$ distribution in terms of $x \equiv \alpha(1-e_{\rm out})^{-1}$ together with the MK20 RW model estimations, and discuss the dependence of orbital configuration on the disruption time. Next, we show the simulated stability boundary with $T_{\rm d}/P_{\rm in} > 4.0 \times 10^7$, and compare it with the MA99 and MK20 models.

6.4.1 Disruption time distribution in terms of x

The RW model in MK20 is written as follows (see equation (2.41) in chapter 2):

$$\begin{aligned}\log_{10}\frac{T_{\rm d}(x)}{P_{\rm in}} &= \log_{10}\left[2\left(\frac{m_{123}}{\mu_{12}}\right)^2 x^2\right] + \frac{4\sqrt{2}}{3}\sqrt{\frac{m_{12}}{m_{123}}}(\log_{10} e)x^{-3/2} + \log_{10}(1-e_{\rm out})^{1/2} \\ &\approx \log_{10}\left[2(1+q_{21})\left(1+\frac{1}{q_{21}}+\frac{1}{q_{23}}\right)x^2\right] \\ &+ 0.82\sqrt{\frac{1+q_{21}}{1+q_{21}+q_{21}/q_{23}}}x^{-3/2} + \log_{10}(1-e_{\rm out})^{1/2}, \end{aligned} \tag{6.1}$$

where we define x as $\alpha(1-e_{\rm out})^{-1}$, the ratio between the inner semi-major axis and outer pericenter distance. Since the equations is dominated by the $\mathcal{O}(x^{-3/2})$ term, we can make a clear comparison with simulations in terms of x.

Figure 6.5 shows the comparison of simulated $\log_{10} T_{\rm d}/P_{\rm in}$ and the RW model in terms of x. Top, middle, and bottom panels show the prograde ($i_{\rm mut} = 0°$), orthogonal ($i_{\rm mut} = 90°$), and retrograde cases ($i_{\rm mut} = 180°$), respectively, and left and right panels are divided according to q_{21} =1.0, and 0.1, respectively. In these plots, red open circle, blue cross, and black triangle represent the simulated $\log_{10} T_{\rm d}/P_{\rm in}$ for $q_{23} = 5.0$, 1.0, and 0.5, respectively. The RW model estimations are plotted by solid ($e_{\rm out} = 0.02$) and dotted curves $e_{\rm out} = 0.98$, where the eccentricity values correspond to the lower and upper limits in simulations, respectively. The curves are color-coded according to corresponding q_{23} values. Note that the clustered data around $\log_{10} T_{\rm d}/P_{\rm in} \sim 7.6$ are just due to the limitation of integration time ($t_{\rm int} = 4.0 \times 10^7 P_{\rm in}$).

First, we start from the top panels, which correspond to coplanar prograde cases. In both top-left and top-right panels, three different symbols corresponding to different q_{23} values do not show systematic difference. The fact indicates that q_{23} dependence is almost negligible for prograde orbits. The RW model also indicates that q_{23} dependence shows up but not significant. We can also see that simulated $\log_{10} T_{\rm d}/P_{\rm in}$ distributions go upwards for $q_{21} = 0.1$, which indicates the stabilization of the systems. The corresponding RW model estimations also predict the stabilization reasonably well. Therefore, in summary, the RW model represents the disruption time qualitatively well for prograde systems.

Middle two panels show the results for orthogonal systems ($i_{\rm mut} = 90°$). Contrary to prograde cases, both middle-left and middle-right panels show systematic q_{23} dependence. In the panels, we can see that the triples get stabilized as q_{23} increases (*i.e.* tertiary mass decreases). Interestingly, the RW model prediction on q_{23} dependence gets inverted from the simulations when $x \gtrsim 0.5$, and therefore different even qualitatively. This may indicate different disruption processes from the RW-like energy transfer such as the ZKL oscillations for orthogonal systems. As for q_{21} dependence, the RW model predict the systems are stabilized for smaller q_{21}. On the other hand, the middle-right panel shows that significant stabilization only appears when $x \gtrsim 0.5$, compared with the middle-left panel. As a result, the RW model tends to overestimate the disruption time for orthogonal triples with small q_{21} when $x \lesssim 0.5$.

Finally, bottom two panels show the results for retrograde cases. We can clearly see that retrograde systems are significantly stabilized contrary to the systems with the other two mutual inclinations. This is indeed consistent with the prediction that retrograde triples tend to be more stable in the previous stability/instability criterion (e.g. Mardling & Aarseth 1999, 2001; Mylläri et al. 2018). Interestingly, the disruption time distributions have very different shapes from the RW model estimation curves. In particular, the bottom-right panel shows small q_{21} value only stabilizes the systems when $x \lesssim 0.7$, resulting in very steep distribution against x. We can also see the clear dependence on q_{23}, and it is again different even qualitatively from the RW model prediction when $x \gtrsim 0.5$. The fact may also imply different processes from the RW-like energy transfer. This is a very interesting result since only different direction of orbits change significantly the disruption time distribution. Since retrograde systems are shown to have longer lifetime here, our proposed methods in the previous chapters would be more feasibly applicable to retrograde triples.

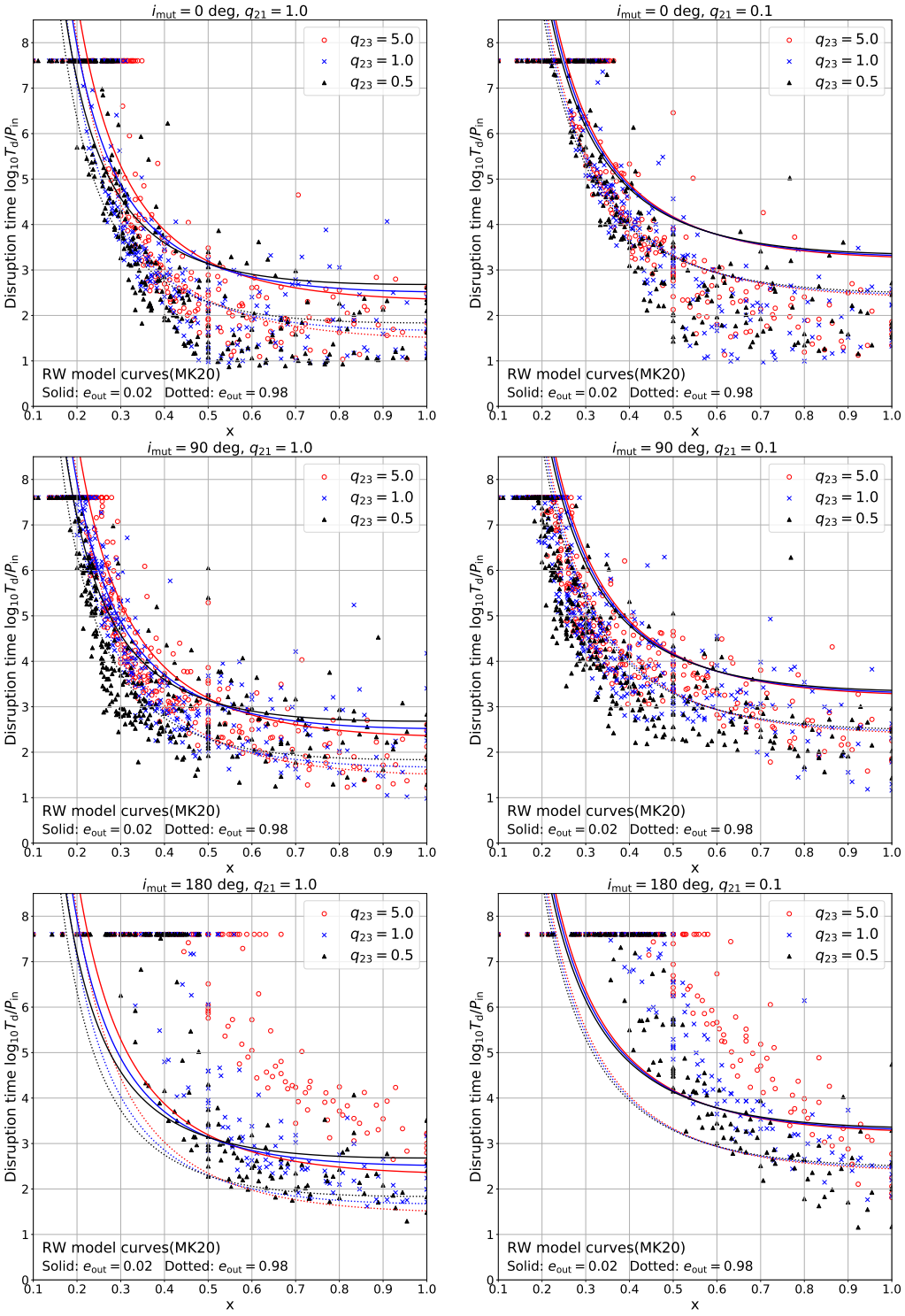

Figure 6.5 Normalized disruption time $T_{\rm d}/P_{\rm in}$ distributions in terms of x. The open red circle, blue cross, and black triangle correspond to $q_{23} = 5.0$, 1.0, and 0.5, respectively. The solid and dotted curves denote the corresponding RW model estimation for $e_{\rm out} = 0.02$ and 0.98, which represent the lower and upper limit eccentricities in the simulations, respectively. Top, middle, and bottom panels show the prograde, orthogonal, and retrograde cases, respectively. Left and right panels show the cases for q_{21} =1.0, and 0.1, respectively.

6.4.2 Boundary corresponding to $> 4.0\times10^7 P_{\rm in}$ disruption time on $e_{\rm out}$ - α plane

In the present subsection, we show the simulated stability boundary corresponding to $> 4.0 \times 10^7 P_{\rm in}$ disruption time. The definition of boundary is same as Figure 6.4. We here compare these boundaries for prograde, orthogonal, and retrograde triples, with the MA99 dynamical stability criterion and the RW model estimation corresponding to $4.0 \times 10^7 P_{\rm in}$ disruption time.

Figure 6.6 shows $> 4.0 \times 10^7 P_{\rm in}$ disruption time boundaries on $e_{\rm out}$ - α plane. Top, middle, and bottom panels show the prograde, orthogonal, and retrograde cases, respectively. Left and right panels are divided according to the values of q_{21} ($q_{21} = 1, 0.1$, respectively). In each plot, open red circle, blue cross, and black triangle denote $q_{23} = 5.0$, 1.0, and 0.5, respectively. The MA99 criterion are plotted as dashed curves, and the RW estimations corresponding to $4.0 \times 10^7 P_{\rm in}$ disruption time are plotted as solid curves. The color of each curve is determined according to q_{23} values.

In Figure 6.6, we can see that the boundaries do not monotonically change as the mutual inclination $i_{\rm mut}$ increases. First, the top panels show that the MA99 criterion agrees well with the simulated stability boundaries. Since the MA99 criterion does not represent any specific timescale, this coincidence implies that the disruption timescale gets significantly longer inside the stability boundary. The RW estimation curves clearly show that the model is applicable only for large $e_{\rm out}$, and underestimate the disruption timescale inside the stability boundary.

In the middle two panels (orthogonal cases), contrarily, the MA99 criterion, which includes monotonic stabilization on $i_{\rm mut}$, overestimates the stability for $i_{\rm mut} = 90^\circ$. The middle two panels also show that the simulated stability boundaries are sensitive to q_{23} values especially for small q_{21} and large α. These fact may indicate that the ZKL oscillations, which enhance $e_{\rm in}$ significantly, affect the stability for orthogonal triples. Interestingly, the RW estimation curves apparently agree well with the boundaries for $q_{21} = 1$ even towards smaller $e_{\rm out}$. On the other hand, the RW model curves overestimate the disruption timescale for $q_{21} = 0.1$.

Finally, the bottom two panels (retrograde cases) show that the MA99 criterion underestimates the stability boundary. Additionally, contrary to the expectation of MA99 criterion, the dependence on q_{21} is not significant for the simulated stability boundary here. The RW model estimations also only agree for very high values of $e_{\rm out}$, and underestimate otherwise. This result clearly shows that retrograde triples are especially important for our proposed methods since the systems should be stable even for large values of α, with which we can expect large perturbations on a tertiary.

6.5 Summary

In this chapter, we considered the disruption timescale of triples for prograde, orthogonal, and retrograde triples. We performed the three-body simulations, and compared the disruption timescale with two currently proposed models, the dynamical stabil-

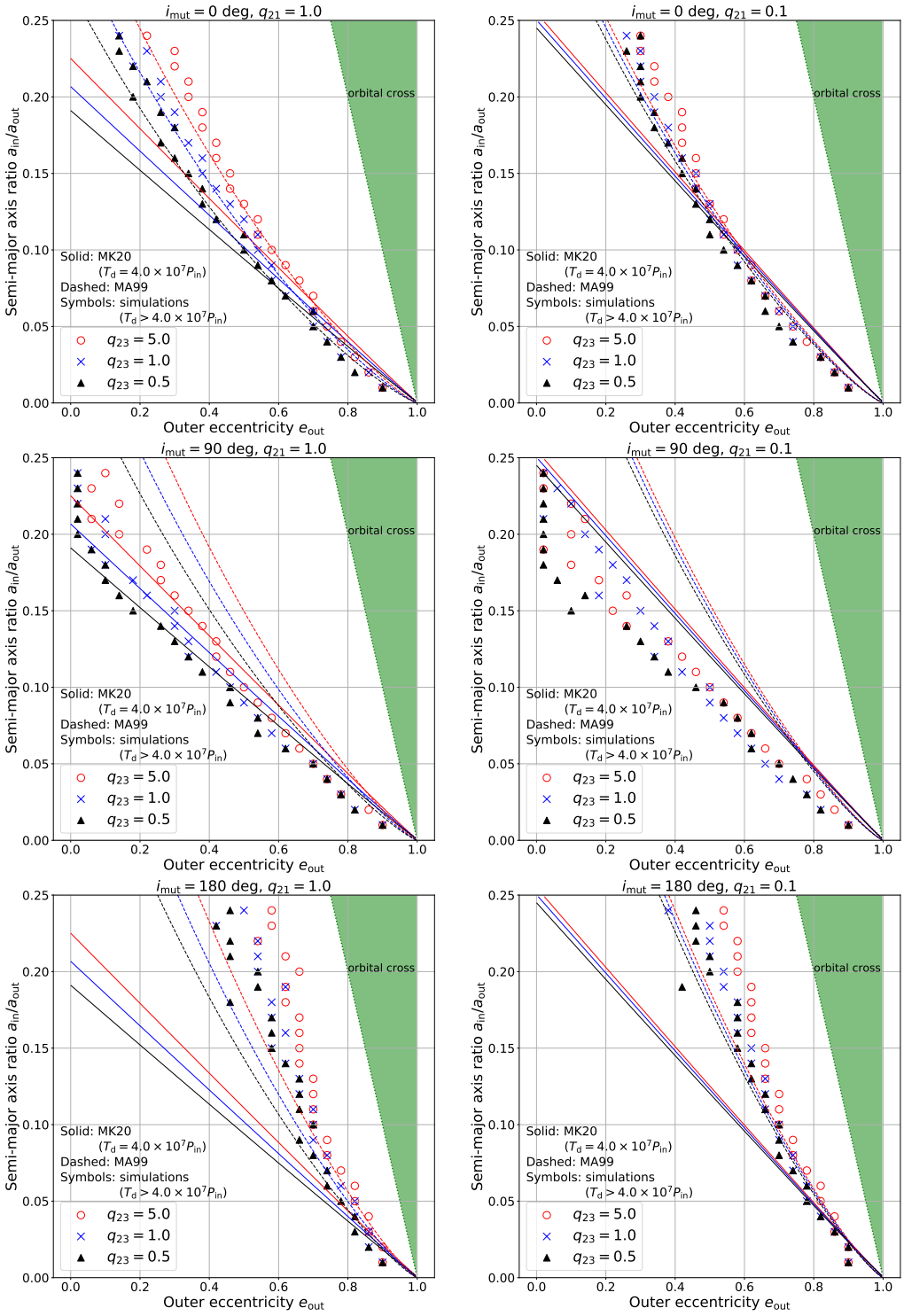

Figure 6.6 Boundary corresponding to $> 4.0 \times 10^7 P_{\rm in}$ disruption time on $e_{\rm out}$ - α plane. The boundary is defined samely as Figure 6.4. The open red circle, blue cross, and black triangle correspond to $q_{23} = 5.0$, 1.0, and 0.5, respectively. The solid and dashed curves correspond to the RW model estimation at $T_{\rm d} = 4.0 \times 10^7 P_{\rm in}$, and the dynamical stability criterion in MA99. The curves are color-coded according to q_{23}. Top, middle, and bottom panels show the prograde, orthogonal, and retrograde cases, respectively. Left and right panels show the cases for q_{21} =1.0, and 0.1, respectively.

ity criterion in MA99, and the RW disruption time estimation model in MK20. We found that the criterion in MA99 agrees well with the simulated stability boundary for prograde case, but gets worse for orthogonal and retrograde cases: orthogonal triples are more unstable, and retrograde triples are more stable than the predictions. It was also shown that the RW model is reasonable for prograde triples with high outer eccentricity, but has qualitative differences on q_{21} and q_{23} dependence for orthogonal and retrograde triples. The result implies that different physical processes from the RW model take place there, and it is worth studying in detail separately.

In order to extend the disruption time estimation model, we consider to proceed the study about the dependence of disruption times on orbital configurations, and seek the different physical processes causing discrepancy. Although the study has not yet accomplished, we here show a preliminary result which may include a hint to find the processes. Figure 6.7 shows the dependence of ejection rate of each body on q_{23}. The primary ejection, secondary ejection, tertiary ejection, and no ejection are color-coded in red, blue, black, and grey, respectively. Top and bottom panels show prograde and orthogonal cases, and upper and lower plots in each panel correspond to $q_{21} = 1.0$ and 0.1, respectively. The figure clearly shows the ejection of inner less massive body dominates over all ejections as q_{23} decreases although the tertiary ejection is dominant for large q_{23}. Note that primary and secondary have same masses when $q_{21} = 1$, and no physical difference is included. Comparing left and right panels, we can see the $q_{23]}$ dependence is larger for orthogonal case. Since the tertiary ejection is likely in the RW model, if the ejected bodies are different from tertiaries, the disruptions may be dominated by different processes.

Furthermore, in orthogonal triples, the ZKL oscillations may also play an important role on the stability. Currently, the ZKL oscillations in nearly orthogonal triples are discussed as a possible channel to accelerate the timescale before BBH mergers (e.g. Liu & Lai 2018; Trani et al. 2021). Therefore, the stability of orthogonal triples will be also important to confirm the validity of this channel. Retrograde triples are also worth studying in detail. They tend to be more stable, and therefore it is possible that our target triples are dominated by this orbital configuration, if the formation processes of our target triples do not avoid retrograde orbits.

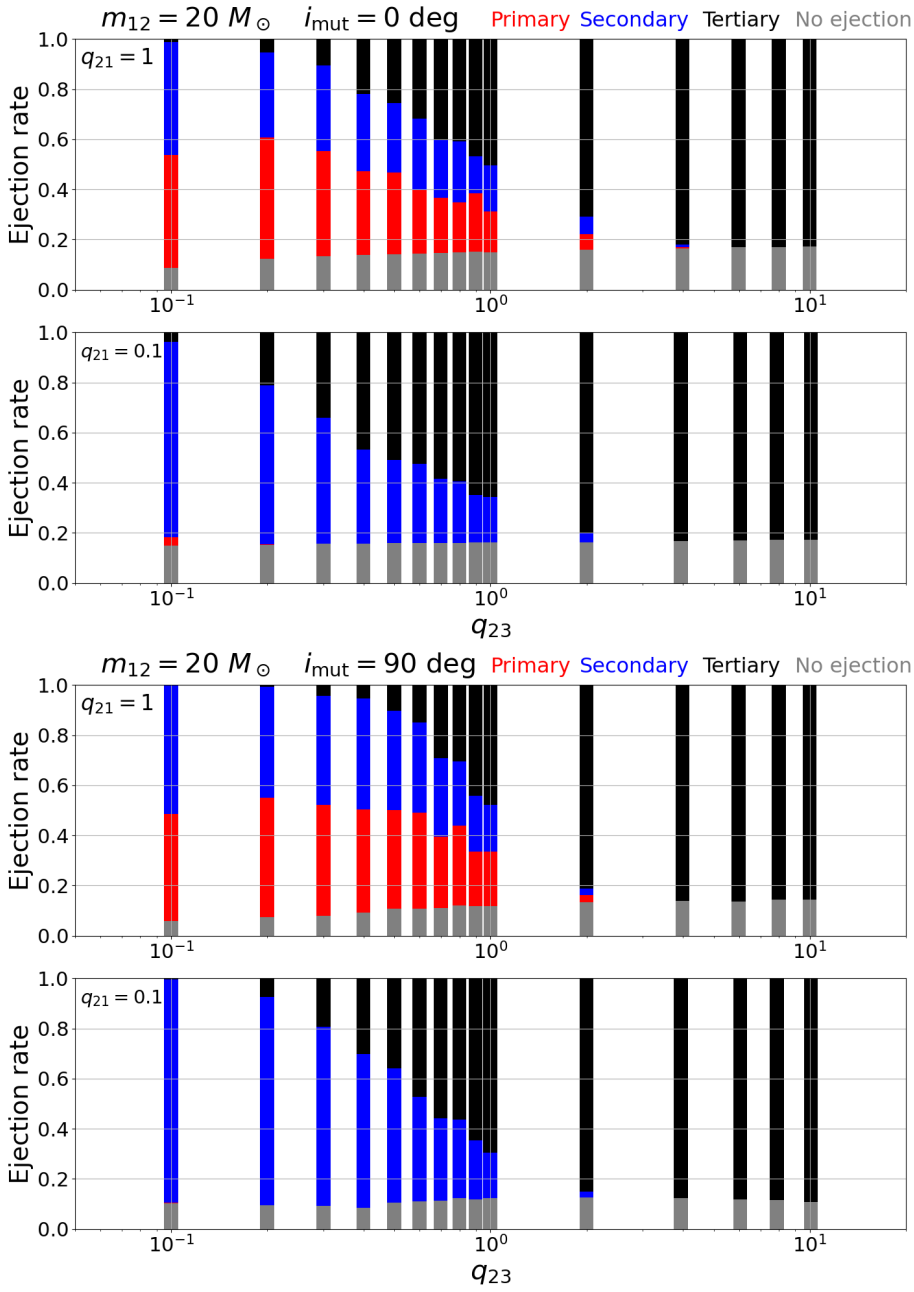

Figure 6.7 The dependence of ejection rate of each body on q_{23}. Red, blue, black, and gray colors represent primary ejection, secondary ejection, tertiary ejection, and no ejection, respectively. Top and bottom panels show prograde and orthogonal cases, respectively. In each panel, upper and lower plots correspond to $q_{21} = 1.0$ and 0.1, respectively. Note that primary and secondary are arbitrarily determined for the equal-mass inner binary case ($q_{21} = 1$), and no physical difference is included.

Chapter 7

Summary and conclusion

Since LIGO's first discovery of the gravitational waves (GWs) from a BBH merger in 2015, the number of observed BBH mergers has rapidly increased at the present epoch (e.g. The LIGO Scientific Collaboration et al. 2021b). We even expect that abundant BBH mergers will be effectively detected with the collaborations of ground-based GW detectors such as LIGO (e.g. The LIGO Scientific Collaboration et al. 2021b), Virgo (e.g. Virgo Collaboration et al. 2021), and KAGRA(e.g. Akutsu et al. 2021). Currently, the origin and formation scenarios of them are extensively discussed in astrophysics (e.g. Belczyński & Bulik 1999; Belczynski et al. 2012, 2016, 2002, 2007; Bird et al. 2016; Dominik et al. 2012, 2013; Kinugawa et al. 2014, 2016; O'Leary et al. 2009, 2006; Portegies Zwart & McMillan 2000; Rodriguez et al. 2016; Sasaki et al. 2016, 2018; Tagawa et al. 2016). Regardless of the details of such proposed scenarios, newly formed BBHs should experience long-term GW emissions before mergers in general. Therefore, we naturally anticipate that a large fraction of progenitor BBHs with wide-separations are hidden in the universe. Nevertheless, such progenitor BBHs have not yet been discovered because they usually never emit any detectable signals. In general, they needs to be searched for via the behaviors of near-by objects.

From observations, it is known that a majority of massive stars actually belong to multiple systems (Raghavan et al. 2010; Sana et al. 2012), and the observed fraction even increases with the masses of stars (e.g. Moe & Di Stefano 2017). A few triple systems, including compact objects, were indeed discovered recently (e.g. Gomez & Grindlay 2021; Lennon et al. 2021a; Ransom et al. 2014). These facts imply a fraction of progenitor BBHs may belong to triple systems as a result of stellar evolution although the detail formation processes are still behind a veil due to the complexity of their evolution. In addition, some previous studies suggested the formation of triples including inner BBHs via dynamical captures in clusters (e.g. Antognini 2015; Fragione et al. 2020; Trani et al. 2021). If such triples really exist, they should be very interesting astronomical targets on their owns. If they are discovered, we will be able to extend our knowledge on the universe.

In this thesis, we consider a hierarchical triple consisting of an inner progenitor BBH and a visible tertiary, and study the plausibility of detecting such triples through observing visible tertiary objects. We first propose three novel methods to search for

inner progenitor binary black holes (BBHs) through detecting the anomalous motions of tertiary. We next start a study of the dynamical stability for such triples, which is indeed mandatory to guarantee the feasibility of our methods.

In the present thesis, we showed that these triples, if exist, can be identified through the precise detection of anomalous tertiary motions. In particular, coplanar triples will be searched for effectively using the short-term RV variations. Although the variations are quite tiny compared with the Kepler motion RV, we found that they will be still detectable through intensive and precise follow-up RV monitoring. For instance, our fiducial triples with week-scale and month-scale inner and outer orbital periods, causes $\mathcal{O}(100)$ m/s RV variations with week-scale periods. This amplitude is indeed much larger than the current best precision of RV method ($\mathcal{O}(1)$ m/s), which is usually applied to detect extrasolar planets. We conclude that it is possible to search for the triples in the case of near-by ($\ll$kpc) and bright stars ($\lesssim$ 15 mag) if the precise RV detections ($\lesssim \mathcal{O}(10)$ m/s) are possible.

Furthermore, we showed that inclined triples with relatively short outer orbital periods are efficiently searched for using the long-term RV variations. The amplitude reaches comparable to the Kepler motion itself in principle. For instance, we expect $\mathcal{O}(100)$ km/s signals for our fiducial inclined triples. Although the variation timescale is very long in general, we showed that the variations are detected within decades when inner and outer orbital periods are week-scale and month-scale, respectively. Since the amplitude is very huge, it will be easier to detect them even without high precision RV monitoring. Interestingly, inclined triples, including inner BBHs, are widely discussed as possible sources of GW merger events since the ZKL oscillations work effectively there, and decrease the timescale before coalescence (e.g. Liu & Lai 2018; Trani et al. 2021). Therefore, the discovery of inclined triples will be very important even from the theoretical point of view.

We found that pulsar arrival time variations are also a promising probe of progenitor inner BBHs. Although the number of tertiary pulsars is likely to be smaller than tertiary stars, the pulsar timing will applied for more distant triples beyond kpc scale with great precision. It was shown that we can even determine orbital parameters of inner BBHs very precisely without degeneracy. Moreover, we found that it is possible to cover large parameter space of inner BBHs, combining precise pulsar timing with future space-based GW detectors such as LISA (Amaro-Seoane et al. 2017), DECIGO (Sato et al. 2017), and BBO (Harry et al. 2006). Therefore, in the future, we expect effective searches for (BBH - pulsar) triples, which are, if exist, interesting themselves.

We also started a study on the dynamical stability and the disruption timescale of triples. We found that preciously proposed models (Mardling & Aarseth 1999; Mushkin & Katz 2020) are applicable only to a limited range of orbital configurations. In particular, we showed that retrograde triples are significantly stable, and have long lifetime. The fact implies the possibility that our target triples are dominated by retrograde systems. It will be important to study retrograde triples separately, in order to identify what process caused discrepancy from the previous models. We will proceed this study, and possibly extend the disruption time estimation models

including orbital configuration dependency.

Next, we would like to discuss future prospects of our study in this thesis. We expect that many (star - unseen companion) binaries will be discovered with Gaia and TESS in the near future. For instance, Yamaguchi et al. (2018) predicted that $200-1000$ such binaries will be detected with Gaia, and Masuda & Hotokezaka (2019) expected that $10-100$ such ones will be detected with TESS. Gaia Full Data Release 3 is planned in 2022, and such binaries will be discovered in due course. Furthermore, rapid improvement of observational instruments are currently achieved, and large-scale surveys are planned successively at the present epoch. For instance, Large Synoptic Survey Telescope (LSST) (e.g. Ivezić et al. 2019) plans to start large-scale regular survey by 2022. In the future, we will hopefully know more and more (star - unseen companion) binaries, and we will possibly have an opportunity to propose followup observations. If such a binary turns out to be a triple in the future, it should be a great discovery as the first detection of progenitor BBHs, and triple systems including compact binaries.

We also would like to emphasize our methods are not only applicable to triples with massive inner binaries. Our study is based on three-body dynamics, which is very robustly applied to many astrophysical objects. For instance, extrasolar binary planets were predicted theoretically (e.g. Ochiai et al. 2014), and it was proposed to search for them using transit observations (e.g. Lewis et al. 2015). However, transit observations are only applicable when binary planet is close to edge-on with respect to the line of sight, and repeatedly hide the surface of a host star. This situation is actually very limited, and therefore, it is very interesting to consider RV variations of a host star induced by a binary planet, and study the plausibility of surveys via RV observations.

On the dynamical stability of triples, it is also important to include general relativistic (GR) corrections such as precessions, and GW emissions. The GR precession should suppress the ZKL oscillations effectively, depending on orbital configurations. In addition, GW emissions should change the semi-major axis ratio through the shrinkage of inner orbital separations. Therefore, these corrections would affect the disruption process, and the stability of triples. Interestingly, Fragione et al. (2020) found that most of triple systems including compact binaries formed via dynamical captures in clusters are expected to be black hole triples, in which all three objects are black holes. This is very interesting to consider the detectability of such triples with future space-based GW detectors such as LISA, DECIGO, and BBO. In the sense, GR corrections are especially important, and contribute to establish the detection methodology of black hole triples.

Finally, we would like to close this thesis by emphasizing the purpose and conclusion. So far, close massive BBHs are detected only through GWs from merger events. In the present thesis, we proposed different methods from GW observations to detect progenitor BBHs with relatively wide separations hidden in triple systems. We showed that such BBHs can be identified with RV and pulsar arrival time variations of visible tertiaries. We expect that (star - BBH) triples will be searched for from candidate

(star - unseen companion) binaries in the future. If such a triple are successfully discovered, the discovery will be remarkable in astronomy as the first detection of not only progenitor BBHs, but also triples including compact binaries.

Acknowledgments

First of all, I would like to express my gratitude to supervisor Yasushi Suto for his advice on research and discussion during seminars. Although the research in this thesis faced many difficulties, he always gave me good advice when I tackled such difficulties, and therefore I was able to overcome them each time. I am also grateful to my research collaborators, Shijie Wang and Alessandro Trani for their helps and advice on the studies in this thesis. Chapter 3 is based on a collaboration with Shijie Wang, and he always gave me good speculations about dynamics. Chapter 6 is based on an on-going collaboration with Alessandro Trani. Indeed, he is one of the developers of N-body integrator "`TSUNAMI`", which the result in chapter 6 highly relies on. He also gave me good advice on triple dynamics, numerical codes, and so on during our regular weekly discussions.

My research is also supported by helps and advice from many other researchers. Here, I would like to emphasize my gratitude for them. I thank Makiko Nagasawa, Anna Lisa Varri, Re'em Sari, and Toshio Fukushima for discussion on dynamical evolution of many body systems and giving comments on our study. I am also grateful to Mamoru Sekido, Keitaro Takahashi, and Hiroki Kumamoto for discussion on the pulsar timing analysis, which the results in chapter 5 are owed to much.

During weekly seminars and daily life in my group, I studied a lot on various aspects of astrophysics from many people. I also would like to express my gratitude for them here. In particular, I would like to thank Kazuhiro Kanagawa, Shoya Kamiaka, Masataka Aizawa, Yuta Nakagawa, Shijie Wang, and Yuting Lu for giving me great insight on planetary physics during weekly planet seminars. I am also grateful to all other members belonging to the University of Tokyo Theoretical Astrophysics (UTAP) and Research Center for the Early Universe (RESCEU) for many good comments on this study and thesis. I also would like to acknowledge JSPS fellowship for doctoral course and JSPS KEKENHI Grant Number JP21J11378, which support the study in this thesis. The simulations in chapter 6 are performed in the calculation server of CfCA. Finally, I express my thanks to my family for supporting my life both mentally and economically.

Appendix A

Constraint on a possible inner unseen binary in a binary system 2M05215658+4359220

As one specific application of the short-term RV variations, we here put a constraint on a possible inner unseen binary in a binary system 2M05215658+4359220. This kind of procedure is also useful to design our follow-up RV observations since we can see the expected amplitudes of signals for a given $P_{\rm in}$ and m_2/m_1 beforehand.

We put a constraint using the following characteristic amplitude $K_{\rm BBH}$ of the short-term RV variations for coplanar circular triples:

$$K_{\rm BBH} \equiv \frac{m_1 m_2}{(m_1+m_2)^2}\sqrt{\frac{m_1+m_2+m_*}{m_1+m_2}}\left(\frac{a_{\rm in}}{a_{\rm out}}\right)^{3.5} K_0 \tag{A.1}$$

with $a_{\rm in}$ being the semi-major axis of the inner binary.

Figure A.1 plots a color contour map of $K_{\rm BBH}$ as a function of the mass ratio m_2/m_1 and the orbital period $P_{\rm in}$ of the possible inner binary for the 2M05215658+4359220 system assuming an unseen companion is actually an invisible binary. We adopt the values of orbital parameters from Table 2.1 in chapter 2. The color is coded according to the value of $K_{\rm BBH}$ that labels the contour curves.

The axis on the right indicates the semi-major axis ratio $(a_{\rm in}/a_{\rm out})$ corresponding to the orbital period $P_{\rm in}$ of the left axis. Note that the approximation formula is degraded towards the upper part of Figure A.1. Indeed the three-body system becomes dynamically unstable if it satisfies (Mardling & Aarseth 1999, 2001)

$$\alpha > \left(\frac{a_{\rm in}}{a_{\rm out}}\right)_{\rm crit} \equiv \frac{1-e_{\rm out}}{2.8}\left(\frac{(1+m_3/(m_1+m_2))(1+e_{\rm out})}{\sqrt{1-e_{\rm out}}}\right)^{-\frac{2}{5}} \approx 0.270. \tag{A.2}$$

Thus, the perturbation result completely breaks down there as indicated by the black area in Figure A.1. Although the approximation formula is degraded for large $(a_{\rm in}/a_{\rm out})$, we can still conservatively estimate the semi-amplitude of RV variations in the allowed region of Figure A.1.

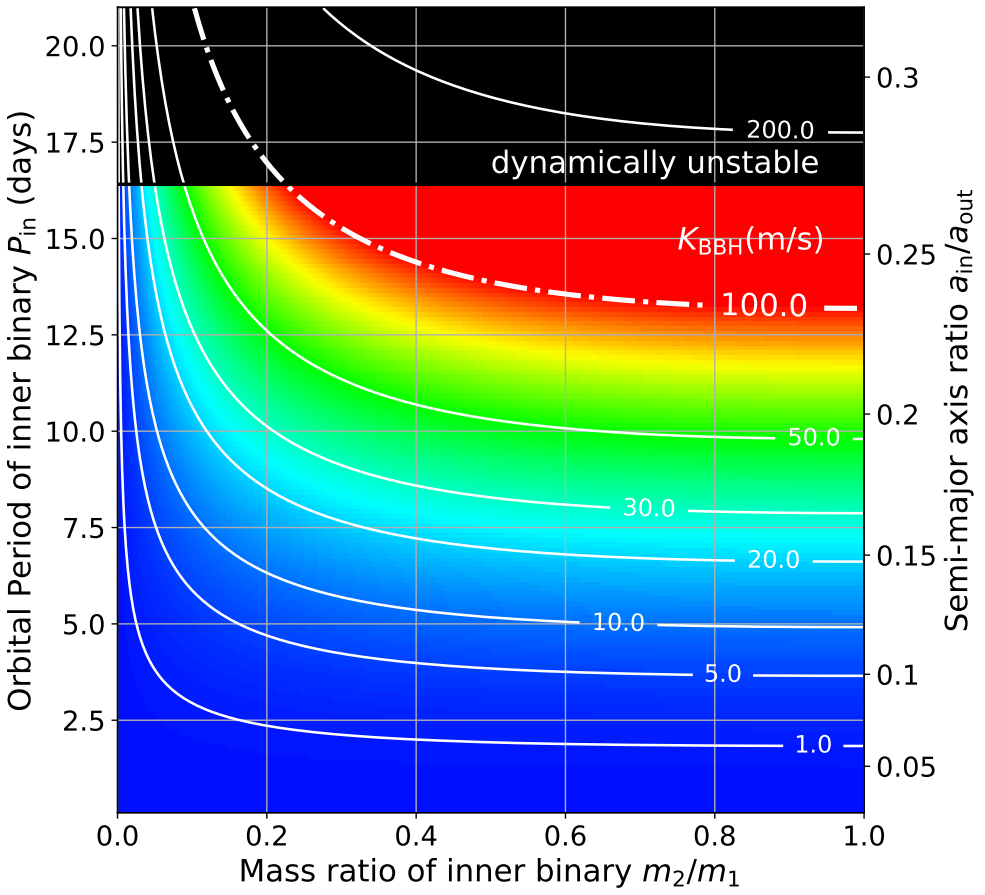

Figure A.1 Characteristic semi-amplitude of RV variations $K_{\rm BBH}$ induced by a hypothetical inner binary in 2M05215658+4359220. Each contour curve is labeled by the value of $K_{\rm BBH}$ in units of m/s. The black region specifies the dynamically unstable region calculated using Mardling & Aarseth (1999, 2001). Adapted from HWS2020.

Incidentally, the coalescence time of a circular compact binary $t_{\rm GW}$ via its GW emission is given by Peters (1964):

$$t_{\rm GW} = \frac{5}{256}\frac{c^5 a_{\rm in}^4}{G^3 m_{12}^2 \mu} \approx 1.88\times 10^{11}\left(\frac{P_{\rm in}}{\rm day}\right)^{8/3}\left(\frac{m_{12}}{M_\odot}\right)^{-5/3}\ {\rm yrs}, \tag{A.3}$$

where c is the speed of light, $m_{12} = m_1 + m_2$, $\mu \equiv m_1 m_2/m_{12}$. Equation (A.3) ensures that we can safely neglect the effect of GW emissions unless $P_{\rm in} \ll 1$ days.

Considering no detection of anomalous RV variations by TRES beyond ~ 100 m/s, Figure A.1 shows that an assumed inner coplanar circular binary is constrained to have orbital period less than a couple of weeks if the binary consists of an almost equal mass objects.

Assuming a planet orbiting around the red giant with its stellocentric semi-major

axis $a_{\rm pl}$, the orbital period of planet $P_{\rm pl}$ is obtained as

$$P_{\rm pl} \approx 11 \text{ days } \left(\frac{a_{\rm pl}}{30 \text{ R}_\odot}\right)^{3/2} \gtrsim 11 \text{ days}. \tag{A.4}$$

Thus, the period of RV variations by a planet needs to be longer than 11 days. On the other hand, the period of variations by an inner binary is constrained to be shorter than $P_{\rm in}/2 \sim 13/2$ days from Figure A.1. Since the outer orbiting star is a red giant of a radius $\sim 30\ R_\odot$ (see Table 2.1), we can basically break the degeneracy between an inner binary and an S-type circumbinary planet for this specific example even if the periodic RV variation is detected.

Appendix B

Parameter correspondence between inner-binary and S-type circumbinary-planet interpretations

In section 3.6, we find that for a coplanar circular triple the RV variations are almost degenerate with those produced by an S-type circumbinary planet. If a star is a giant, we can sometimes rule out the degeneracy using same the way as for the system 2M05215658+4359220, which is discussed in the appendix A. However, this is not always applicable. Thus, we here consider a parameter correspondence for a coplanar circular case when we cannot distinguish these two possibilities.

The RV variations are basically characterized by its semi-amplitude $K_{\rm var}$ and period $P_{\rm var}$. The latter is equal to $P_{\rm pl}$ and $P_{\rm in}/2$ in the planet-star and inner BBH interpretations, respectively.

The semi-amplitude of RV variations induced by an inner binary is estimated from equation (A.1):

$$K_{\rm BBH} = (2\pi G)^{1/3} \left(\frac{m_{123}}{m_{12}}\right)^{5/3} P_{\rm out}^{-1/3} m_{123}^{1/3} \gamma^{-2} \left(\frac{P_{\rm in}}{P_{\rm out}}\right)^{7/3}, \tag{B.1}$$

where $P_{\rm out}$ is the orbital period of the outer star, $m_{12} = m_1 + m_2$, $m_{123} = m_{12} + m_*$, and $\gamma \equiv \left(\sqrt{m_2/m_1} + \sqrt{m_1/m_2}\right)$.

On the other hand, the semi-amplitude of variations induced by a coplanar circular planet around the outer star is

$$K_{\rm pl} = (2\pi G)^{1/3} P_{\rm pl}^{-1/3} m_{\rm pl} m_*^{-2/3}, \tag{B.2}$$

where $m_{\rm pl}$ is the mass of planet, and we assume that $m_{\rm pl} \ll m_*$.

We cannot distinguish these two interpretations from observation if both of them induce the RV variations with similar amplitude and period. For this case, using equations (B.1) and (B.2), we can obtain the parameter correspondence considering

$K_{\rm var} = K_{\rm BBH} = K_{\rm pl}$, and $P_{\rm var} = P_{\rm pl} = P_{\rm in}/2$:

$$m_{\rm pl} = 2^{7/3} m_*^{2/3} \left(\frac{m_{12}}{m_{12}+m_*}\right)^{5/3} \gamma^{-2} (m_{12}+m_*)^{1/3} \left(\frac{P_{\rm var}}{P_{\rm out}}\right)^{8/3}. \tag{B.3}$$

Equation (B.3) relates the parameters in the two different interpretations.

Figures B.1 shows the parameter correspondence between $m_{\rm pl}$ in the planet-star interpretation and m_{12} in the inner BBH interpretation for $P_{\rm out} = 100$ days. We assume that $m_2/m_1 = 1$ and $m_* = 1\ M_\odot$. Given the values of the RV variation semi-amplitude and period, $K_{\rm var}$ (color-coded) and $P_{\rm var}$ (black contour), the corresponding values of $m_{\rm pl}$ and m_{12} can be read off from the figures.

The dotted area above the blue curve is excluded in the inner BBH picture from the instability of the triple. We use the dynamical stability criterion (Mardling & Aarseth 1999, 2001) (see equation (A.2)) to compute the region. The tiny black region is excluded by the instability of the planet orbiting the star. To compute the region, we adopt the following Hill instability criterion (e.g. Barnes & O'Brien 2002; Holman & Wiegert 1999):

$$a_{\rm pl} > f \left(\frac{m_*}{3m_{12}}\right)^{1/3} a_{\rm out} \qquad \left(\mu \equiv \frac{m_{12}}{m_{12}+m_*} \gtrsim 0.8\right), \tag{B.4}$$

where $f = 0.36$ is derived from numerical simulations, and $a_{\rm pl}$ is the stellocentric semi-major axis of planet. Note that m_{12} is interpreted as the mass of a single BH in a planet-star picture. Figure B.1 shows that most of regions accept both interpretations, indicating that a Hot Jupiter around a star in a star-BH binary system may mimic the RV variation induced by an inner binary in the system. Therefore, we conclude that it is necessary to analyze the signals carefully to distinguish two interpretations for such a case.

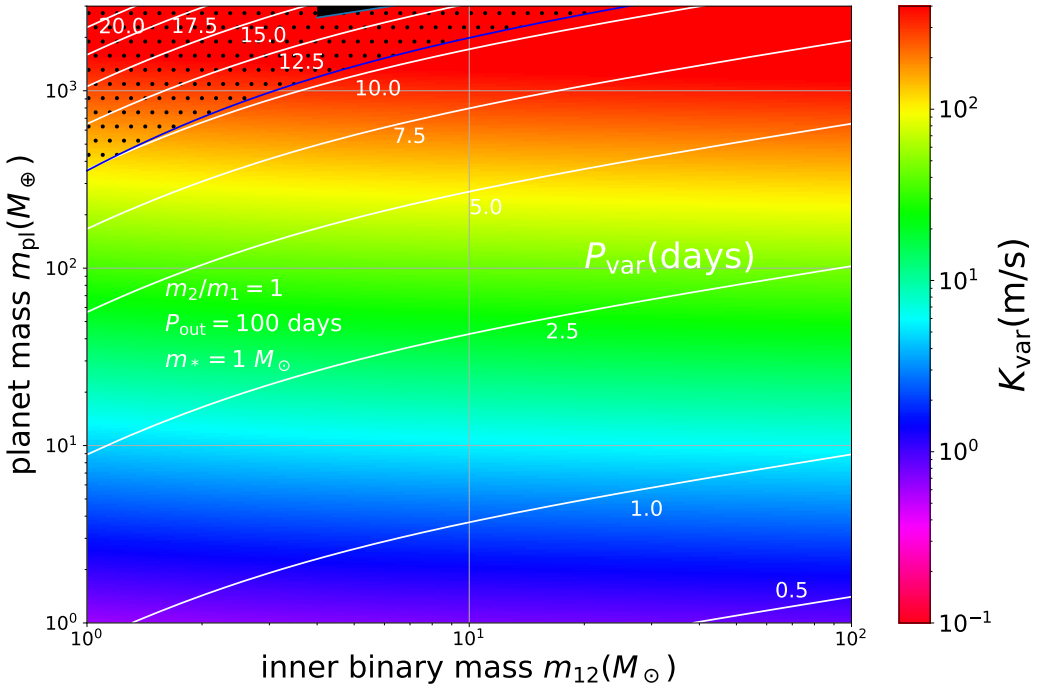

Figure B.1 An example of the parameter degeneracy between the inner binary mass m_{12} and the planet mass $m_{\rm pl}$ that produce almost the same RV variation of a period $P_{\rm var}$ and a semi-amplitude $K_{\rm var}$. We assume that a tertiary star of $1M_\odot$ orbits around an equal-mass BBH with an orbital period of $P_{\rm out} = 100$ days. The dotted region excludes the inner BBH picture from the dynamical instability condition for the triple system according to Mardling & Aarseth (1999, 2001). The tiny black region excludes the planet picture from inequality (B.4). Adapted from HWS2020.

Appendix C

Analytic discussion on the orbital period of a modulated Keplerian motion

In order to clearly detect the Rømer delay induced by the inner-binary perturbation, it is important to precisely determine the Keplerian motion and properly subtract it from the timing data. In chapter 3, we confirmed that this is indeed achieved by fittings. In the present appendix, we briefly discuss how the Keplerian motion is modulated and the best-fit parameters of the Keplerian orbit can be interpreted under the presence of the inner-binary perturbation. For simplicity, we only consider a coplanar near-circular triple.

Following Morais & Correia (2008) (see also chapter 2), the radial Keplerian motion under the inner-binary perturbation is written by the unperturbed Keplerian term $z_{\rm Kep}^{(0)}(t)$ and the tiny correction $\delta z_{\rm Kep}(t)$ as

$$\begin{aligned} z_{\rm Kep}(t) &= z_{\rm Kep}^{(0)}(t) + \delta z_{\rm Kep}(t) \\ &= \frac{m_{12}}{m_{123}} a_{\rm out} \left[1 + \frac{3}{4} \frac{m_1 m_2}{m_{12}^2} \left(\frac{a_{\rm in}}{a_{\rm out}} \right)^2 \right] \sin I_{\rm out} \\ &\quad \times \sin(\nu_{\rm out} t + f_{\rm out,0} + \omega_{\rm out}), \end{aligned} \tag{C.1}$$

where $\nu_{\rm out}$ and $\omega_{\rm out}$ denote the mean motion and argument of pericenter of the tertiary, and $f_{\rm out,0}$ is the initial true anomaly at $t = 0$. We note that since the outer orbit in a triple system should have a non-vanishing eccentricity due to the inner-binary perturbation, although it is very tiny in general, $\omega_{\rm out}$ in the above expressions is generally well defined. The above expression shows the amplitude of the radial Keplerian motion is modulated by the inner-binary perturbation with the order of $(a_{\rm in}/a_{\rm out})^2$.

The averaged orbital period $P_{\rm out}^{\rm (ave)}$ over an orbital motion is modulated due to the long-term effects of the inner-binary perturbation. Since $\omega_{\rm out}$ and $f_{\rm out,0}$ are not constant with time under the perturbation, the angular frequency corresponding to

the averaged orbital period is written as

$$\nu_{\rm out}^{\rm (ave)} \equiv \frac{2\pi}{P_{\rm out}^{\rm (ave)}} \approx \nu_{\rm out} + \dot{\omega}_{\rm out} + \dot{f}_{\rm out,0}. \tag{C.2}$$

The $\dot{\omega}_{\rm out}$ and $\dot{f}_{\rm out,0}$ can be calculated by the Lagrange planetary equations using the orbit-averaged quadrupole Hamiltonian of triple system. The orbit-averaged quadrupole Hamiltonian $\bar{F}$ is given by (e.g., Morais & Correia 2012, see also chapter 2):

$$\begin{aligned}\bar{F} &= C_{\rm quad}[2 - 12e_{\rm in}^2 - 6(1-e_{\rm in}^2)(\sin I_{\rm in}\sin I_{\rm out}\cos(\Delta\Omega) + \cos I_{\rm in}\cos I_{\rm out})^2 + 30e_{\rm in}^2 \\ &\quad \times(-\sin I_{\rm out}\cos I_{\rm in}\sin\omega_{\rm in}\cos(\Delta\Omega) - \sin I_{\rm out}\cos\omega_{\rm in}\sin(\Delta\Omega) \\ &\quad + \sin I_{\rm in}\sin\omega_{\rm in}\cos I_{\rm out})^2],\end{aligned} \tag{C.3}$$

where

$$C_{\rm quad} \equiv \frac{\mathcal{G}}{16}\frac{m_1m_2}{m_{12}}\frac{m_3}{(1-e_{\rm out}^2)^{3/2}}\left(\frac{a_{\rm in}^2}{a_{\rm out}^3}\right) \quad \text{and} \quad \Delta\Omega \equiv \Omega_{\rm in} - \Omega_{\rm out}. \tag{C.4}$$

The Lagrange planetary equations of $\omega_{\rm out}$ and $f_{\rm out,0}$ are (see e.g. Danby 1988)

$$\dot{\omega}_{\rm out} = -\frac{\sqrt{1-e_{\rm out}^2}}{\mu_{\rm out}\nu_{\rm out}a_{\rm out}^2e_{\rm out}}\frac{\partial\bar{F}}{\partial e_{\rm out}} + \frac{\cos I_{\rm out}}{\mu_{\rm out}\nu_{\rm out}a_{\rm out}^2\sqrt{1-e_{\rm out}^2}\sin I_{\rm out}}\frac{\partial\bar{F}}{\partial I_{\rm out}} \tag{C.5}$$

and

$$\dot{f}_{\rm out,0} \approx \dot{\bar{M}}_{\rm out,0} = \frac{1-e_{\rm out}^2}{\mu_{\rm out}\nu_{\rm out}a_{\rm out}^2e_{\rm out}}\frac{\partial\bar{F}}{\partial e_{\rm out}} + \frac{2}{\mu_{\rm out}\nu_{\rm out}a_{\rm out}}\frac{\partial\bar{F}}{\partial a_{\rm out}}, \tag{C.6}$$

where $\mu_{\rm out} \equiv m_3m_{12}/m_{123}$. The $\bar{M}_{\rm out,0}$ is defined by the mean anomaly $M_{\rm out}$ to avoid the secular term in the equation as

$$M_{\rm out} \equiv \nu_{\rm out}(t-t_0) + M_{\rm out,0} \equiv \int_{t_0}^{t}\nu_{\rm out}dt + \bar{M}_{\rm out,0}, \tag{C.7}$$

where t_0 is the initial time. Note that we use the fact that the initial true anomaly is well approximated by the initial mean anomaly for a near-circular case. Substituting the equation (C.3) into the Lagrange planetary equations, and neglect the outer eccentricity $e_{\rm out}$, we obtain

$$\dot{\omega}_{\rm out} \approx \frac{12C_{\rm quad}}{\mu_{\rm out}\nu_{\rm out}a_{\rm out}^2} \quad \text{and} \quad \dot{f}_{\rm out,0} \approx \frac{12C_{\rm quad}}{\mu_{\rm out}\nu_{\rm out}a_{\rm out}^2}. \tag{C.8}$$

Therefore, the averaged orbital period $P_{\rm out}^{\rm (ave)}$ over a orbital motion is approximated as

$$\frac{P_{\rm out}^{\rm (ave)}}{P_{\rm out}} \approx \frac{2\pi}{\nu_{\rm out} + \dot{\omega}_{\rm out} + \dot{f}_{\rm out,0}} \approx 1 - \frac{2\dot{\omega}_{\rm out}P_{\rm out}}{2\pi}. \tag{C.9}$$

Incidentally, the averaged behaviors of Figure 3.3 in chapter 3 is well reproduced from the above equation.

Appendix D

Dependence of disruption time on initial phases, $P_{\rm in}$ scale, and mass scale

D.1 Initial phase dependence

Here, we briefly discuss a possible effect of initial phases on the disruption times $T_{\rm d}$. For simplicity, we here vary the outer mean anomaly $M_{\rm out}$ and outer argument of pericenter $\omega_{\rm out}$, and fixed other phases at the values for our fiducial triple. Unlike chapter 6, we consider to vary initial phases using the sets of initial phase values $(\omega_{\rm out}, M_{\rm out}) = (18+72m, 18+72n)$ deg, where m and n runs from 0 to 4. We perform the disruption time simulations with all these $(\omega_{\rm out}, M_{\rm out})$ at each $(e_{\rm out}, \alpha)$. Thus, in total, 5×5 simulations with different initial phases are realized for each $(e_{\rm out}, \alpha)$.

Figure D.1 shows examples of the cumulative distribution of $\log_{10}(T_{\rm d}/P_{\rm in})$ at $(e_{\rm out}, \alpha)$ $= (0.50, 0.17)$ for $(q_{21}, i_{\rm mut}) = (1, 0°)$ (red) and $(1/9, 90°)$ (blue). In what follows, we fix the tertiary mass m_3 as 3 $M_\odot$ unless otherwise specified. We clearly see that the disruption times $T_{\rm d}$ are distributed around the peaks $\sim$ 3.5 (red) and $\sim$ 4 (blue) within $\sim \pm 1$ differences. The distributions are basically similar for different values of $(e_{\rm out}, \alpha)$, q_{21}, and $i_{\rm mut}$.

Figure D.2 shows dependence of $\log_{10}(T_{\rm d}/P_{\rm in})$ on the $(e_{\rm out}, \alpha)$ plot for $(q_{21}, i_{\rm mut}) =$ $(1, 0°)$ (Left) and $(1/9, 90°)$ (Right). In the plots, the mean value of $T_{\rm d}$ at each $(e_{\rm out}, \alpha)$ is color-coded, and the upper and lower 34 % range is denoted by the error bars. The figure shows that the initial phase dependence is within $\sim \pm 1$ order of $T_{\rm d}/P_{\rm in}$, and has no clear systematic tendency. The figure also confirm that the stable region ($T_{\rm d} > t_{\rm int}$) is preserved even after changing the initial phases. Therefore, we conclude that the initial phase dependence can be treated as ± 1 order statistical uncertainty of disruption time except for very specific cases such like resonances.

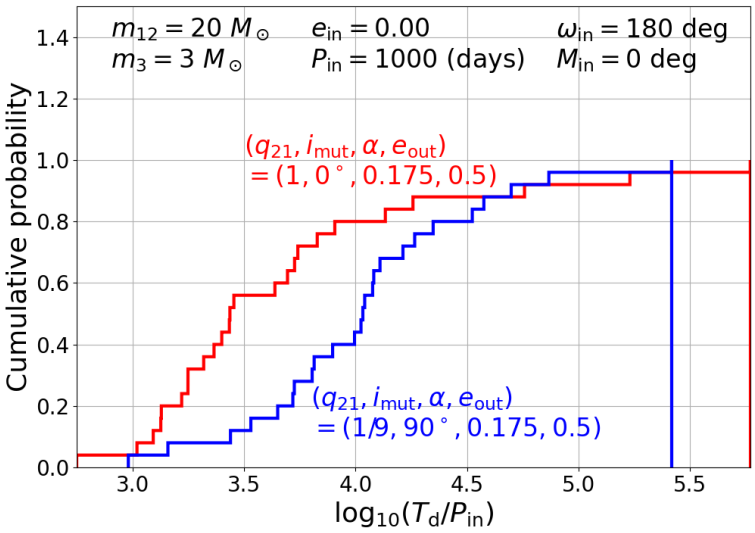

Figure D.1 The cumulative distribution of the disruption times for various initial phases $(M_{\rm out}, \omega_{\rm out})$.We pick up the result at $(e_{\rm out}, \alpha) = (0.17, 0.50)$ for $(q_{21}, i\text{mut}) = (1, 0^\circ)$ (red) and $(1/9, 90^\circ)$ (blue).

D.2 The scalability of the disruption time $T_{\rm d}$ on $P_{\rm in}$ and masses

In chapter 6, we rely on the scalability of disruption time $T_{\rm d}$ with respect to $P_{\rm in}$ and mass scale. Here, we briefly show how this assumption is justified using numerical simulations.

Top-left panel of Figure D.3 shows the same plot as Figures 6.4, respectively but for $P_{\rm in} = 10000$ days, which is 10 times larger value than the value we considered earlier. The top-right panel shows the same plot as the top-left panel, but for $i_{\rm mut} = 90^\circ$ and $q_{21} = 0.1$. The plots show that the overall distribution does not change significantly for different $P_{\rm in}$ values. The bottom two panels show the corresponding cumulative distributions of $T_{\rm d}$ ratio to the top panels. Here, we evaluate the disruption time $T_{\rm d}$ ratio between $P_{\rm in} = 1000, 10000$ days at each $(e_{\rm out}, \alpha)$. Note that we only include the systems with $P_{\rm in} < T_{\rm d} < t_{\rm int}$ for the cumulative distributions. These plots show the $T_{\rm d}$ ratio is sharply peaked at ~ 10 in the linear scale, and the uncertainty is within $\sim \pm 1$ order. The fact implies that the $P_{\rm in}$ scalability is guaranteed in the statistical sense. Note that $P_{\rm out}$ scalability is simultaneously satisfied at fixed α statistically. Although we do not show the results here, the simulations with $P_{\rm in} = 100$ days further confirm this result. We also check the invariance of $T_{\rm d}$ with respect to the mass scale by performing the simulations for 10 times larger and smaller masses: $(m_{12}, m_3) = (200, 30)\ M_\odot$ and $(2, 0.3)\ M_\odot$. Although we do not show the plots here, the result follows the similar tendency of Figure D.3. Thus, it is confirmed that the mass scalability is also guaranteed statistically.

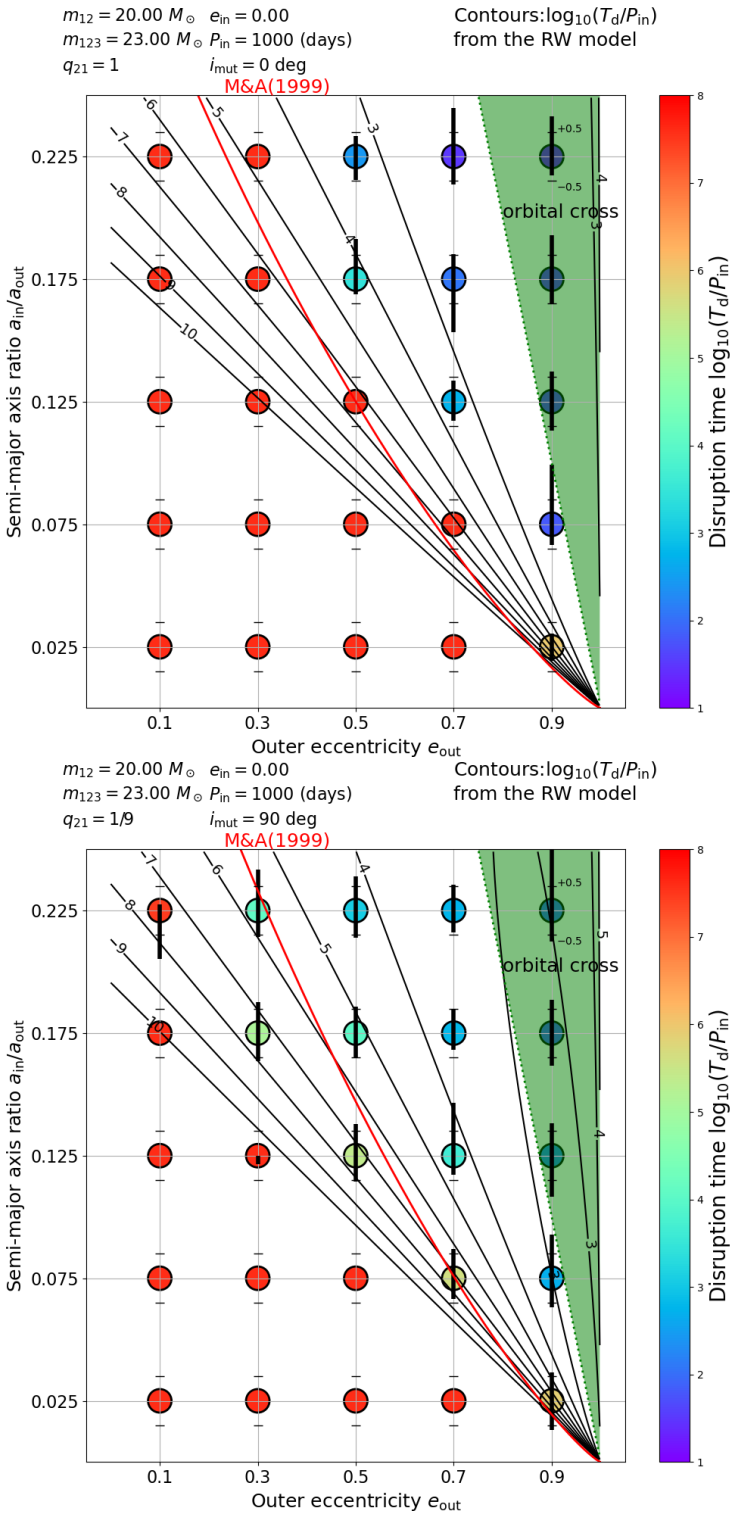

Figure D.2 The disruption time distributions on $(e_{\rm out}, \alpha)$. The mean values are color-coded, and the 34% levels are denoted as the error bars. Left:$(i_{\rm mut}, q_{21}) = (0\ {\rm deg}, 1)$, Right:$(i_{\rm mut}, q_{21}) = (90\ {\rm deg}, 1/9)$.

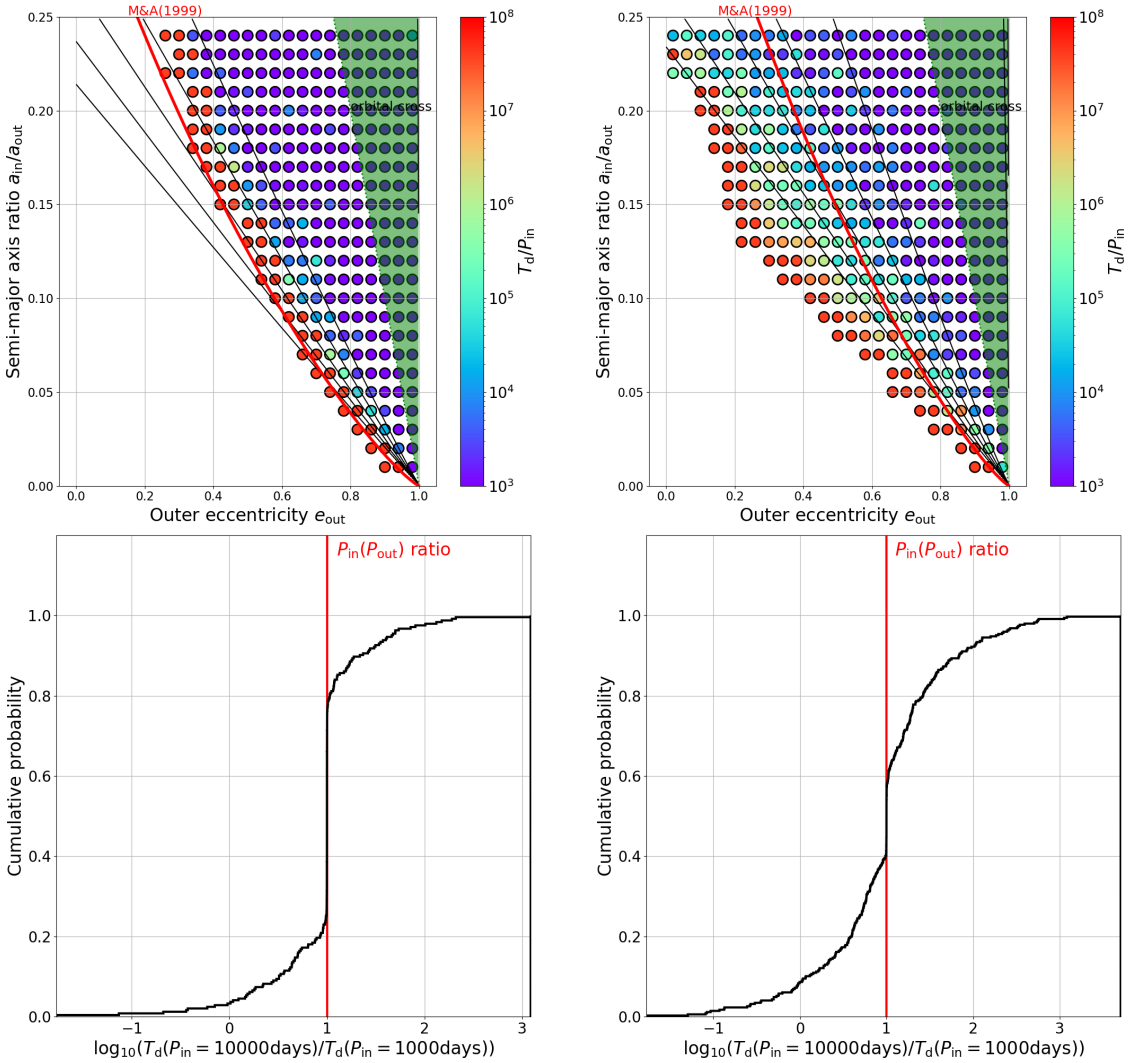

Figure D.3 The $P_{\rm in}(P_{\rm out})$ scalability of the disruption time. The top figures show the distribution on $(e_{\rm out}, \alpha)$ for $P_{\rm in} = 10000$ days. The bottom figures show the cumulative distributions of the ratio of disruption times with $P_{\rm in} = 1000, 10000$ days. Left: $(i_{\rm mut}, q_{21}) = (0\ {\rm deg}, 1)$, Right:$(i_{\rm mut}, q_{21}) = (90\ {\rm deg}, 1/9)$.

Appendix E

Comparison of the orbital evolution simulated with REBOUND and TSUNAMI

In chapter 6, we used a N-body simulation package TSUNAMI rather than REBOUND to achieve fast and accurate simulations. Here, we present the comparison of the orbital evolution simulated with REBOUND and TSUNAMI, and confirm that TSUNAMI can accurately calculate orbital evolution. For simplicity, we performed the simulations with TSUNAMI for I1010 ($i_{\rm mut} = 45°$, $m_1 = m_2$), O1010 ($i_{\rm mut} = 90°$, $m_1 = m_2$), I0218 ($i_{\rm mut} = 45°$, $m_1 = 9m_2$), and O0218 ($i_{\rm mut} = 90°$, $m_1 = 9m_2$) in chapter 4. The input values of orbital parameters are summarized in Tables 3.2 and 4.1 in chapters 3 and 4.

Figure E.1 shows the orbital evolution for I1010 and O1010 performed with REBOUND and TSUNAMI. Each panel contains the evolution of mutual inclination $i_{\rm mut}$, inner inclination $I_{\rm in}$, outer inclination $I_{\rm out}$, and the longitudes of ascending nodes $\Omega_{\rm in}$ and $\Omega_{\rm out}$. Top and bottom panels show the results for I1010 and O1010, respectively. Left panels show the results with REBOUND, which are same as Figures 4.3 and 4.4 in chapter 4. On the other hand, right panels show the results for the same systems performed with TSUNAMI. In order to see the detail of $i_{\rm mut}$ evolution for I1010, we also include the enlarged figures in top panels. The result indicates that the whole evolution is not sensitive to the specific choice of two N-body packages REBOUND and TSUNAMI. Figure E.2 shows the same figure as Figure E.1 but for I0218 and O0218. The result again confirms that the whole evolution is accurately reproduced with TSUNAMI.

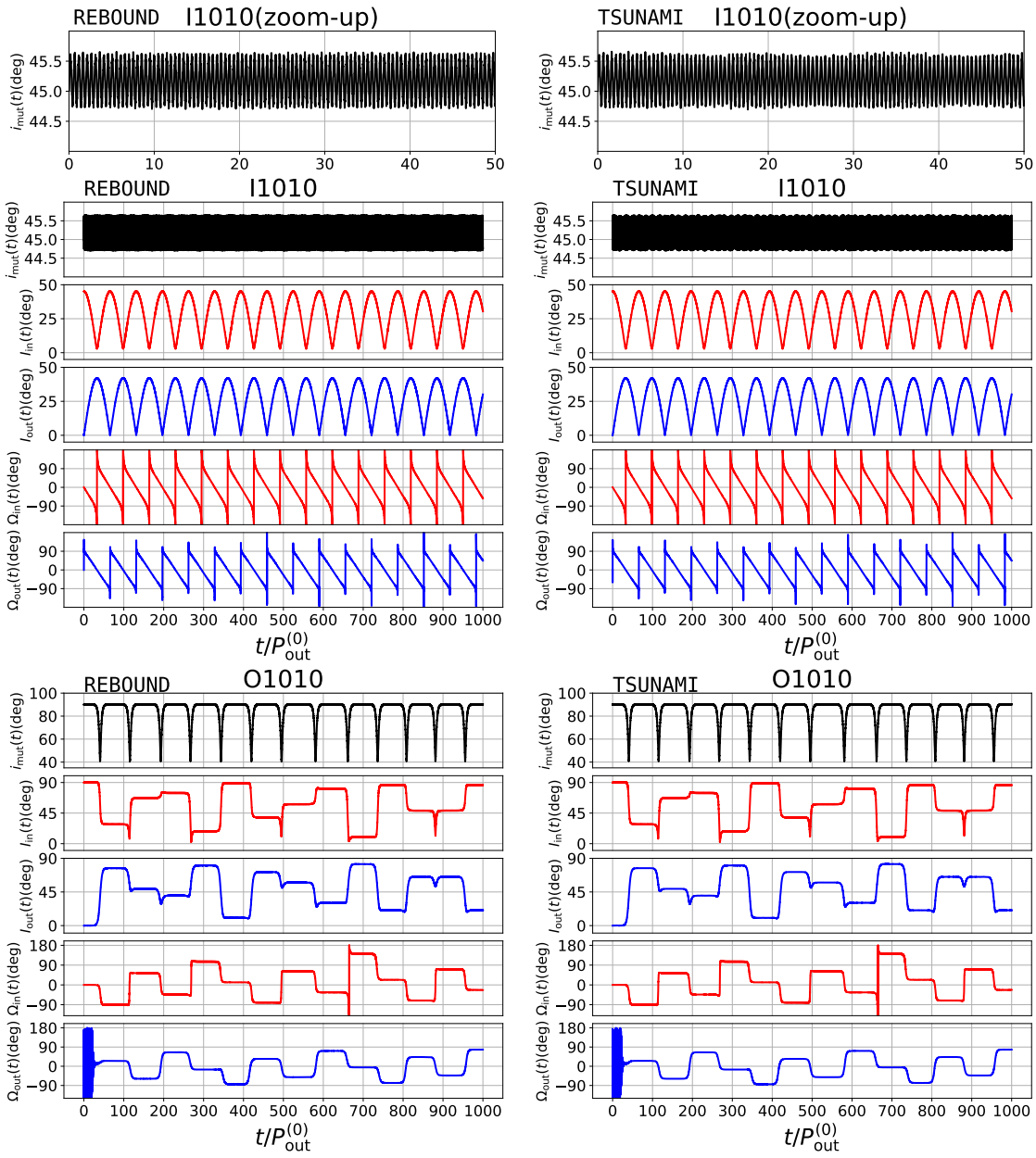

Figure E.1 Orbital evolution for I1010 and O1010 performed with REBOUND (left) and TSUNAMI (right). Top and bottom panels show the results for I1010 and O1010, respectively. The enlarged figures of $i_{\rm mut}$ evolution for I1010 are included in top panels.

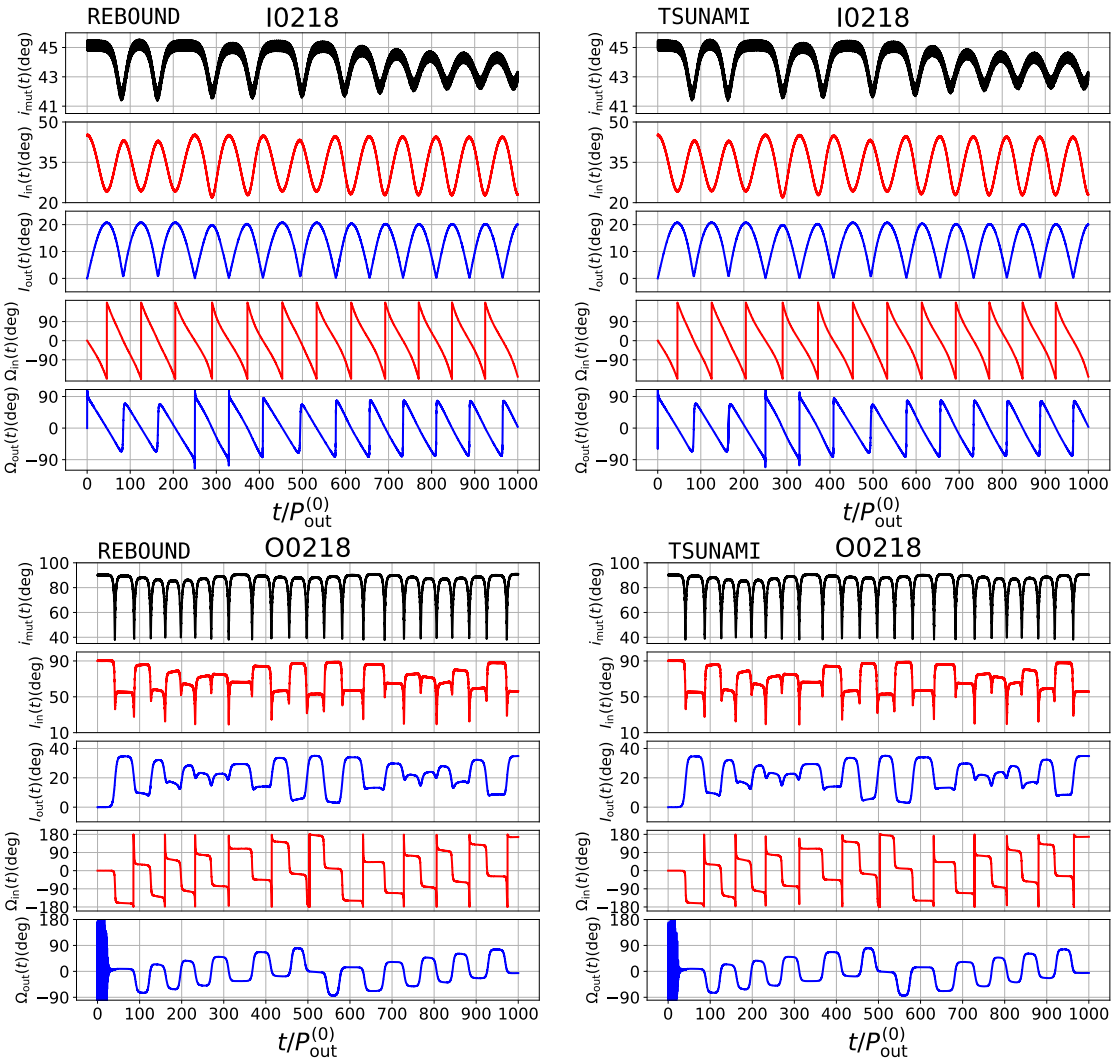

Figure E.2 Same as Figure E.1 but for I0218 and O0218.

Bibliography

Aarseth, S. J., & Mardling, R. A. 2001, Astronomical Society of the Pacific Conference Series, Vol. 229, The Formation and Evolution of Multiple Star Systems, ed. P. Podsiadlowski, S. Rappaport, A. R. King, F. D'Antona, & L. Burderi, 77

Adams, J. C. 1846, MNRAS, 7, 149

Akutsu, T., Ando, M., Arai, K., et al. 2021, Progress of Theoretical and Experimental Physics, 2021, 05A101

Amaro-Seoane, P., Audley, H., Babak, S., et al. 2017, arXiv e-prints, arXiv:1702.00786. https://arxiv.org/abs/1702.00786

Antognini, J. M. O. 2015, MNRAS, 452, 3610

Antognini, J. M. O., & Thompson, T. A. 2016, MNRAS, 456, 4219

Astropy Collaboration, Robitaille, T. P., Tollerud, E. J., et al. 2013, A&A, 558, A33

Astropy Collaboration, Price-Whelan, A. M., Sipőcz, B. M., et al. 2018, AJ, 156, 123

Backer, D. C., & Hellings, R. W. 1986, ARA&A, 24, 537

Barnes, J. W., & O'Brien, D. P. 2002, ApJ, 575, 1087

Barsotti, L., Gras, S., Evans, M., & Fritschel, P. 2018, The updated Advanced LIGO design curve, Tech. Rep. LIGO-T1800044-v5, LIGO

Belczyński, K., & Bulik, T. 1999, A&A, 346, 91. https://arxiv.org/abs/astro-ph/9901193

Belczynski, K., Dominik, M., Repetto, S., Holz, D. E., & Fryer, C. L. 2012, ArXiv e-prints. https://arxiv.org/abs/1208.0358

Belczynski, K., Holz, D. E., Bulik, T., & O'Shaughnessy, R. 2016, Nature, 534, 512

Belczynski, K., Kalogera, V., & Bulik, T. 2002, ApJ, 572, 407

Belczynski, K., Taam, R. E., Kalogera, V., Rasio, F. A., & Bulik, T. 2007, ApJ, 662, 504

Bird, S., Cholis, I., Muñoz, J. B., et al. 2016, Physical Review Letters, 116, 201301

Bodensteiner, J., Shenar, T., Mahy, L., et al. 2020, A&A, 641, A43

Breivik, K., Chatterjee, S., & Larson, S. L. 2017, ApJ, 850, L13

Brown, E. W. 1899, MmRAS, 53, 39

Cameron, A. D., Champion, D. J., Kramer, M., et al. 2018, Monthly Notices of the Royal Astronomical Society: Letters, 475, L57

Corongiu, A., Kramer, M., Stappers, B. W., et al. 2007, A&A, 462, 703

Cunha, J. V., Silva, F. E., & Lima, J. A. S. 2018, MNRAS, 480, L28

Danby, J. M. A. 1988, Fundamentals of celestial mechanics (Willmann-Bell, Inc.)

de Elía, G. C., Zanardi, M., Dugaro, A., & Naoz, S. 2019, A&A, 627, A17

Demorest, P. B., Pennucci, T., Ransom, S. M., Roberts, M. S. E., & Hessels, J. W. T. 2010, Nature, 467, 1081

Dominik, M., Belczynski, K., Fryer, C., et al. 2012, ApJ, 759, 52

—. 2013, ApJ, 779, 72

Dosopoulou, F., & Kalogera, V. 2016, ApJ, 825, 71

Edwards, R. T., Hobbs, G. B., & Manchester, R. N. 2006, MNRAS, 372, 1549

Einstein, A. 1915, Sitzungsberichte der Königlich Preußischen Akademie der Wissenschaften (Berlin), 831

Ferdman, R. D., Stairs, I. H., Kramer, M., et al. 2014, Monthly Notices of the Royal Astronomical Society, 443, 2183

Ferdman, R. D., Freire, P. C. C., Perera, B. B. P., et al. 2020, Nature, 583, 211

Fonseca, E., Stairs, I. H., & Thorsett, S. E. 2014, The Astrophysical Journal, 787, 82

Fragione, G., Martinez, M. A. S., Kremer, K., et al. 2020, arXiv e-prints, arXiv:2007.11605. https://arxiv.org/abs/2007.11605

Fulton, B. J., Petigura, E. A., Blunt, S., & Sinukoff, E. 2018, PASP, 130, 044504

Gaia Collaboration, Prusti, T., de Bruijne, J. H. J., et al. 2016, A&A, 595, A1

Galle, J. G. 1846, MNRAS, 7, 153

Gomez, S., & Grindlay, J. E. 2021, ApJ, 913, 48

Gupta, P., Suzuki, H., Okawa, H., & Maeda, K.-i. 2020, Phys. Rev. D, 101, 104053

Hajdu, T., Borkovits, T., Forgács-Dajka, E., Sztakovics, J., & Bódi, A. 2021, MNRAS

Haniewicz, H. T., Ferdman, R. D., Freire, P. C. C., et al. 2020, arXiv e-prints, arXiv:2007.07565. https://arxiv.org/abs/2007.07565

Harrington, R. S. 1972, Celestial Mechanics, 6, 322

Harry, G. M., Fritschel, P., Shaddock, D. A., Folkner, W., & Phinney, E. S. 2006, Classical and Quantum Gravity, 23, 4887

Hartle, J. B. 2003, Gravity : an introduction to Einstein's general relativity (Pearson)

Hayashi, T., & Suto, Y. 2020, ApJ, 897, 29

—. 2021, ApJ, 907, 48

Hayashi, T., Wang, S., & Suto, Y. 2019, A strategy to search for an inner binary black hole from the motion of the tertiary star I: a perturbative analytic approach to a coplanar and near-circular three-body system and its application to 2M05215658+4359220. https://arxiv.org/abs/1905.07100v1

—. 2020, The Astrophysical Journal, 890, 112

Hill, G. W. 1877, On the part of the motion of the lunar perigee which is a function of the mean motions of the sun and moon.

Holman, M. J., & Wiegert, P. A. 1999, AJ, 117, 621

Hut, P., & Bahcall, J. N. 1983, ApJ, 268, 319

Ivezić, Ž., Kahn, S. M., Tyson, J. A., et al. 2019, ApJ, 873, 111

Janssen, G. H., Stappers, B. W., Kramer, M., et al. 2008, A&A, 490, 753

Jha, S., Torres, G., Stefanik, R. P., Latham, D. W., & Mazeh, T. 2000, MNRAS, 317, 375

Kawanaka, N., Yamaguchi, M., Piran, T., & Bulik, T. 2017, in IAU Symposium, Vol. 324, New Frontiers in Black Hole Astrophysics, ed. A. Gomboc (Cambridge University Press), 41–42

Keith, M. J., Kramer, M., Lyne, A. G., et al. 2009, Monthly Notices of the Royal Astronomical Society, 393, 623

Kinoshita, H., & Nakai, H. 1999, Celestial Mechanics and Dynamical Astronomy, 75, 125

Kinugawa, T., Inayoshi, K., Hotokezaka, K., Nakauchi, D., & Nakamura, T. 2014, MNRAS, 442, 2963

Kinugawa, T., Miyamoto, A., Kanda, N., & Nakamura, T. 2016, MNRAS, 456, 1093

Kozai, Y. 1962, AJ, 67, 591

Kramer, M., Stairs, I. H., Manchester, R. N., et al. 2006, Science, 314, 97

Kremer, K., Ye, C. S., Rui, N. Z., et al. 2020, ApJS, 247, 48

Kumamoto, J., Fujii, M. S., & Tanikawa, A. 2020, MNRAS, 495, 4268

Laplace, P. S. 1798, Traité De Mécanique Céleste (Paris, Chez J.B.M. Duprat, an VII)

Le Verrier, U. J. 1846, Astronomische Nachrichten, 25, 65

Le Verrier, U.-J. 1859, Comptes rendus hebdomadaires des séances de l'Académie des sciences, 49, 379

Lennon, D. J., Dufton, P. L., Villaseñor, J. I., et al. 2021a, arXiv e-prints, arXiv:2111.12173. https://arxiv.org/abs/2111.12173

Lennon, D. J., Maíz Apellániz, J., Irrgang, A., et al. 2021b, A&A, 649, A167

Lewis, K. M., Ochiai, H., Nagasawa, M., & Ida, S. 2015, ApJ, 805, 27

Lidov, M. L. 1962, Planet. Space Sci., 9, 719

Liu, B., & Lai, D. 2017, ApJ, 846, L11

—. 2018, ApJ, 863, 68

Liu, B., Muñoz, D. J., & Lai, D. 2015, MNRAS, 447, 747

Liu, J., Zhang, H., Howard, A. W., et al. 2019, Nature, 575, 618

Lu, C. X., & Naoz, S. 2019, MNRAS, 484, 1506

Lynch, R. S., Swiggum, J. K., Kondratiev, V. I., et al. 2018, The Astrophysical Journal, 859, 93

Manwadkar, V., Kol, B., Trani, A. A., & Leigh, N. W. C. 2021, MNRAS, 506, 692

Manwadkar, V., Trani, A. A., & Leigh, N. W. C. 2020, MNRAS, 497, 3694

Mardling, R., & Aarseth, S. 1999, in NATO Advanced Science Institutes (ASI) Series C, Vol. 522, NATO Advanced Science Institutes (ASI) Series C, ed. B. A. Steves & A. E. Roy (Springer), 385

Mardling, R. A. 1995a, ApJ, 450, 722

—. 1995b, ApJ, 450, 732

—. 2013, MNRAS, 435, 2187

Mardling, R. A., & Aarseth, S. J. 2001, MNRAS, 321, 398

Marks, M., & Kroupa, P. 2012, A&A, 543, A8

Martinez, J. G., Stovall, K., Freire, P. C. C., et al. 2015, The Astrophysical Journal, 812, 143

—. 2017, The Astrophysical Journal, 851, L29

Mashian, N., & Loeb, A. 2017, MNRAS, 470, 2611

Masuda, K., & Hotokezaka, K. 2019, ApJ, 883, 169

Merritt, D. 2013, Dynamics and Evolution of Galactic Nuclei (Princeton University Press)

Michaely, E., & Perets, H. B. 2014, ApJ, 794, 122

Mikkola, S., & Aarseth, S. J. 1993, Celestial Mechanics and Dynamical Astronomy, 57, 439

Mikkola, S., & Tanikawa, K. 2013a, MNRAS, 430, 2822

—. 2013b, New A, 20, 38

Moe, M., & Di Stefano, R. 2017, ApJS, 230, 15

Moore, C. J., Cole, R. H., & Berry, C. P. L. 2015, Classical and Quantum Gravity, 32, 015014

Morais, M. H. M., & Correia, A. C. M. 2008, A&A, 491, 899

—. 2011, A&A, 525, A152

—. 2012, MNRAS, 419, 3447

Murray, C. D., & Dermott, S. F. 2000, Solar System Dynamics (Cambridge University Press)

Mushkin, J., & Katz, B. 2020, MNRAS, 498, 665

Mylläri, A., Valtonen, M., Pasechnik, A., & Mikkola, S. 2018, MNRAS, 476, 830

Naoz, S., Farr, W. M., Lithwick, Y., Rasio, F. A., & Teyssandier, J. 2013, MNRAS, 431, 2155

Naoz, S., Li, G., Zanardi, M., de Elía, G. C., & Di Sisto, R. P. 2017, AJ, 154, 18

Naoz, S., Will, C. M., Ramirez-Ruiz, E., et al. 2020, ApJ, 888, L8

Nelemans, G., Yungelson, L. R., & Portegies Zwart, S. F. 2001, A&A, 375, 890

Newhall, X. X., Standish, E. M., & Williams, J. G. 1983, A&A, 125, 150

Newton, I. 1687, Philosophiae Naturalis Principia Mathematica. Auctore Js. Newton

Ochiai, H., Nagasawa, M., & Ida, S. 2014, ApJ, 790, 92

O'Leary, R. M., Kocsis, B., & Loeb, A. 2009, MNRAS, 395, 2127

O'Leary, R. M., Rasio, F. A., Fregeau, J. M., Ivanova, N., & O'Shaughnessy, R. 2006, ApJ, 637, 937

Perpinyà-Vallès, M., Rebassa-Mansergas, A., Gänsicke, B. T., et al. 2019, MNRAS, 483, 901

Perryman, M., Hartman, J., Bakos, G. Á., & Lindegren, L. 2014, ApJ, 797, 14

Peters, P. C. 1964, Physical Review, 136, 1224

Plavchan, P., Latham, D., Gaudi, S., et al. 2015, arXiv e-prints, arXiv:1503.01770. https://arxiv.org/abs/1503.01770

Poincaré, H. 1892, Les méthodes nouvelles de la mécanique céleste

Portegies Zwart, S. F., & McMillan, S. L. W. 2000, ApJ, 528, L17

Raghavan, D., McAlister, H. A., Henry, T. J., et al. 2010, ApJS, 190, 1

Ransom, S. M., Stairs, I. H., Archibald, A. M., et al. 2014, Nature, 505, 520

Rastello, S., Mapelli, M., Di Carlo, U. N., et al. 2020, MNRAS, 497, 1563

Rein, H., & Liu, S. F. 2012, A&A, 537, A128

Rein, H., & Tamayo, D. 2015, MNRAS, 452, 376

Rivinius, T., Baade, D., Hadrava, P., Heida, M., & Klement, R. 2020, A&A, 637, L3

Robson, T., Cornish, N. J., & Liu, C. 2019, Classical and Quantum Gravity, 36, 105011

Rodriguez, C. L., Haster, C.-J., Chatterjee, S., Kalogera, V., & Rasio, F. A. 2016, ApJ, 824, L8

Roy, A., & Haddow, M. 2003, Celestial Mechanics and Dynamical Astronomy, 87, 411

Sana, H., de Mink, S. E., de Koter, A., et al. 2012, Science, 337, 444

Sasaki, M., Suyama, T., Tanaka, T., & Yokoyama, S. 2016, Physical Review Letters, 117, 061101

—. 2018, Classical and Quantum Gravity, 35, 063001

Sato, S., Kawamura, S., Ando, M., et al. 2017, in Journal of Physics Conference Series, Vol. 840, Journal of Physics Conference Series, 012010

Schneider, J., & Cabrera, J. 2006, A&A, 445, 1159

Schutz, B. 2009, A First Course in General Relativity (Cambridge University Press)

Shapiro, S. L., & Teukolsky, S. A. 1983, Black holes, white dwarfs, and neutron stars : the physics of compact objects (A Wiley-Interscience Publication, New York: Wiley, 1983)

Shappee, B. J., & Thompson, T. A. 2013, ApJ, 766, 64

Shenar, T., Bodensteiner, J., Abdul-Masih, M., et al. 2020, arXiv e-prints, arXiv:2004.12882. https://arxiv.org/abs/2004.12882

Shikauchi, M., Kumamoto, J., Tanikawa, A., & Fujii, M. S. 2020, arXiv e-prints, arXiv:2001.11199. https://arxiv.org/abs/2001.11199

Stoer, J., & Bulirsch, R. 2002, Texts in applied mathematics, Vol. 12, Introduction to Numerical Analysis, 3rd edn. (New York: Springer)

Stovall, K., Freire, P. C. C., Chatterjee, S., et al. 2018, The Astrophysical Journal, 854, L22

Swiggum, J. K., Rosen, R., McLaughlin, M. A., et al. 2015, The Astrophysical Journal, 805, 156

Tagawa, H., Umemura, M., & Gouda, N. 2016, MNRAS, 462, 3812

Tamayo, D., Rein, H., Shi, P., & Hernand ez, D. M. 2020, MNRAS, 491, 2885

Tanikawa, A., Kinugawa, T., Kumamoto, J., & Fujii, M. S. 2020, PASJ

Taylor, J. H., & Weisberg, J. M. 1982, ApJ, 253, 908

The LIGO Scientific Collaboration, The Virgo Collaboration, & The KAGRA Scientific Collaboration. 2021a, arXiv e-prints, arXiv:2111.03634. https://arxiv.org/abs/2111.03634

The LIGO Scientific Collaboration, the Virgo Collaboration, the KAGRA Collaboration, et al. 2021b, arXiv e-prints, arXiv:2111.03606. https://arxiv.org/abs/2111.03606

Thompson, T. A. 2011, ApJ, 741, 82

Thompson, T. A., Kochanek, C. S., Stanek, K. Z., et al. 2019, Science, 366, 637

Tokovinin, A. 2021, AJ, 161, 144

Tokovinin, A., & Latham, D. W. 2020, AJ, 160, 251

Toonen, S., Hamers, A., & Portegies Zwart, S. 2016, Computational Astrophysics and Cosmology, 3, 6

Toonen, S., Portegies Zwart, S., Hamers, A. S., & Bandopadhyay, D. 2020, A&A, 640, A16

Trani, A. A., Fujii, M. S., & Spera, M. 2019, ApJ, 875, 42

Trani, A. A., Rastello, S., Di Carlo, U. N., et al. 2021, arXiv e-prints, arXiv:2111.06388. https://arxiv.org/abs/2111.06388

Valtonen, M., & Karttunen, H. 2006, The Three-Body Problem (Cambridge University Press)

Vinson, B. R., & Chiang, E. 2018, MNRAS, 474, 4855

Virgo Collaboration, Acernese, F., Agathos, M., et al. 2021, arXiv e-prints, arXiv:2107.03294. https://arxiv.org/abs/2107.03294

von Zeipel, H. 1910, Astronomische Nachrichten, 183, 345

Wei, L., Naoz, S., Faridani, T., & Farr, W. M. 2021, arXiv e-prints, arXiv:2106.02276. https://arxiv.org/abs/2106.02276

Weisberg, J. M., & Taylor, J. H. 2005, in Astronomical Society of the Pacific Conference Series, Vol. 328, Binary Radio Pulsars, ed. F. A. Rasio & I. H. Stairs, 25. https://arxiv.org/abs/astro-ph/0407149

Will, C. M. 2017, Phys. Rev. D, 96, 023017

Wong, K. W. K., Berti, E., Gabella, W. E., & Holley-Bockelmann, K. 2019, MNRAS, 483, L33

Yagi, K., & Seto, N. 2011, Phys. Rev. D, 83, 044011

—. 2017, Phys. Rev. D, 95, 109901

Yalinewich, A., Beniamini, P., Hotokezaka, K., & Zhu, W. 2018, MNRAS, 481, 930

Yamaguchi, M. S., Kawanaka, N., Bulik, T., & Piran, T. 2018, ApJ, 861, 21

Zorotovic, M., Schreiber, M. R., Gänsicke, B. T., & Nebot Gómez-Morán, A. 2010, A&A, 520, A86